UNIVERSIDAD MICHOACANA DE SAN NICOLÁS DE HIDALGO

INSTITUTO DE FÍSICA Y MATEMÁTICAS

AN IMPLEMENTATION OF THE LATTICE BOLTZMANN METHOD FOR THE ANALYSIS OF CAPILLARY WAVES IN CONFINED GEOMETRIES

T H E S I S

TO OBTAIN THE TITLE OF:

MASTER OF SCIENCE IN THE AREA OF PHYSICS

PRESENTED BY:

VENECIA CHÁVEZ MEDINA

ADVISOR:

DR. FRANCISCO S. GUZMÁN MURILLO

Universidad Michoacana De San Nicolás De Hidalgo

COADVISOR:

DR. TIMM KRÜGER

University of Edinburgh

MORELIA MICH. APRIL, 2019

Con todo mi amor, agradecimiento y admiración, a mis papás, Fina y Luis y a mi hermana Grecia. Cada logro en mi vida es gracias a ustedes.

ACKNOWLEDGEMENTS

El resultado de mi investigación fue posible gracias a instituciones y personas que a lo largo de estos dos años me apoyaron e impulsaron a cumplir mis metas.

En primer lugar agradezco al Consejo Nacional de Ciencia y Tecnología (CONACyT) que sostuvo mis estudios de maestría.

Al Instituto de Física y Matemáticas de la Universidad Michoacana de San Nicolás de Hidalgo por haberme abierto un espacio con un ambiente lleno de oportunidades para mi investigación. También expreso mi gratitud al Institute for Multiscale Thermofluids en la Universidad de Edimburgo que me acogió y brindó un espacio propicio para la investigación.

Mi total gratitud a mis profesores durante la maestría, Dr. Ulises Nucamendi Gómez, Dr. Thomas Zannias, Dr. Axel Weber y Dr. Ricardo Becerril, de quienes aprendí académica y profesionalmente además de trasmitirme su amor por la Física. Al Doctor Olivier Sarbach por sus enseñanzas, por su apoyo y por sus consejos. Al personal administrativo, en especial a Alejandra y a Don Manuel, por siempre contribuir en brindarnos un excelente ambiente de trabajo.

Gracias al doctor José Antonio González Cervera por los valiosos comentarios a mi investigación y por todo su apoyo durante mi formación académica; de igual manera agradezco al doctor Umberto Cotti por sus valiosos comentarios y su disposición para leer mi trabajo. A ambos gracias por aceptar ser parte de mi mesa sinodal.

Agradezco de manera muy especial a mis directores de tesis Dr. Francisco S. Guzmán y Dr. Timm Krüger por aventurarse conmigo en este proyecto brindándome siempre palabras de aliento y las mejores enseñanzas que una estudiante pueda recibir.

Reitero mi gratitud y admiración al Dr. Timm Krüger por la disposición que siempre ha mostrado, por sus asesorías, revisiones y comentarios tan atinados que sin duda solidificaron mi trabajo. A lo largo de este trabajo su guía fue fundamental. Agradezco también a su grupo de trabajo, especialmente a Rohan, Charles, Greg y Arunn quienes me brindaron siempre un ambiente amigable y lleno de apoyo.

Expreso mi gratitud y profunda admiración a mi asesor, el doctor Francisco. No hubiera sido posible cumplir esta meta sin las enseñanzas que como profesor y asesor me ha brindado; además que sus palabras de aliento y su apoyo me ayudaron a avanzar en momentos de desánimo. Siempre estaré sinceramente agradecida con usted, profe.

A mi compañera y compañeros de generación, Iza, Ruben, Cesar y Juan, con y de ustedes aprendí siempre. Gracias por estos magníficos dos años que convirtieron un bonito compañerismo es una gran amistad. A mis amigos Gonny, Jorch, Memo, Santi y Gabo; al magnífico grupo de trabajo del Dr. Francisco. Mi cariño y gratitud a Cesar, Thelma y Mati por siempre apoyarme, por sus buenos consejos y por todos los momentos que hemos compartido. De manera especial agradezco a Sofi, por la complicidad de nuestra amistad y a Anayeli por su presencia, cariño.

Siempre mi gratitud hacia Cindy por sus siempre presentes palabras de aliento y su apoyo incondicional, por su amistad irremplazable.

Por último pero por sobre todo, a mi familia. A mis abuelitas, Marie y Lola y a mis abuelitos, Miguel y Chelis por todo su cariño y cuidados. A mi hermana Grecia a quien siempre he admirado, por todos sus consejos, por todo sus regaños, por siempre creer en mí y por enseñarme a crecer. Agradezco especialmente a mis padres, Fina y Luis por todo su amor, toda su confianza, todo su tiempo, por ser siempre mi mayor sostén, por todo, por siempre, gracias.

Morelia MEX., April 9, 2019

ABSTRACT

'An Implementation of the Lattice Boltzmann Method for the Analysis of Capillary Waves in Confined Geometries' presents a code capable of simulating in 3 dimensions a two phase fluid using the Shan-Chen approach in addition to the lattice Boltzmann model. The work presents the pertinent mathematical analysis that enables a fair understanding of the method and its validity as well as the mathematical derivation and physical concepts of the hydrodynamic equations. By focusing on the development of a computational code, the work also presents a non-dimesionalisation analysis, boundary conditions and more importantly, all basic tests any computational method of this nature should verify in order to be reliable. Finally, the influence of confined geometries over the dynamics of standing capillary waves is analyzed, specially the effects of the boundaries parallel to the interface between the two phases of the fluid.

Keywords: Lattice Boltzmann method, Shan-Chen approach, two phase fluids, capillary waves, confined geometries, Computational Fluid Dynamics.

RESUMEN

'Implementación del Método de Malla de Boltzmann para el Análisis de Ondas Capilares en Geometrías Confinadas' presenta un código capaz de simular en 3 dimensiones un fluido bifásico utilizando el enfoque de Shan-Chen además del modelo de malla de Boltzmann. El trabajo presenta el análisis matemático pertinente que permite una comprensión justa del método y su validez, así como la derivación matemática y los conceptos físicos de las ecuaciones hidrodinámicas. Al centrarse en el desarrollo de un código computacional, el trabajo también presenta un análisis de no-desdimesionalización, condiciones de frontera y, lo que es más importante, todas las pruebas básicas que cualquier método computacional de esta naturaleza debe verificar para ser confiable. Finalmente, se analiza la influencia de las geometrías confinadas sobre la dinámica de las ondas capilares estacionarias, especialmente se estudian los efectos de las fronteras paralelas a la interfaz entre las dos fases del fluido.

Palabras clave: Método de Malla de Boltzmann, aproximación de Shan-Chen, fluido de dos fases, ondas capilares, geometrías confinadas, Dinámica de Fluidos Computacional.

Contents

Chapter 1

Introduction

Complex fluids are ubiquitous in natural and industrial processes, they can involve single component multiphase fluids such as water and vapor water, or multicomponent fluids, such as oil and water. The hydrodynamics and kinetics of these type of complex fluids present a wealth of physical problems of technological but also fundamental importance: wave dynamics, marine engineering, chemical engineering, the food processing industry, recovery of petroleum resources from reservoirs, non-aqueous phase liquid contamination of ground water, soil water behaviour, surface wetting phenomena, fuel cell operation and the movement and evolution of clouds [1] [2].

These physical problems represent an important challenge for both experimental an computational scientists. For the case or experiments, scientists encounter important limitations regarding the systems that they can analyze, for instance, a limited range of scales for the fluid velocity, temperature, time or length scale of the system. Thus, computational fluid dynamics (CFD) concerned with numerical solution to differential equations governing transport of mass, momentum and energy in moving fluids, has become, over the last four decades, a powerful area in fluid flow studies [3]. An inevitable consequence of the computational analysis of a two phase fluid system, which also adds another level of complexity to the problem, is the interface between these two fluids. Quality that also provides a rich variety of phenomena to investigate, specially in the field of micro and nanofluidics [4] [5].

From the interface between the fluids, comes the key to the physics of multiphase flows, the notion of surface tension, which is mesoscopic in nature. Surface tension is, at the same time, the starting point to some other interesting physical phenomena such as droplet coalescence, falling droplets and capillary phenomena [6] [7] [8] [9] [10] and some other where the lattice Boltzmann method (LBM) looks or has already been promising: impact of droplets on solid subtrates, droplets brake-up, capillarity instabilities and bouncing transitions, liquid fragmentation, water repellency on structured surfaces [11] [12] [13] [14] [15]. On the other hand, capillary waves, which are harmonic waves located in the interface between two phases and whose dynamics is governed by surface tension, acting as a

restoring force and fluid viscosity, is yet a physical phenomena new to lattice Boltzmann method, even when their scientific relevance was recognized years ago. The first attempt to give a scientific basis to this phenomenon was made by Benjamin Franklin and later shown by Lord Kelvin that the properties of these waves are determined by surface tension [16].

Therefore, this work focuses on the particularly challenging problem of analyzing capillary waves with the lattice Boltzmann method.

The dissertation presents a fully working three-dimensional lattice Boltzmann method code in FORTRAN 90, developed from scratch without the usage of any packages or libraries, that implements a Shan-Chen model that uses Guo's Forcing Scheme in order to simulate a two phase fluid that evolves a stationary capillary wave. A free version of the code is available in https://github.com/veneciachm/LatticeBoltzmannMethod.

Despite the existence of a wide rage of lattice Boltzmann method implementations available: from specialized academic packages [17][18][19] to very versatile open-source projects [20][21] as well as commercial applications [22][23], this work prioritizes the development of a computational code and the analysis of the method, not focusing precisely on the optimal performance of the implementation but rather readability and comprehension. Therefore, the code verifies all basic tests any numerical method should check about convergence and stability of the solution, as well as the basic benchmark cases a lattice Boltzmann method should present. Regarding the implementation of the Shan-Chen model for a two phase fluid, the work also includes tests for galilean invariance and the Laplace pressure test.

Lattice Boltzmann method along with Shan-Chen approach is characterized by the definition of two free parameters in numerical simulations: viscosity, by setting a timescale that dictates the relaxation of the system to equilibrium via collisions, and surface tension, through the definition of a temperature-like parameter in charge of phase coexistence. These two parameters control the behaviour of capillary waves. Hence, the work uses the possibility of analyzing them to provide a framework for the description of capillary waves based on the mesoscopical approach that the lattice Boltzmann method represents.

Another asset of this method is that the Shan-Chen approach is a straight forward way to model multiphase fluids without the need of an extra algorithm to track the evolution of interfaces, unlike the widely used Eulerian methods (e.g., finite difference method, finite volume method, etc.). Thus, interests are growing in adopting LBM in multiphase simulations as a mesoscopic interpretation of fluid phenomena through simple streaming-collision processes [24]. Considering in addition that any fluid interphase boundary is mesoscopic in nature [25], LBM becomes a strong candidate for the numerical analysis of capillary waves.

The dissertation is organized as follows. As the Navier-Stokes equations solver the

lattice Boltzmann method is, chapter 2 presents a reminder of the basic notions of hydrodynamics and classical statistical mechanics, thus given the kinetic nature of the method, chapter 2 also contains the study of the Chapman-Enskog analysis in charge of recovering the macroscopic behaviour of the system out of the mesoscopic approach that the lattice Boltzmann equation is. In chapter 3, I present all the necessary theory for a complete understanding of the method: from the discretisation of the governing equation, the introduction of forces -crucial to the implementation of then Shan-Chen model- to the analysis of nondimesionalisation, accuracy of the method and boundary conditions. A breakdown of the theory for the Shan-Chen model is presented in chapter 4. I also present in chapters 3 and 4 the basic benchmark tests in two and three dimensions studied for the correct implementation of the numerical method considering the inclusion to it of forces and the Shan-Chen approach. Chapter 5 presents the main results of this work, there I analyze and discuss the influence of confined geometries over the dynamics of standing capillary waves, making special emphasis over the effects of the boundaries parallel to the interface between the two phases of the fluid. Finally, I conclude this work with some conclusions and final remarks in chapter 6.

Chapter 2

Theoretical Background of the Method

A physical system such as a fluid, can be studied using different scales. In each scale, exist different interactions that control the dynamics of the system and, with it, different equations and regimes dictating the evolution of processes. See Fig. 2.1 for an schematic representation of the various regimes used to study the fluid dynamics.

Parting from the micro-scale, the system is considered to be a collection of N molecules that interact via two-body intermolecular potentials. If the size of the molecules s is much smaller than their mean interparticle separation, it is safe to consider the molecules as point-like structureless particles. Under this condition, the de Broglie length $\lambda = h/p$ of these particles is much smaller than any other length scale of the system, so that the classical Newton equations govern their dynamics, in the N-body regime. Upon specifying initial and boundary conditions, Newton equations will yield the entire state of the system. Nonetheless, N here is usually of the order of Avogradro number (10^{23}), only a cubic millimeter of air contains approximately 10^{16} particles [26], consequently this N-body approach to the system turns-out computationally impossible to solve. Fortunately, the physical observables this work is interested in are macroscopic (pressure, velocity, density of a fluid) and originate from an statistical average over a large number of individual molecules, therefore the need of the analysis of the system at different scales that will be described now: the lattice Boltzmann equation is based on statistical mechanics principles to solve the hydrodynamics of a fluid flow. Therefore, in the last section of this chapter, I will also discuss how this link between kinetic theory and hydrodynamics is established in the lattice Boltzmann equation.

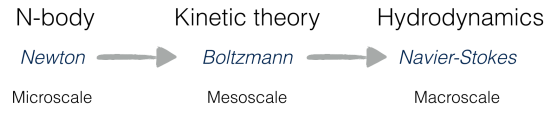

Figure 2.1: Scheme of the different relevant length-scales on which a fluid can be analyzed.

2.1 Hydrodynamics

This regime uses a continuous approach to the system where macroscopic variables such as velocity, pressure and density will give all the important properties of the dynamics. The continuous approach means that any small volume element in the fluid is supposed to be so large that it contains a very large number of molecules, enough to be considered statistically meaningful, but the volume yet small enough compared to the global dimension of the macroscopic domain where the fluid evolves. This volume element will be referred to as parcel of fluid or fluid element and its properties $\mathbf{u}$, $\mathbf{p}$ and ρ will be function of the spatial coordinates x, y, z of the parcel and time.

Equations governing the system come from conservation principles: mass, momentum and energy. Taking as a starting point the equation which describes the conservation of mass, consider a volume V_0. The mass contained in this volume is $\int_{V_0} \rho dV$ with $\rho = \rho(\mathbf{x}, t)$ the fluid density. The mass of fluid flowing with velocity $\mathbf{u} = \mathbf{u}(\mathbf{x}, t)$ in unit time through an element $d\boldsymbol{\sigma}$ of the surface bounding this volume is $\rho\mathbf{u} \cdot d\boldsymbol{\sigma}$. Considering $d\boldsymbol{\sigma}$ along the outward pointing normal, the total mass flowing out of V_0 per unit of time is

$$\oint \rho\mathbf{u} \cdot d\boldsymbol{\sigma} = \int \nabla \cdot (\rho\mathbf{u}) dV,$$

where Green's formula has been used, and the decrease per unit time in the mass of fluid in the volume V_0 can be written as

$$-\frac{\partial}{\partial t} \int \rho dV.$$

Therefore, equating these two expressions one obtains that

$$\frac{\partial}{\partial t} \int \rho dV = -\int \nabla \cdot (\rho\mathbf{u}) dV,$$

$$\int \left[\frac{\partial \rho}{\partial t} + \nabla \cdot (\rho\mathbf{u}) \right] dV = 0.$$

The later is valid for any volume, so the integrand must always vanish

$$\frac{\partial \rho}{\partial t} + \nabla \cdot (\rho\mathbf{u}) = 0. \tag{2.1}$$

This is the **equation of continuity** in differential form.

Similarly, considering the change of net momentum in or out of the fluid element, changes in pressure p and external body forces $\mathbf{F}$

$$\frac{d}{dt} \int_{V_0} \rho\mathbf{u} dV = -\oint_{\partial V_0} \rho\mathbf{u}\mathbf{u} \cdot d\boldsymbol{\sigma} - \oint_{\partial V_0} p d\boldsymbol{\sigma} + \int_{V_0} \mathbf{F} dV,$$

here **uu** denotes the outer product. Using the divergence theorem

$$\int_{V_0} \frac{\partial(\rho \mathbf{u})}{\partial t} dV = -\int_{V_0} \nabla \cdot (\rho \mathbf{u}\mathbf{u}) dV - \int_{V_0} \nabla p dV + \int_{V_0} \mathbf{F} dV,$$

results, once again, in an expression valid for any volume, the **Euler equation**

$$\frac{\partial(\rho \mathbf{u})}{\partial t} + \nabla \cdot (\rho \mathbf{u}\mathbf{u}) = -\nabla p + \mathbf{F}. \tag{2.2}$$

First obtained by L. Euler in 1755 is one of the fundamental equations of fluid dynamics [27].

Defining the momentum flux density tensor as

$$\Pi_{\alpha\beta} = \rho u_\alpha u_\beta - p\delta_{\alpha\beta}$$

equation (2.2) takes a more general form as the Cauchy momentum equation

$$\frac{\partial(\rho \mathbf{u})}{\partial t} + \nabla \cdot \mathbf{\Pi} = \mathbf{F}. \tag{2.3}$$

This equation only considers momentum transfer that is reversible. When considering the effect of energy dissipation due to internal friction (viscosity) and thermal conduction, the inclusion of additional terms in the equation describing this ideal fluid is necessary. Whereas the continuity equation remains valid whether this fluid is viscous or not, Euler's equation requires modifications when viscosity is to be considered.

To establish the new form of this equation, considering now internal friction the addition of a term $-\sigma'_{\alpha\beta}$ that represents this irreversible viscous transfer of momentum, is necessary. Writing then the momentum flux density tensor as follows

$$\Pi_{\alpha\beta} = \rho u_\alpha u_\beta - \sigma_{\alpha\beta}, \tag{2.4}$$

with the stress tensor

$$\sigma_{\alpha\beta} = -p\delta_{\alpha\beta} + \sigma'_{\alpha\beta} \tag{2.5}$$

and $\sigma'_{\alpha\beta}$ a tensor of rank two which takes the form [27][28]

$$\sigma'_{\alpha\beta} = \eta\left(\frac{\partial u_\alpha}{\partial x_\beta} + \frac{\partial u_\beta}{\partial x_\alpha} - \frac{2}{3}\delta_{\alpha\beta}\frac{\partial u_\gamma}{\partial x_\gamma}\right) + \eta_B \delta_{\alpha\beta}\frac{\partial u_\gamma}{\partial x_\gamma}. \tag{2.6}$$

Coefficients η and η_B referred to as coefficients of shear and bulk viscosity respectively, are independent of the fluid velocity, both positive and usually assumed isotropic and uniform*.

*Not the case for, for example, non-Newtonian fluids.

Finally, the substitution of equations (2.5) and (2.6) into (2.3) using (2.4) results in

$$\frac{\partial(\rho u_\alpha)}{\partial t} + \frac{\partial(\rho u_\alpha u_\beta)}{\partial x_\beta} = -\frac{\partial p}{\partial x_\alpha} + \frac{\partial}{\partial x_\beta}\left[\eta\left(\frac{\partial u_\alpha}{\partial x_\beta} + \frac{\partial u_\beta}{\partial x_\alpha}\right) + \left(\eta_B - \frac{2}{3}\eta\right)\frac{\partial u_\gamma}{\partial x_\gamma}\delta_{\alpha\beta}\right] + F_\alpha,$$

the **Navier-Stokes equation**.

Assuming viscosities are constant and regarding the flow as incompressible[†] ($\nabla\cdot\mathbf{u} = 0$), results in the **incompressible Navier-Stokes equation**

$$\rho\left(\frac{\partial}{\partial t} + \mathbf{u}\cdot\nabla\right)\mathbf{u} = -\nabla p + \eta\Delta\mathbf{u} + \mathbf{F}. \tag{2.7}$$

Up to this point, the dynamics of the fluid flow is described by 4 equations, one representing the conservation of mass and three for the conservation of momentum (one for each spatial component), but five unknown hydrodynamic variables (ρ, p, u_x, u_y and u_z), hence the need of another equation to close the system. An equation of state relates any state variable as density, pressure, temperature, internal energy or entropy to any other two of these state variables [28].

If the fluid is considered to have constant temperature T_0, the isothermal equation of state is a linear relationship between pressure p and density ρ:

$$p = \rho R T_0,$$

with R the specific gas constant. For this equation of state, the speed of sound is

$$c_s = \sqrt{RT_0},$$

therefore the pressure and density of the fluid are related by

$$p = c_s^2\rho. \tag{2.8}$$

Equation (2.8) provides the extra equation that closes the full system of equations and will be very useful in the formulation of the lattice Boltzmann method.

As mentioned in the introduction to this chapter and to this dissertation, the lattice Boltzmann method uses a mesoscopic approach to describe the dynamics of a fluid. I present next a reminder of the basic notions of kinetic theory.

[†]Since the lattice Boltzmann method used in this work will only work in the incompressible limit.

2.2 Kinetic Theory

"*I am conscious of being only an individual struggling weakly against the stream of time. But it still remains in my power to contribute in such a way that, the theory of gases is again revived, no too much will have to be rediscovered.* "
-Ludwig Boltzmann.

As stated before, pressure, velocity and density, originate from a statistical average over a large number of individual molecules. This statistical point of view can be explored at various levels of complexity. Considering the simplest one, i. e. the one-body kinetic level [26], its pivotal variable is the distribution function $f(\mathbf{x}, \boldsymbol{\xi}, t)$ which describes the probability density (density of particles) of finding a particle around the spatial position $\mathbf{x}$ at time t with velocity $\boldsymbol{\xi}$. Therefore the units of this function are

$$[f] = \frac{kg\ s^3}{m^6}.$$

In 1872, Ludwig Boltzmann derived the now referred to as the Boltzmann equation, an equation that describes the evolution of the distribution function in terms of microdynamic interactions,

$$\frac{\partial f}{\partial t} + \xi_\beta \frac{\partial f}{\partial x_\beta} + \frac{F_\beta}{\rho} \frac{\partial f}{\partial \xi_\beta} = \Omega(f) \tag{2.9}$$

with the source term $\Omega(f)$ as the collision operator. Within this equation, the first two terms describe the advection of the distribution function (streaming), the third term describes how forces affect the system and $\Omega(f)$ the local redistribution of f due to two body collisions, consequently the collision operator involves a two-body distribution function f_{12}. In fact, streaming and collision are the two main mechanisms dictating the dynamics of the system and also of the lattice Boltzmann method.

What is more, Boltzmann assumed the system was a dilute gas of point-like, structureless molecules interacting via a short-range two-body potential [26], this way collisions become localized and binary, which results into Boltzmann's closure assumption

$$f_{12} = f_1 f_2, \tag{2.10}$$

equivalent to assuming no correlations between molecules entering a collision.

As kinetic theory describes processes along their relaxation towards thermodynamic equilibrium, central to it is the concept of local equilibrium described by the associated distribution function f^{eq}. In this state, mathematically, the condition f^{eq} fulfills is

$$\Omega(f^{eq}) = 0.$$

This annihilation of the collision operator, leads to the detailed balance condition, meaning that any collision process is balanced by an inverse one, using equation (2.10), this translates into

$$f_1' f_2' = f_1 f_2,$$

with f' denoting the inverse collision process. Taking logarithms

$$\ln f_1' + \ln f_2' = \ln f_1 + \ln f_2,$$

hence $\ln f$ is a variable that does not change under the effect of collisions. This means that f must be a function only of dynamic collision invariants (mass, momentum and energy) [26]:

$$\ln f = A + B_\alpha u_\alpha + \frac{1}{2} C u^2$$

with A, B_α and C five lagrangian multipliers, obtained by imposing conservation of these dynamic collision invariants [26], conditions that are moments of the distribution function, which are integrals of f weighted with some function of $\boldsymbol{\xi}$:

0^{th} **moment** (mass density)

$$\rho(\mathbf{x}, t) = \int f(\mathbf{x}, \boldsymbol{\xi}, t) d^3\xi \tag{2.11}$$

1^{st} **moment** (momentum density)

$$\rho(\mathbf{x}, t)\mathbf{u}(\mathbf{x}, t) = \int \boldsymbol{\xi} f(\mathbf{x}, \boldsymbol{\xi}, t) d^3\xi \tag{2.12}$$

2^{nd} **moment** (total energy density)

$$\rho(\mathbf{x}, t) E(\mathbf{x}, t) = \frac{1}{2} \int |\boldsymbol{\xi}|^2 f(\mathbf{x}, \boldsymbol{\xi}, t) d^3\xi. \tag{2.13}$$

Thus, demanding that f^{eq} has the same moments as f, the equilibrium distribution function in d-dimension is [28]

$$f^{eq}(\rho, \mathbf{u}, \theta, \boldsymbol{\xi}) = \frac{\rho}{(2\pi)^{d/2}} e^{-\frac{(\boldsymbol{\xi}-\mathbf{u})^2}{2\theta}}, \tag{2.14}$$

with θ the temperature of the system. This distribution function is the Maxwell-Boltzmann distribution.

Note that f and f^{eq} are connected to the macroscopic variables via equations (2.11), (2.12) and (2.13).

To conclude with this section, let me go back to the collision term, one of the major problems when dealing with the Boltzmann equation. In order to facilitate numerical and

analytical solutions, simpler expressions of this collision term have been proposed. Any collision term must, as stated before:

1. Conserve mass, momentum and energy

   0^{th} **moment**

   $$\int \Omega(f) d^3\xi = 0 \tag{2.15}$$

   1^{st} **moment**

   $$\int \boldsymbol{\xi} \Omega(f) d^3\xi = \mathbf{0} \tag{2.16}$$

   2^{nd} **moment**

   $$\frac{1}{2} \int |\boldsymbol{\xi}|^2 \Omega(f) d^3\xi = 0. \tag{2.17}$$

2. Express the tendency of the system to approach to a Maxwellian distribution [29].

An expression that avoids most of the mathematical difficulties but meets the basic physics, including equations (2.15), (2.16) and (2.17), is the so-called BGK collision operator

$$\Omega(f) = -\frac{1}{\tau}(f - f^{eq}). \tag{2.18}$$

Proposed by Bhatnagar, Gross and Krook in 1954 [30], uses τ as the time scale associated with the speed at which the system (described by f) goes by means of collisions towards local equilibrium, f^{eq} (second condition stated before). This relaxation time, directly determines the fluid viscosity η. To illustate it with an example, think of a fluid with small viscosity, this means, as I will show in the next chapter, that τ is also small, hence $\Omega(f)$ will be big and the system will present a lot of collisions as intuition dictates.

Equation (2.9) together with equation (2.18) imply that

$$\frac{\partial f}{\partial t} + \xi_\beta \frac{\partial f}{\partial x_\beta} + \frac{F_\beta}{\rho} \frac{\partial f}{\partial \xi_\beta} = -\frac{1}{\tau}(f - f^{eq}) \tag{2.19}$$

which is one of the main equations of this work and the pillar of chapter 3.

2.3 From Kinetic Theory to Hydrodynamics: Chapman-Enskog analysis

Up to this point, this chapter has been all about kinetic theory and hydrodynamics as separate topics. In the last section I focused the discussion only on the kinetic regime driven mainly by local relaxation towards equilibrium and collisions but, how is this regime connected to fluid dynamics?

Fluid dynamics and, particularly, Navier Stokes equations, can be seen as the mean field picture of a perturbative treatment of the kinetic description of the system, where the perturbation parameter is the Knudsen Number [26]

$$Kn = \frac{l_{mfp}}{l}$$

defined as ratio between the mean free path and the shortest scale at which macroscopic variations are appreciated. This passage between kinetic theory and fluid dynamics is known as the Chapman-Enskog analysis.

Named after Sydney Chapman and David Eskog, a version of this analysis was expressed concisely by Enskog in 1917, while later, in 1939, Chapman combined it with his derivation in his book [31], into what is now known as the Chapman Enskog analysis.

As seen earlier in this chapter, the assumption $f \approx f^{eq}$ leads to the Euler momentum equation thus, any other macroscopic behaviour not represented in Euler equation, should be connected to the non-equilibrium part of the system:

$$f^{neq} = f - f^{eq}.$$

To determine the way on which this connection works, Chapman-Enskog expansion is used, consisting in general on a double expansion of both dependent and independent variables.

The former, the expansion around the dependent variable, i. e. the distribution function, reads

$$f = f^{(0)} + \epsilon f^{(1)} + \epsilon^2 f^{(2)} + ... \tag{2.20}$$

with ϵ^n referring to terms of order of Kn^n and identifying the first term $f^{(0)}$ as the equilibrium distribution function f^{eq}. Here, terms of lowest order result in the Euler momentum equation, whereas the higher order terms will represent corrections.

On the other hand, this analysis poses a multiple-scale expansion in time and space derivatives, whose basic idea is to represent the independent variables in terms of a hierarchy of scales that otherwise result in terms growing without bound. Hence, in this multiple scale expansion, each variable is $O(1)$ at its own relevant scale. This hierarchy suggests [26]

$$x = \frac{x^{(1)}}{\epsilon}, \qquad t = \frac{t^{(1)}}{\epsilon} + \frac{t^{(2)}}{\epsilon^2}.$$

The above induces the following representation of the differential operators [28]:

$$\begin{aligned} \delta t c_{k\alpha} \partial_\alpha f &= \delta t (\epsilon c_{k\alpha} \partial_\alpha^{(1)}) f, \\ \delta t \partial_t f &= \delta t (\epsilon \partial_t^{(1)} + \epsilon^2 \partial_t^{(2)}) f, \end{aligned} \tag{2.21}$$

where the expansion $\partial_t = \sum_{n=0}^{\infty} \partial_t^{(n)}$, is just a formal definition.

By introducing the following expansion

$$f(\mathbf{x} + \boldsymbol{\xi}\delta t, t + \delta t) = \sum_{n=0}^{\infty} \frac{\delta t^n}{n!} \mathbf{D}_t^{(n)} f(\mathbf{x}, t) \tag{2.22}$$

with $D_{t\alpha}^{(n)} \equiv (\partial_t + \xi_\alpha \partial_\alpha)^n$, Boltzmann Equation can be written as follows. Considering the ansatz that only the two lowest orders in Kn are significant when recovering the macroscopic behaviour of the system (for notation purposes $f(\mathbf{x}, t) = f$)

$$\underbrace{f + \delta t(\partial_t + \xi_\alpha \partial_\alpha) f + \frac{\delta t^2}{2}(\partial t + \xi_\alpha \partial_\alpha)^2 f + O(\delta t^3)}_{f(x_\alpha + \xi_\alpha \delta t, t + \delta t)} - f = -\frac{\delta t}{\tau}(f - f^{eq}), \tag{2.23}$$

canceling the respective terms and rearranging the equation, results in

$$\delta t \partial_t f + \delta t \xi_\alpha \partial_\alpha f + \frac{1}{2}[\delta t \partial_t f + \delta t \xi_\alpha \partial_\alpha f]^2 = -\frac{\delta t}{\tau}(f - f^{eq}).$$

Now substituting equations (2.21)

$$\delta t \epsilon \partial_t^{(1)} f + \delta t \epsilon^2 \partial_t^{(2)} f + \delta t \epsilon \xi_\alpha \partial_\alpha^{(1)} f + \frac{\delta t^2}{2}[\epsilon \partial_t^{(1)} + \epsilon^2 \partial_t^{(2)} + \epsilon \xi_\alpha \partial_\alpha^{(1)}]^2 f = -\frac{\delta t}{\tau}(f - f^{eq})$$

and also equation (2.20), considering that only the 2 lowest order terms in Kn will contribute:

$$\begin{aligned}\delta t \epsilon \partial_t^{(1)}(f^{(0)} + \epsilon f^{(1)}) + \delta t \epsilon^2 \partial_t^{(2)}(f^{(0)}) + \delta t \epsilon \xi_\alpha \partial_\alpha^{(1)}(f^{(0)} + \epsilon f^{(1)}) \\ + \frac{\delta t^2}{2}[\epsilon \partial_t^{(1)} + \epsilon^2 \partial_t^{(2)} + \epsilon \xi_\alpha \partial_\alpha^{(1)}]^2 (f^{(0)}) = -\frac{\delta t}{\tau}((f^{(0)} + \epsilon f^{(1)} + \epsilon^2 f^{(2)}) - f^{eq})\end{aligned}$$

finally results in

$$\begin{aligned}\delta t \epsilon \partial_t^{(1)} f^{(0)} + \delta t \epsilon^2 \partial_t^{(1)} f^{(1)} + \delta t \epsilon^2 \partial_t^{(2)} f^{(0)} + \delta t \epsilon \xi_\alpha \partial_\alpha^{(1)} f^{(0)} + \delta t \epsilon^2 \xi_\alpha \partial_\alpha^{(1)} f^{(1)} \\ + \frac{\delta t^2}{2}[\epsilon^2 \partial_t^{(1)^2} + 2\epsilon^2 \xi_\alpha \partial_t^{(1)} \partial_\alpha^{(1)} + \epsilon^2 \xi_\alpha^2 \partial_\alpha^{(1)^2}] f^{(0)} = -\frac{\delta t}{\tau}(f^{(0)} + \epsilon f^{(1)} + \epsilon^2 f^{(2)} - f^{eq})\end{aligned}. \tag{2.24}$$

Once the equation on which I will base the rest of the analysis has been derived , let us

remember that the relaxation process should conserve mass and momentum:

$$\int f^{eq} d^3\xi = \int f d^3\xi = \rho$$
$$\int \xi_\alpha f^{eq} d^3\xi = \int \xi_\alpha f d^3\xi = u_\alpha \rho$$

and that, given the supposition $f^{neq} = f - f^{eq}$, I can express

$$\int f^{neq} d^3\xi = 0, \qquad \int \xi_\alpha f^{neq} d^3\xi = 0,$$

which, together with equation (2.20), lead to

$$\int f^{(n)} d^3\xi = 0, \qquad \int \xi_\alpha f^{(n)} d^3\xi = 0 \quad \forall\ n \geq 1, \tag{2.25}$$

known as the conditions of solubility [31]. This mean that that corrections of order of ϵ and bigger, do not contribute to the local values of mass and momentum density [29].

Going back to equation (2.24), it can be sorted according to the order of magnitude of ϵ, and replaced by a set of equations arranged in a consecutive order of magnitude of this same parameter [32]:

$O(\epsilon^{\mathbf{0}})$: Relaxation towards local equilibrium with few collisions necessary to reach such equilibrium, a very fast process.

$$f^{(0)} = f^{eq} \tag{2.26}$$

$O(\epsilon^{\mathbf{1}})$: Sound waves and advection, a fast process but slower than relaxation towards local equilibrium [29].

$$\delta t \epsilon \partial_t^{(1)} f^{(0)} + \delta t \epsilon \xi_\alpha \partial_\alpha^{(1)} f^{(0)} = -\frac{\delta t}{\tau} \epsilon f^{(1)}$$

which simplifies to

$$\left(\partial_t^{(1)} + \xi_\alpha \partial_\alpha^{(1)}\right) f^{(0)} = -\frac{1}{\tau} f^{(1)}. \tag{2.27}$$

Taking the zero-th to second moments of this equation corresponding to equations (2.11), (2.12) and (2.13) and considering the conditions of solubility (2.25) one obtains:

0^{th} **moment:**

$$\partial_t^{(1)} \rho + \partial_\alpha^{(1)} \rho u_\alpha = 0, \tag{2.28}$$

which is the equivalent at $O(\epsilon^1)$ of the continuity equation.

1^{st} **moment:**

$$\int \left(\xi_\alpha(\partial_t^{(1)} + \xi_\alpha\partial_\alpha^{(1)})f^{(0)}\right) d^3\xi = -\int \frac{\xi_\alpha}{\tau} f^{(1)} d^3\xi$$

which using equation (2.26) results in

$$\partial_t^{(1)}(\rho u_\alpha) + \partial_\beta^{(1)}\Pi_{\alpha\beta}^{eq} = 0, \tag{2.29}$$

the $O(\epsilon^1)$ Euler equation.

2^{nd} **moment:** Following the same steps, the resulting equation is:

$$\partial_t^{(1)}\Pi_{\alpha\beta}^{eq} + \partial_\gamma^{(1)}\Pi_{\alpha\beta\gamma}^{eq} = -\frac{1}{\tau}\Pi_{\alpha\beta}^{(1)}, \tag{2.30}$$

where the moments are

$$\begin{aligned}
\Pi_{\alpha\beta}^{eq} &= \int f^{eq}\xi_\alpha\xi_\beta d^3\xi = \rho c_s^2\delta_{\alpha\beta} + \rho u_\alpha u_\beta, \\
\Pi_{\alpha\beta\gamma}^{eq} &= \int f^{eq}\xi_\alpha\xi_\beta\xi_\gamma d^3\xi = \rho c_s^2(u_\alpha\delta_{\beta\gamma} + u_\beta\delta_{\alpha\gamma} + u_\gamma\delta_{\alpha\beta}), \\
\Pi_{\alpha\beta}^{(1)} &= \int \xi_\alpha\xi_\beta f^{(1)} d^3\xi.
\end{aligned} \tag{2.31}$$

$O(\epsilon^2)$: This correction of second order in ϵ corresponds to diffusion processes which are considerably slower than sound waves and advection.

$$\begin{aligned}
&\delta t\epsilon^2\partial_t^{(1)}f^{(1)} + \delta t\epsilon^2\partial_t^{(2)}f^{(0)} + \delta t\epsilon^2\xi_\alpha\partial_\alpha^{(1)}f^{(1)} \\
&\qquad + \frac{\delta t^2}{2}[\epsilon^2\partial_t^{(1)^2} + 2\epsilon^2\xi_\alpha\partial_t^{(1)}\partial_\alpha^{(1)} + \epsilon^2\xi_\alpha^2\partial_\alpha^{(1)^2}]f^{(0)} = -\frac{\delta t}{\tau}\epsilon^2 f^{(2)} \\
&\partial_t^{(2)}f^{(0)} + (\partial_t^{(1)} + \xi_\alpha\partial_\alpha^{(1)})f^{(1)} + \underbrace{\frac{\delta t}{2}[\partial_t^{(1)^2} + 2\xi_\alpha\partial_t^{(1)}\partial_\alpha^{(1)} + \xi_\alpha^2\partial_\alpha^{(1)^2}]f^{(0)}}_{\circledast} = -\frac{1}{\tau}f^{(2)}
\end{aligned} \tag{2.32}$$

Let us focus on the term $\circledast$ for a moment. Applying $(\partial_t^{(1)} + \xi_\alpha\partial_\alpha^{(1)})$ to both sides of equation (2.27)[‡]:

$$\underbrace{\left(\partial_t^{(1)^2} + 2\xi_\alpha\partial_\alpha^{(1)}\partial_t^{(1)} + {\xi_\alpha}^2\partial_\alpha^{(1)^2}\right)f^{(0)}}_{\frac{2}{\delta t}\circledast} = -\frac{1}{\tau}(\partial_t^{(1)} + \xi_\alpha\partial_\alpha^{(1)})f^{(1)}.$$

[‡]Throughout all this analysis it is supposed that the changes in f are slow, occurring only on a macroscopic scale [28].

After substituting the later in equation (2.32) and doing some algebra one obtains

$$\partial_t^{(2)} f^{eq} + (\partial_t^{(1)} + \xi_\alpha \partial_\alpha^{(1)})(1 - \frac{\delta t}{2\tau}) f^{(1)} = -\frac{1}{\tau} f^{(2)}.$$

Taking its moments and considering again the conditions of solubility, the following relations arise:

0^{th} **moment:**

$$\partial_t^{(2)} \rho = 0 \tag{2.33}$$

1^{st} **moment:**

$$\partial_t^{(2)}(\rho u_\alpha) + \partial_\beta^{(1)} \left(1 - \frac{\delta t}{2\tau}\right) \Pi_{\alpha\beta}^{(1)} = 0 \tag{2.34}$$

these equations are interpreted as second order in ϵ corrections to the equations corresponding to $O(\epsilon)$ above.

Hence, assembling the moments of order zero of both $O(\epsilon)$ and $O(\epsilon^2)$, i.e. equations (2.28) and (2.33), I can obtain the correction to continuity equation:

$$(\epsilon \partial_t^{(1)} + \epsilon^2 \partial_t^{(2)})\rho + \partial_\alpha^{(1)} \rho u_\alpha = 0 \tag{2.35}$$

which, when reversing expansions in equation (2.21), will be zero, since it is exact already at $O(\epsilon)$, unlike momentum conservation equation as I will show next.

Doing the same, but now for the moments of order one, that is, equations (2.29) and (2.34)

$$(\epsilon \partial_t^{(1)} + \epsilon^2 \partial_t^{(2)})(\rho u_\alpha) + \epsilon \partial_\beta^{(1)} \Pi_{\alpha\beta}^{eq} = -\epsilon^2 \partial_\beta^{(1)} \left(1 - \frac{\delta t}{2\tau}\right) \Pi_{\alpha\beta}^{(1)}, \tag{2.36}$$

the needed corrections of $O(\epsilon^2)$ for momentum conservation equation with the unknown viscous stress tensor are found [28]:

$$\sigma'_{\alpha\beta} = -\left(1 - \frac{\delta t}{2\tau}\right) \Pi_{\alpha\beta}^{(1)}. \tag{2.37}$$

For the calculation of this perturbation moment, I refer to Appendix A.2.2 of [28]. Where using equation (2.30), they find an explicit expression for $\Pi_{\alpha\beta}^{(1)}$ in terms of $\mathbf{u}$, ρ and their derivatives. This explicit expression is

$$\Pi_{\alpha\beta}^{(1)} = -\tau \left[\underbrace{\rho c_s^2 (\partial_\beta^{(1)} u_\alpha + \partial_\alpha^{(1)} u_\beta)}_{\text{N-S viscous stress tensor}} - \underbrace{\partial_\gamma^{(1)} (\rho u_\alpha u_\beta u_\gamma)}_{\text{error of } O(u^3)} \right]. \tag{2.38}$$

The error term can be neglected for incompressible flows, that is, when the Mach number

is small. The Mach number

$$Ma = \frac{t_{sound}}{t_{conv}} = \frac{u}{c_s}$$

defines the ratio between the acoustic and advective scales. Then, the error term is neglected when $Ma^2 \ll 1$ or, what is equivalent, $u^2 \ll c_s^2$, reason why LBM is only valid for weakly compressible phenomena [33]. In simulations, a steady fluid flow with $Ma \leq 0.1$ is assumed to be incompressible [28]. Later in this work, I will mention more restrictions the method has to meet in order to simulate the correct physic of a system.

Once counting with all the ingredients to recover the macroscopic equations arising from this kinetic regime that represents lattice Boltzmann, insert, from equation (2.38), only the viscous stress tensor into equation (2.36) and reverse expansions in (2.21) to finally express continuity equation and Navier-Stokes equation:

$$\begin{aligned} \partial_t \rho + \partial_\gamma(\rho u_\gamma) &= 0, \\ \partial_t(\rho u_\alpha) + \partial_\beta(\rho u_\alpha u_\beta) &= -\partial_\alpha p + \partial_\beta\left(\eta[\partial_\beta u_\alpha + \partial_\alpha u_\beta]\right) \end{aligned} \tag{2.39}$$

with

$$p = \rho c_s^2, \qquad \eta = \rho c_s^2\left(\tau - \frac{\delta t}{2}\right), \qquad \eta_B = \frac{2}{3}\eta. \tag{2.40}$$

The same macroscopic equations can be found by using more general collision operators. Here, using Boltzmann equation along with the BGK collision operator, a formula, equation (2.40), was obtained to correlate the LBM model parameters to the kinematic viscosity implicitly implemented in LBM simulations. It is important to mention that this theoretical derivation of the viscosity coefficient is only applicable in the domain of validity of the Chapman-Enskog analysis, that is, near local equilibrium [28].

In the next chapter I present all the necessary theory for a complete understanding of the method.

Chapter 3

Lattice Boltzmann Method

In this chapter, I present an overview of the Lattice Boltzman Method with the main elements of lattice Boltzmann equation theory, including the derivation of the lattice Boltzmann equation and the discretisation of velocity space, physical space and time. In particular, I only analyze the Bhatnagar-Gross-Krook model introduced in 1954. This Lattice Bhatnagar-Gross-Krook scheme (LBGK) is the ideal lattice Boltzmann model in terms of simplicity and effectiveness. Next, I include an analysis of the method, including non-dimensionalisation, a review of its accuracy, stability and efficiency as well as the extension of the model to 3 dimensions and the analysis of Boundary Conditions. Later, I discuss the forcing scheme in 3D. Finally, some benchmark cases to the method are presented.

3.1 Lattice Boltzmann Equation

Lattice Gas Cellular Automata as the precursor of the lattice Boltzmann method, is described by kinetic equations of the type

$$f_k(\mathbf{x} + \hat{\mathbf{c}}_k \Delta t, t + \Delta t) = f_k(\mathbf{x}, t) + \Omega_k. \tag{3.1}$$

This form of discrete equation expressing that particles in $f_k(\mathbf{x}, t)$ move with velocity $\hat{\mathbf{c}}_k$ to a point $\mathbf{x} + \hat{\mathbf{c}}_k \Delta t$ in the neighborhood of $\mathbf{x}$ at the next time step, being affected at the same time by a collision operator Ω_k, is referred to as lattice Boltzmann equation, with its basic quantity being the discrete-velocity distribution function $f_k(\mathbf{x}, t)$. The correspondence of equation (3.1) to the Boltzmann equation is established by discretising Boltzmann equation in velocity space, physical space and time. Hence, all the argument variables of f_k are discrete in comparison to those of the continuous distribution function. Velocity space is dicretised by introducing a finite set of velocities $\hat{\mathbf{c}}_k$ as follows.

3.1.1 Discretisation in velocity space

Any sufficiently well-behaved continuous function $f(\mathbf{x}) \in \mathbb{R}$ can be represented as a series of Hermite polynomials in d dimensions ($\mathbf{x} \in \mathbb{R}^d$) as

$$f(\mathbf{x}) = w(\mathbf{x}) \sum_{n=0}^{\infty} \frac{1}{n!} \mathbf{a}^{(n)} \cdot \mathbf{H}^{(n)}(\mathbf{x})$$

with

$$\mathbf{a}^{(n)} = \int f(\mathbf{x}) \mathbf{H}^{(n)}(\mathbf{x}) d^d x \tag{3.2}$$

a tensor of rank n and

$$\mathbf{H}^{(n)}(\mathbf{x}) = (-1)^n \frac{1}{w(\mathbf{x})} \nabla^{(n)} w(\mathbf{x}), \qquad w(\mathbf{x}) = \frac{1}{(2\pi)^{d/2}} e^{-\frac{x^2}{2}}. \tag{3.3}$$

Applying the Hermite series expansion to the equilibrium distribution function and limiting this expansion to the $N - th$ order, results in

$$f^{eq}(\rho, \mathbf{u}, \theta, \boldsymbol{\xi}) \approx w(\boldsymbol{\xi}) \sum_{n=0}^{N} \frac{1}{n!} \mathbf{a}^{(n),eq}(\rho, \mathbf{u}, \theta) \cdot \mathbf{H}^{(n)}(\boldsymbol{\xi}), \tag{3.4}$$

$$\mathbf{a}^{(n),eq}(\rho, \mathbf{u}, \theta) = \int f^{eq}(\rho, \mathbf{u}, \theta, \boldsymbol{\xi}) \mathbf{H}^{(n)}(\boldsymbol{\xi}) d^d \xi, \tag{3.5}$$

where ρ is the density of the parcel of fluid, $\mathbf{u}$ the macroscopic velocity, θ the temperature and $\boldsymbol{\xi}$ the velocity of the particles in f. The equilibrium distribution function explicitly up to the second order, $N = 2$ in $\boldsymbol{\xi}$ from equation (3.4), is

$$f^{eq}(\rho, \mathbf{u}, \theta, \boldsymbol{\xi}) \approx w(\boldsymbol{\xi}) \rho \left[1 + \xi_\alpha u_\alpha + \frac{1}{2} (u_\alpha u_\beta + (\theta - 1)\delta_{\alpha\beta})(\xi_\alpha \xi_\beta - \delta_{\alpha\beta}) \right] = w(\boldsymbol{\xi}) \rho Q(\mathbf{u}, \theta, \boldsymbol{\xi}), \tag{3.6}$$

note that $f^{eq}(\rho, \mathbf{u}, \theta, \boldsymbol{\xi}) = \frac{\rho}{(2\pi)^{d/2}} e^{-\frac{(\boldsymbol{\xi} - \mathbf{u})^2}{2\theta}}$ has the same form as the weight function in (3.3) with the argument $\mathbf{x} = \frac{\boldsymbol{\xi} - \mathbf{u}}{\sqrt{\theta}}$. This way, (3.5) takes the form:

$$\begin{aligned} \mathbf{a}^{(n),eq} &= \frac{\rho}{\theta^{d/2}} \int \underbrace{w\left(\frac{\boldsymbol{\xi} - \mathbf{u}}{\sqrt{\theta}} \right)}_{\eta} \mathbf{H}^{(n)}(\boldsymbol{\xi}) d^d \xi \\ &= \rho \int w(\eta) \mathbf{H}^{(n)}(\sqrt{\theta}\eta + \mathbf{u}) d^d \eta. \end{aligned} \tag{3.7}$$

Relation that will provide the discrete velocity set necessary to discretise the velocity space, replacing $\boldsymbol{\xi}$ by a discrete set of velocities $\{\boldsymbol{\xi}_k\}$.

First, let us consider the Gauss-Hermite quadrature rule that allows us to calculate the value of integrals of the form $\int w(\mathbf{x})P^{(n)}(\mathbf{x})d^dx$, $P^{(n)}(\mathbf{x})$ a polynomial of order N, by considering its values only in certain points $\mathbf{x}_k$ roots of the Hermite polinomial:

$$\mathbf{H}^{(n)}(x_{\alpha k}) = 0, \qquad \alpha = 1, \ ... \ , d.$$

That is

$$\int w(\mathbf{x})P^{(N)}(\mathbf{x})d^dx = \sum_{k=1}^{N} \mathrm{w}_k P^{(N)}(\mathbf{x}_k), \quad \mathrm{w}_k = \frac{n!}{(nH^{(n-1)}(x_k))^2}.$$

Instead of using (3.7) with the Gaussian-Hermite quadrature, go back to (3.5) and substitute (3.6):

$$\mathbf{a}^{(n),eq} = \int f^{eq}(\boldsymbol{\xi})\mathbf{H}^{(n)}(\boldsymbol{\xi})d^d\xi = \rho \int w(\boldsymbol{\xi})Q(\boldsymbol{\xi})\mathbf{H}^{(n)}(\boldsymbol{\xi})d^d\xi = \rho \sum_{k=1}^{n} \mathrm{w}_k Q(\boldsymbol{\xi}_k)\mathbf{H}^{(n)}(\boldsymbol{\xi}_k). \quad (3.8)$$

Now, defining n quantities, each related to one velocity direction ξ_k as

$$f_k^{eq}(\mathbf{x}, t) = \mathrm{w}_k \rho(\mathbf{x}, t) Q(\mathbf{u}(\mathbf{x}, t), \theta(\mathbf{x}, t), \boldsymbol{\xi}_k) \quad (3.9)$$

in such a way that instead of a continuous function I have a finite set of them discretised in velocity space. Hence equation (3.6) will take the following form

$$f_k^{eq} = \mathrm{w}_k \rho \left(1 + \xi_{k\alpha}u_\alpha + \frac{1}{2}(u_\alpha u_\beta + (\theta - 1)\delta_{\alpha\beta})(\xi_{k\alpha}\xi_{k\beta})\right). \quad (3.10)$$

This discrete set of equilibrium distribution functions, satisfies the same conservation laws that its continuous version [28].

From the discretised Hermite series expansion in equation (3.8), n is the required number of abscissae suffiecient to obtain the correct macroscopic conservation laws. For this case, at least $n = 3$, therefore, the abscissae are given by the roots of $H^{(3)}(\xi_{k\alpha})$, $\alpha = 1, .., d$.

Abscissae suitable for LB simulations of the Navier-Stokes equation in $d = 2$ and $d = 3$ appear in Table 3.1 respective to $D2Q9$ and $D3Q19$ velocity sets.

Many of these abscissae contain factors of $\sqrt{3}$, so one simplification to equation (3.10) can be

$$\hat{\mathbf{c}}_k = \frac{\boldsymbol{\xi}_k}{\sqrt{3}}.$$

Another common simplification is the isothermal assumption that removes temperature of the equation by implying $\theta = 1$. Finally, considering the isothermal speed of sound, rewrite

Dimension	Number of abscissae	Abscissae	Weights
D	q	x_k	w_k
2	9	$(0,0)$	4/9
		$(0,\pm\sqrt{3}),(\pm\sqrt{3},0)$	1/9
		$(\pm\sqrt{3},\pm\sqrt{3})$	1/36
3	19	$(0,0,0)$	1/3
		$(\pm\sqrt{3},0,0),(0,\pm\sqrt{3},0),(0,0,\pm\sqrt{3})$	1/18
		$(\pm\sqrt{3},\pm\sqrt{3},0),(\pm\sqrt{3},0,\pm\sqrt{3}),(0,\pm\sqrt{3},\pm\sqrt{3})$	1/36

Table 3.1: Abscissae and weights from exact integration of 2D and 3D polynomials.

(3.10) as

$$f_k^{eq} = \mathrm{w}_k\rho\left(1 + \frac{\hat{c}_{k\alpha}u_\alpha}{c_s^2} + \frac{u_\alpha u_\beta(\hat{c}_{k\alpha}\hat{c}_{k\beta} - c_s^2\delta_{\alpha\beta})}{2c_s^4}\right), \tag{3.11}$$

the equilibrium distribution function that will be used and one of the most important equations in this work and LB theory in general. Note that it depends only on the local quantities ρ and $\mathbf{u}$. Now, discretising the distribution function in the same way as the equilibrium distribution function, the conservation laws for mass and momentum will be still satisfied. Then using Gauss-Hermite rule:

$$\begin{aligned}\mathbf{a}^{(n)}(\mathbf{x},t) &= \int f(\mathbf{x},\hat{\mathbf{c}},t)\mathbf{H}^{(n)}(\hat{\mathbf{c}})d^d\hat{c} = \int \frac{w(\hat{\mathbf{c}})}{w(\hat{\mathbf{c}})} f(\mathbf{x},\hat{\mathbf{c}},t)\mathbf{H}^{(n)}(\hat{\mathbf{c}})d^d\hat{c} \\ &\approx \sum_{k=1}^{q} \frac{\mathrm{w}_k}{w(\hat{\mathbf{c}}_k)} f(\mathbf{x},\hat{\mathbf{c}}_k,t)\mathbf{H}^{(n)}(\hat{\mathbf{c}}_k) = \sum_{k=1}^{q} f_k(\mathbf{x},t)\mathbf{H}^{(n)}(\hat{\mathbf{c}}_k)\end{aligned}$$

with f_k the population of particles moving in the $\hat{\mathbf{c}}_k$ direction:

$$f_k(\mathbf{x},t) = \frac{\mathrm{w}_k}{w(\hat{\mathbf{c}}_k)} f(\mathbf{x},\hat{\mathbf{c}}_k,t).$$

This discretised version of f is governed by the discrete * Boltzmann equation:

$$\frac{\partial f_k(\mathbf{x},t)}{\partial t} + \hat{\mathbf{c}}_k \cdot \nabla f_k(\mathbf{x},t) = \Omega(f_k(\mathbf{x},t)), \qquad k = 1,..,q. \tag{3.12}$$

Note that this is the same equation as the one introduced in Chapter 2, equation (2.9), but in a version with discrete velocity space $\boldsymbol{\xi} \to \hat{\mathbf{c}}$, and without forces, which will be introduced later.

Some remarks about this equation:

- The number of velocities in a model is given by the parameter q, whereas its dimension by d, hence the notation DdQq. The velocity sets that I use in this work, are

*Not discretised Boltzmann equation, which I will introduce in the next section by discretising physical space and time.

i	0	1	2	3	4	5	6	7	8
w_k	$\frac{4}{9}$	$\frac{1}{9}$	$\frac{1}{9}$	$\frac{1}{9}$	$\frac{1}{9}$	$\frac{1}{36}$	$\frac{1}{36}$	$\frac{1}{36}$	$\frac{1}{36}$
$\hat{c}_{kx}$	0	+1	0	−1	0	+1	−1	−1	+1
$\hat{c}_{ky}$	0	0	+1	0	−1	+1	+1	−1	−1

Table 3.2: Components of the D2Q9 velocity set $\{\hat{\mathbf{c}}_k\}$. In this table $\hat{\mathbf{c}}_k = (\hat{c}_{kx}, \hat{c}_{ky})$ and the weights w_k verify restrictions imposed in equations (3.14).

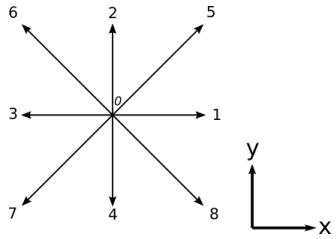

Figure 3.1: D2Q9 computational molecule. The arrows correspond to each $\hat{c}_k$, where k = 0, ..., 8.

D2Q9 and D3Q19. Figures. 3.1 and 3.2 show a schematic version of this velocity sets, while the explicit values for D2Q9 with its respective weights are given in Table 3.2. Further on I will treat with more detail the three dimensional case.

- The macroscopic moments of this discrete equation are finite sums instead of the integrals in the velocity space of the continuous version of the equation shown in equations (2.11) and (2.12) :

$$\begin{aligned} \rho &= \sum_{k=1}^{q} f_k = \sum_{k=1}^{q} f_k^{eq}, \\ \rho\mathbf{u} &= \sum_{k=1}^{q} f_k \hat{\mathbf{c}}_k = \sum_{k=1}^{q} f_k^{eq} \hat{\mathbf{c}}_k. \end{aligned} \tag{3.13}$$

- Regardless of the velocity set used, mass and momentum conservation, as well as the rotational isotropy of the lattice [†], require the isotropy of moments of the Hermite-

[†]As a Navier-Stokes solver, all moments of the Hermite-weights up to the fifth order must be isotropic.

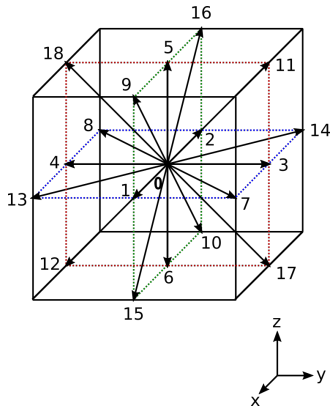

Figure 3.2: D3Q19 computational molecule. The arrows correspond to each $\hat{c}_k$, where $k = 0, ..., 18$.

weights up to the fifth order:

$$\begin{aligned}
\sum_{k=0}^{q} w_k &= 1, \\
\sum_{k=0}^{q} w_k c_{k\alpha} &= 0, \\
\sum_{k=0}^{q} w_k c_{k\alpha} c_{k\beta} &= c_s^2 \delta_{\alpha\beta,} \\
\sum_{k=0}^{q} w_k c_{k\alpha} c_{k\beta} c_{k\gamma} &= 0, \\
\sum_{k=0}^{q} w_k c_{k\alpha} c_{k\beta} c_{k\gamma} c_{k\mu} &= c_s^4 (\delta_{\alpha\beta}\delta_{\gamma\mu} + \delta_{\alpha\gamma}\delta_{\beta\mu} + \delta_{\alpha\mu}\delta_{\beta\gamma}), \\
\sum_{k=0}^{q} w_k c_{k\alpha} c_{k\beta} c_{k\gamma} c_{k\mu} c_{k\nu} &= 0,
\end{aligned} \tag{3.14}$$

with $q = 9$ for 2 dimensions and $q = 19$ for 3.

- Finally, the discrete version of the Bhatnagar-Gross-Krook collision operator,

$$\Omega_k = -\frac{f_k - f_k^{eq}}{\tau} \tag{3.15}$$

portrays its property of mass and momentum conservation, given the relations for

macroscopic moments in equation (3.13) [‡]. It also portrays the tendency of the system to approach its equilibrium state after a time τ, hence the name of this parameter, the relaxation time.

- Equation (3.12) is still continuous in space and time.

In the following, I will present the discretised version of this discrete equation, that is, once having an equation in a discrete velocity space (discrete equation) now follows the discretised equation which includes the discretisation in physical space and in time.

3.1.2 Discretisation in space and time

The spatial and temporal discretisation will define the computational *lattice* the numerical method will work on, leaving then aside the continuous domain on which the Boltzmann Equation is defined. Hence, for a continuous spatial domain $\mathbf{x} \in [\mathbf{x}_{min}, \mathbf{x}_{max}]$, taking the x-axis as an example, an uniform discretisation is

$$\Delta x = \frac{x_{max} - x_{min}}{N_x - 1}, \tag{3.16}$$

with $N_{x,y,z}$ the number of *lattice sites* along each spatial direction. Such lattice sites are defined by

$$x_i = x_{min} + i\,\Delta x, \qquad i = 0,\ ...,\ N_x - 1. \tag{3.17}$$

The temporal discretisation works the same way. Defining each time-step as

$$\Delta t = \frac{t_{max} - t_{min}}{N_t - 1}, \tag{3.18}$$

the discretised Boltzmann Equation will be now solved only in the following N_t time-steps:

$$t_n = t_{min} + n\,\Delta t, \qquad n = 0,\ ...,\ N_t - 1, \tag{3.19}$$

and not anymore in the continuous temporal domain.

Once the physical and temporal domains have been discretised, it is the turn for equation

[‡]This because of the linear form of the collision operator:

$$\sum_k \Omega_k \propto \sum_k (f_k - f_k^{eq}) = 0$$
$$\sum_k \mathbf{\Omega}_k \hat{\mathbf{c}}_k \propto \sum_k (f_k \hat{\mathbf{c}}_k - f_k^{eq} \hat{\mathbf{c}}_k) = \mathbf{0}$$

(3.12) which , combined with the BGK collision operator from equation (3.13), is

$$\frac{\partial f_k(\mathbf{x},t)}{\partial t} + \hat{\mathbf{c}}_k \cdot \nabla f_k(\mathbf{x},t) = -\frac{f_k(\mathbf{x},t) - f_k^{eq}(\mathbf{x},t)}{\tau}. \tag{3.20}$$

This is a first order hyperbolic partial differential equation, that will be solved by using the method of characteristics, assuming the existence of a parameter χ that parametrises a trajectory along which the PDE becomes an ordinary differential equation (ODE).

See Appendix A for the full mathematical analysis, which results into the **Lattice Bhatnagar Gross Krook equation** (a special case of the lattice Boltzmann equation that uses the BGK collision operator) discretised in velocity space, physical space and time:

$$\underbrace{f_k(\mathbf{x} + \hat{\mathbf{c}}_k \Delta t, t + \Delta t)}_{\text{streaming}} = f_k(\mathbf{x},t) + \underbrace{\frac{\Delta t}{\tau}\left(f_k^{eq}(\mathbf{x},t) - f_k(\mathbf{x},t)\right)}_{\text{collision}}. \tag{3.21}$$

- In this lattice Boltzmann equation, also referred to as Lattice BGK equation, the collision term is evaluated locally and has only one streaming step per lattice velocity $\hat{\mathbf{c}}_k$. This stream-collide interpretation is a result of the Lagrangian character of the equation [34].

- Although this scheme is first order accurate in time, a second order approximation of this particular integral (equation (A.5)) leads to the same form of LBE, thus, equation (3.21) is actually second order accurate in time [28].

- Even when it can be derived from the Boltzmann equation, the entire idea of LBM has its origins in lattice gas models which solved a Lattice Gas Boltzmann equation (specifically Lattice Gas Cellular Automata). Then, in order to get rid mainly of statistical noise but also other problems that these Lattice Gas presented, the idea of assuming that particle populations were only either zero or one was introduced [35] by using instead a particle distribution function. In other words, lattice Boltzmann equation was originally constructed empirically as an extension of Lattice Gas Automata and later shown that a direct derivation from Boltzmann equation is possible. Hence the approach used here, is also useful for ensuring that the LBE reproduces the correct continuum behaviour.

3.2 Lattice Boltzmann Method

Overall, I have described the basic equations of the lattice Boltzmann method, making emphasis over the collision and streaming steps. Now, I will summarize the general steps of the lattice Boltzmann method algorithm, after initializing the system by specifying the macroscopic moments from equation (3.13):

1. Construct the equilibrium distribution function at this current time-step from equation (3.11).

2. Perform collision and streaming as indicated in the Lattice Bhatnagar Gross Krook equation (3.21).

3. Consider boundary conditions (this topic is covered ahead in this section).

4. Compute macroscopic fields again as indicated in equation (3.13).

5. Increase the time-step to $t + \Delta t$ and go back to step 1 of this list.

Note that the order of these steps is important since the later steps depend on the earlier ones. In the next sections I will cover some important details for a successful implementation of this method.

3.2.1 Non-Dimensionalisation

This section will show how to convert parameters from the physical world, which will be referred to as dimensionalised values, to their respective values in simulations, i. e. non-dimesionalised. First of all, it is important to notice how in physics all phenomena are independent of units, since units are nothing but a human construct. Therefore, and by the very concept of these units, what matters to our analysis are ratios of the physical quantities. In particular, the physical outcome should not depend on whether I use one set of units, another or even dimensionless quantities. Nevertheless, it is always important and fundamental to be able to represent the results of our simulations in actual physical units. In this work and for the sake of convenience, I shall refer to the MKS system.

Non-dimensionalisation is achieved by dividing a quantity with units by a chosen reference quantity with the same units, the result is a number which I will call the *lattice value* of the quantity in a simulation which will be in lattice units with the reference quantity as the conversion factor, C. If I use a $\star$ to denote the non-dimensionalised quantity, then for example, for the especial case of a quantity with units of length, I have:

$$l^\star = \frac{l}{C_l} \tag{3.22}$$

with l the length in meters, C_l the conversion factor and $l^\star$ the lattice length. One of the purposes of this section is to learn how to chose these conversion factors C appropriately.

In general, a mechanical quantity, say q, has dimensions that turn out to be a combination of length, time and mass. From here, I conclude that these three fundamental dimensions are sufficient to generate the dimension that any mechanical quantity may have. So with the only requirement of exactly three independent conversion factors, it is possible to

define a unique non-dimensionalisation scheme. From now on, any set of three independent conversion factors will be a set of basic conversion factors.

The selection of these basic conversion factors is arbitrary, but in LBM one usually takes

$$C_l, \quad C_t, \quad (or \ C_u) \quad and \quad \rho. \tag{3.23}$$

as the conversion factor for distance, time (or velocity) and density respectively, in charge of re-scaling a simulation value to its respective parameter in the physical world.

To argue that all that matters to us scientists are ratios of a physical quantity, I turn to the Law of Similarity [27]: flows which can be obtained from one another by simply changing the unit of measurement of co-ordinates and velocities are said to be similar. Let us commence with an example from geometry. Just as it is said that bodies of the same shape are geometrically similar when they can be obtained from one another by only changing all their linear dimensions in the same ratio, the same logic can be applied to the study of fluids motion. Same physical properties will be measured on the system, as long as they are re-scaled by the appropriate factors.

Considering steady flows and supposing incompressible fluids, from the parameters that characterize the fluid itself, only the kinematic viscosity $\nu = \eta/\rho$ appears in the equations of hydrodynamics (Navier-Stokes equations). On these equations and when incompressibility is supposed, the unknown function that has to be determined is the velocity $\mathbf{u}$. Moreover, the flow depends, through the boundary conditions, on the shape and dimensions of the body through which the fluid is moving and on its velocity field. Since the shape of the body is assumed known, its geometrical properties as treated before, are determined by one linear dimension, say l. Then, any flow is specified by these three parameters:

$$\nu, \quad \mathbf{u}, \quad l$$

with the following dimensions:

$$[\nu] = \frac{m^2}{sec}, \quad [u] = \frac{m}{sec}, \quad [l] = m.$$

It is easy, then, to verify that the only dimensionless quantity that can be formed by the above three, is:

$$Re = \frac{ul}{\nu} = \frac{\rho ul}{\eta} \tag{3.24}$$

namely, the Reynolds number. Named by Arnold Sommerfeld after Osborne Reynolds, who popularized its use in 1883.

Re being the only dimensionless number, any other dimensionless parameter can be written as a function of it, including the velocity field obtained by solving the equation of incompressible flow and which is given by a function of the form

$$\mathbf{v} = \mathbf{u}\ \mathcal{U}(r/l, Re). \tag{3.25}$$

Lengths will be now measured in terms of l, and velocities in terms of u. i.e. I introduce the dimensionless quantities r/l and v_i/u_i, with r and v_i the new reference quantities. It is seen from these expressions that, in two different flows of the same type, the velocities (v_i/u_i) are the same function of (r/l) if the Reynolds number is the same for each flow. Then, now once introduced the Reynolds number, the law of similarity can be reformulated: **flows of the same type with the same Reynolds number are said to be similar**.

Here, l and $\mathbf{u}$ are the typical length and velocity scales in the system and ρ, ν and η are the density, kinematic viscosity and dynamic viscosity of the fluid.

To ensure that the result of our simulations can be applied to any two equivalent physical systems, the Reynolds number must be identical in both unit systems, dimensionalised and non-dimensionalised, that is, the quantities in reality (l, u and ν) and the quantities in our simulations (l^*, u^* and ν^*) :

$$Re = \frac{l^\star u^\star}{\nu^\star} = \frac{lu}{\nu} \tag{3.26}$$

or, what is equivalent:

$$\frac{C_l C_u}{C_\nu} = 1. \tag{3.27}$$

This way, the law of similarity for the Reynolds number, uniquely defines the relation of the conversion factors for viscosity, length and velocity, and with them, the expression of any other conversion factor is unique as a combination of the basic ones.

On account of this, it should be acknowledged that some important quantities that one has to keep in mind while performing LBM simulations (see equation (3.23)), are Δx, the distance between neighboring lattice sites in length units (meters in case of MKS), Δt, the physical length of a time step, τ the BGK relaxation parameter (both in time units, seconds on MKS) and the dimensionless fluid density $\rho^\star$. Here, it is useful to remember that the **physical density** of an incompressible fluid is constant, while the **LB density can fluctuate**, reason why, its average value is usually set to unity, $\rho_0^\star = 1$ (situation that will change in the case of multiphase fluids). Another important quantity is the typical simulated velocity $u^\star$, which is usually part of the simulation output and not an input parameter, even though some boundary conditions require the specification of this velocity at the boundary. Sometimes it is important to estimate the magnitude of $u^\star$ before the simulation in order to avoid unstable situations or very long computing times.

One more important quantity to consider is the speed of sound, its physical value can be defined as

$$C_s = c_s \frac{\Delta x}{\Delta t}, \tag{3.28}$$

where the capital denotes the physical value and c_s the dimensionless grid value. It can be

shown ([28] Secc. 12.1) that in the D1Q3, D2Q9, D3Q15, D3Q19 and D3Q27 velocity sets, c_s represents the isothermal model's speed of sound with $c_s^2 = \frac{1}{3}\frac{\Delta x^{\star 2}}{\Delta t^{\star 2}}$. Hence, in the standard LBM, where $\Delta x^\star/\Delta t^\star = 1$ in considered, the lattice speed of sound is $c_s = \sqrt{1/3} \approx 0.577$. In addition, in order to work in the quasi-incompressible limit, all simulated velocities of any system have to be significantly smaller, $u^\star \ll c_s$. In practice this means that the lattice Boltzmann method works around $u^\star \approx 0.2$ [28].

Later I will impose more conditions on this parameters in order to ensure the stability of our simulations. But first, I have to relate all physical parameters mentioned above to their counterparts in lattice units and vice versa.

As mentioned, a very usual and recommended choice is to settle

$$\Delta x^\star = \Delta t^\star = 1 \;\; and \;\; \rho^\star = 1, \tag{3.29}$$

choices that lead to

$$C_l = \Delta x, \quad C_t = \Delta t, \quad C_\rho = \rho \tag{3.30}$$

and

$$\tau = \tau^\star C_t = \tau^\star \Delta t \tag{3.31}$$

with the unique combination of

$$C_u = \frac{C_l}{C_t} = \frac{\Delta x}{\Delta t} \tag{3.32}$$

after all, $\Delta x, \Delta t$ and ρ form a unique set of basic conversion factors.

Viscosity. One notices the importance of the kinematic viscosity in simulations the moment one understand the relevance of the Reynolds number. From [28]

$$\eta = \rho C_s^2 \left(\tau - \frac{\Delta t}{2}\right) \tag{3.33}$$

the kinematic viscosity is obtained

$$\nu = C_s^2 \left(\tau - \frac{\Delta t}{2}\right) \tag{3.34}$$

therefore

$$\nu = c_s^2 \frac{\Delta x^2}{\Delta t^2}\left(\tau^\star \Delta t - \frac{\Delta t}{2}\right) = c_s^2 \left(\tau^\star - \frac{1}{2}\right)\frac{\Delta x^2}{\Delta t} \tag{3.35}$$

where clearly

$$[\nu] = \frac{m^2}{s}$$

so that

$$\nu^\star = c_s^2(\tau^\star - \frac{1}{2}), \tag{3.36}$$

is the dimensionless viscosity.

Pressure. From the equation of state of the LB fluid, equation (2.8),

$$p = {c_s}^2\rho. \tag{3.37}$$

However only the pressure gradient appears in the Navier-Stokes equation, so only the pressure changes matter [28]. Nottice that total pressure p does appear in the energy equation but this equation is not relevant for non-thermal LB models as the one used in this work, earlier in this chapter the isothermal assumption was mentioned when temperature was set to a constant, $\theta = 1$. On this note, one has to decompose the LB density into its constant average $\rho_0^\star$ and deviation $\rho'^\star$ from the average, such that

$$\rho^\star = \rho_0^\star + \rho'^\star, \tag{3.38}$$

and the LB density can be converted to the physical pressure as

$$p = p_0 + p' = p_0 + p'^\star C_p, \quad p'^\star = {c_s}^2\rho'^\star, \tag{3.39}$$

where

$$C_p = C_\rho C_l^2/C_t^2 = C_\rho C_u^2 \tag{3.40}$$

is the conversion factor for the pressure and p_0 is the physical reference pressure which can be freely specified by the user.

Force. The conversion factor for any force with units $[\mathbf{F}] = \frac{kg\ m}{s^2}$, is

$$C_F = \frac{C_\rho C_l^4}{C_t^2}, \tag{3.41}$$

whereas, for the body force density $[\mathbf{F}_B] = \frac{kg\ m}{s^2}\frac{1}{m^3} = \frac{kg}{(m\ s)^2}$, the factor is

$$C_{F_B} = \frac{C_F}{C_l^3} = \frac{C_\rho C_l}{C_t^2}. \tag{3.42}$$

As a special case, let us consider gravity, which is an acceleration, not a force, with units

$$[g] = m/s^2$$

Quantity	Non-dimentionalisation	Grid parameter	Physical Value
ρ	$\rho = C_\rho \rho^\star$	$\rho^\star = 1$	$C_\rho = \rho$
Δx	$\Delta x = C_l \Delta x^\star$	$\Delta x^\star = 1$	$C_l = \Delta x$
l	$l = C_l l^\star = \Delta x l^\star$	$l^\star = \frac{l}{\Delta x}$	$l^\star = N_x$
Δt	$\Delta t = C_t \Delta t^\star$	$\Delta t^\star = 1$	$C_t = \Delta t$
t	$t = C_t\, t^\star = \Delta t\, t^\star$	$t^\star = \frac{t}{\Delta t}$	$t^\star = N_t$

Table 3.3: Physical parameters and their appropriate conversion factors.

and its conversion factor $C_g = C_l/C_t^2$. The gravitational force density F_g is given by $F_g = \rho g$.

Finally I summarize all the sufficient parameters needed to conduct a simulation with all the correct lattice values in Table 3.3. The steps to obtain all these values are:

1. C_ρ: Set C_ρ in $\frac{kg}{m^3}$ as the density of the fluid whose dynamics we are to simulate.

2. Δx: Set the spatial domain l, in meters and N_x the number of lattice sites (in lattice units) used to discretise the spatial domain so that

$$\Delta x = \frac{l}{N_x}. \tag{3.43}$$

3. Δt: For a given physical viscosity ν, in $\frac{m^2}{s}$, and given a proper $\tau^\star$ (I will comment about this more in detail on the next section), from equation (3.35), one gets:

$$\Delta t = c_s^2 \left(\tau^\star - \frac{1}{2}\right) \frac{\Delta x^2}{\nu}. \tag{3.44}$$

This way, I obtain the needed set of basic conversion factors that will be used to go from simulation values to physical ones.

3.2.2 Accuracy, stability and efficiency

Since the lattice Boltzmann method was introduced in the late 1980s, several kinds of lattice Boltzmann approaches have been developed. However, despite its notable success, methodical investigations on their stability and hydrodynamic behaviors are still demanding [36]. The ongoing section then presents a short analysis about the stability of the code developed along with this work, which uses the knowledge described so far.

In traditional kinetic theory, the equilibrium velocity distribution function is the maximum entropy state, any initial state will evolve towards a state of higher entropy. This result is known as Boltzmann's $\mathcal{H}$-theorem which ensures an increase of entropy, and ensures stability. Therefore, the continuous Boltzmann equation is completely stable in terms of the Boltzmann's $\mathcal{H}$-theorem. If one could guarantee that the equilibrium distribution function for LB methods is the maximum entropy state, then stability can be guaranteed. The problem with this approach is that one cannot usually find an equilibrium distribution function that can simultaneously guarantee an $\mathcal{H}$-theorem and allow the correct form of the equation to be obtained (Navier-Stokes equation)[§]. Since, in the LBM, only a small set of discrete velocities is used and the equilibrium distribution function is usually derived from the Maxwell equilibrium distribution function by the truncated Taylor series expansion, the $\mathcal{H}$-theorem is no longer satisfied. Specifically, the incompressible Navier-Stokes Equations do not have an $\mathcal{H}$-theorem. As a consequence, the LBM is subject to numerical instability [36]. The problem of the existence of instability issues is also obvious considering the lattice Boltzmann equation is a finite difference form of the continuous Boltzmann equation [37] so, like any other numerical scheme, LBM is always accompanied by stability and accuracy issues that have to be treated.

On computational physics it is understood that instability in a LB simulation refers to situations where the errors of our hydrodynamic variables, as population, density or velocity, grow exponentially [28].

As mentioned in the previous section, to simulate physical systems of our interest, there are some important dimensionless quantities that need to be under control, meaning that, one needs to be careful with the choice of certain specific parameters that need to fulfill certain conditions in order for our simulation results to be stable, since this choice is not arbitrary and a wrong selection of this parameters may lead to numerical instability. The restrictions that the values of this parameters need to meet is the subject of this section.

Usually, for problems involving evolution of initial conditions, the analysis of the *Courant Number* $C = |u|\,\Delta t/\Delta x$, is enough to ensure the stability of our results. It compares the speed $\Delta x/\Delta t$ at which information propagates in the model, with the physical speed $|u|$ at which the fluid field is being advected. Therefore, $C \leq 1$ *i.e.* $|u| \leq \Delta x/\Delta t$, is often necessary so the simulation can propagate the physical solution faster than the numerical errors, making the simulation results stable.

Unfortunately, even when this condition is kept, one can encounter unstable results. This is because, for the LBM, stability analysis is much more complicated than the majority of numerical methods such as Finite Differences, Finite Element or Finite Volume, considering that the lattice Boltzmann equation has more degrees of freedom to be treated carefully. One of these important parameters, is the **relaxation time**, τ, and with it, the

[§]Studies have been made on the so called, entropic collision operators, which consist on defining a lattice version of the $\mathcal{H}$-function, i.e, looking for a lattice version of the $\mathcal{H}$-theorem, ensuring that collisions only ever increase the entropy of the system, ruling out many cases of instability [28] (p. 409).

viscosity.

From equation (3.36), it is clear that, for the viscosity to be non-negative, the value of the relaxation time has to be greater than half the time step [34]. Result supported by previous stability studies [38], showing that stability of the LBE based on D2Q9 lattice model deteriorate as $\tau^\star$ approaches to $1/2$ in the $u - \tau^\star$ plane and, as proven in [36], all the LBE approaches are unstable when $\tau^\star \leqslant 1/2$. Thus, stability of **uniform flows** is guaranteed if $\tau^\star > \frac{1}{2}$ [34].

For this method, all the conditions for the parameters that I will state, including the ones that I have already mentioned, are obtained analytically in the bulk far away from any boundaries. This type of analysis does not include the effects of boundaries or machine round-off errors, reason why, the analytically derived stability conditions act as guidelines [28] and are considered necessary conditions.

Another dimensionless number that has to be considered is the velocity which, in this case, is the characteristic Mach number, which should be small in order to simulate incompressible flows. This way, the convergence to the analytic solution of a computational program with a given Reynolds number is performed by increasing $N_x = l/\Delta x$ while either increasing $\tau^\star$ and/or $u^\star$ appropriately, in such a way that a decrease on the value of $u^\star$, should be accompanied by an increase in the number of time steps needed to reach the same flow evolution time [34].

It is also known that, for models valid only in the incompressible regime, velocity should be small for both stability and accuracy [34]. Care then must be always taken to ensure that the Mach number is small enough that the deviation from incompressible behavior is negligible. The smaller the Mach number is, the more accurate the method for simulating the incompressible Navier-Stokes equation will be. This is why, in the previous section, I mentioned that $u^\star \approx 0.2$.

Furthermore, a stability analysis made in [28], specifically for the BGK collision operator, shows that a **sufficient stability condition** is the non-negativity of all equilibrium populations, i.e, $f_k^{eq} \geqslant 0$.

Given all these parameter restrictions, it is clever to enlist some parameter selection strategies. Taking into account also the previous section:

1. C_ρ: Set C_ρ and choose $\rho_0^\star$ arbitrarily, this last parameter does not have any effect on accuracy, stability or efficiency. As stated, it is usually set to unity.

2. Δx: Set the spatial domain, l and N_x.

3. Δt: For a given physical viscosity, ν and a given Reynolds number, choose a proper $\tau^\star$. It is generally recommended to choose relaxation times around unity as well [28].

   (a) If $\tau^\star$ is too small, Δx should decrease or equivalently, $l^\star$ should increase. Making simulations more expensive.

(b) If $\tau^\star$ is too big, $u^\star$ will increase and, as a result, simulations will be less accurate and possibly less stable. Specially values $\tau^\star \gg 1$ should be avoided.

Once the appripiate $\tau^\star$ is chosen, use equation (3.44) to determine Δt.

Notice here that stability and accuracy do not come for free, they usually come at the expense of a more expensive computing process.

Let me now say a few words about how accurate the LBM is as a Navier-Stokes solver, subject that cannot be left aside since there are several error terms that affect the accuracy of a LB simulation. Overall, a discretisation scheme like the one treated herein, is consistent if its truncation errors tend to zero when its discretisation parameters, the numerical time step Δt and the lattice length Δx, approach zero. That is, if the numerical solution tends to the solution in the continuum when the discrete domain tends to the continuous one. The rate at which this happens, establishes the formal order of convergence of the discretisation scheme. In addition, when stability is ensured, this order of convergence dictates the rate at which the numerical solution approaches towards the targeted PDE solution, known as the rate of convergence of the numerical solution. Usually, on discretisation schemes like finite differences, it is possible and relatively easy to evaluate the accuracy of a numerical scheme theoretically, however, LBM is a non-linear scheme due to the use of the equilibrium distribution function in the collision term. This function is quadratic in velocity and the density and velocity are computed as sums over all of the populations at a site [34]. Also, it is affected by other error sources like round-off error, iterative errors, that is difference between numerical solution and the actual steady state, discretisation errors and so on. Consequently, a theoretical measure of accuracy is not enough, rather an estimate of it is needed.

Focusing on the spatial discretisation error, assuming it to be the dominant numerical error, one has

$$\epsilon_\phi \propto \Delta x_i^p \tag{3.45}$$

where ϵ_ϕ is the numerical error related to the desired observable ϕ:

$$\epsilon_\phi(t) := \sqrt{\frac{\sum_x \left(\phi_n(\mathbf{x},t) - \phi_o(\mathbf{x},t)\right)^2}{\sum_x \phi_o(\mathbf{x},t)^2}}, \tag{3.46}$$

with ϕ_n the value of the observable at the current iteration, ϕ_o the exact value of the observable at that time and $\sum_x$ referring to a sum over all the spatial domain.

Autoconvergence. The key point in equation (3.45) is the assumption that ϵ_ϕ follows a power-law relation. Assume the next to be of the form:

$$\epsilon_\phi = E(x)\Delta x_i^\alpha. \tag{3.47}$$

here, Δx_i is the spatial resolution of the domain for the chosen refinement level i, and α is the order of accuracy of the method used to construct ϕ. By analyzing the solution for the observable ϕ_i in three different mesh refinements, say $\Delta x_1 = \Delta x$, $\Delta x_2 = \frac{\Delta x}{\kappa}$ and $\Delta x_3 = \frac{\Delta x_2}{\kappa} = \frac{\Delta x}{\kappa^2}$, with $\kappa > 1$ the autoconvergence order of the solution can be estimated.

Say that ϕ_i is the numerical solution in space at a certain time t, suppose the analytic solution is also known, ϕ_0. Then, one can express ϕ_i as follows, using equation (3.47),

$$\phi_i(\mathbf{x}) = \phi_0(\mathbf{x}) + E(\mathbf{x})\Delta x_i^\alpha + O(\Delta x_i^{\alpha+1}). \tag{3.48}$$

Then combining the solutions with different refinements using (3.48) for $i = 1, 2, 3$

$$\begin{aligned}\frac{\phi_1 - \phi_2}{\phi_2 - \phi_3} &= \frac{E(\vec{x})\Delta x^\alpha(1 - (\frac{1}{r})^\alpha) + O(\Delta x^{\alpha+1})}{E(\vec{x})\Delta x^\alpha((\frac{1}{\kappa})^\alpha - (\frac{1}{\kappa^2})^\alpha) + O(\Delta x^{\alpha+1})} \\ &= \frac{(1 - \frac{1}{\kappa^\alpha})}{\frac{1}{\kappa^\alpha}(1 - \frac{1}{\kappa^\alpha})} + O(\Delta x) \\ &= \kappa^\alpha + O(\Delta x).\end{aligned}$$

determines the difference among solutions using two consecutive resolutions. The relation that must be fulfilled in order for a simulation to converge is

$$\frac{\phi_1 - \phi_2}{\phi_2 - \phi_3} \approx \kappa^\alpha. \tag{3.49}$$

and α is the order of convergence that in theory should coincide with that in equation (3.47).

It has been proven ([28] p. 53, 54) that, the standard LBM, the one treated here, is a second order accurate solver in space and time for the weakly compressible Navier-Stokes equation (weakly compressible refers to errors that become relevant as Mach number approaches unity). Second order in space means that the error decreases quadratically with Δx when fixing the dimensionless ratio $\nu^\star \frac{\Delta t^\star}{\Delta x^{\star 2}}$ and given our choice of $\Delta t^\star$ and $\Delta x^\star$ as the unity, this level of accuracy is obtained when fixing $\nu^\star$.

As an important side note to the conventional dependence of truncation errors on Δx and Δt, truncation errors on LBM also depend on the relaxation time parameter ([28] p. 142).

Finally, stability of LB schemes can also be improved by adopting larger discrete velocity sets, by adding, for example, higher-order Hermite polynomial tensors to the equilibrium distribution [39], leading, ultimately, to larger discrete velocity sets.

i	0	1	2	3	4	5	6	7	8	9	10	11	12	13	14	15	16	17	18
w_k	$\frac{1}{3}$	$\frac{1}{18}$	$\frac{1}{18}$	$\frac{1}{18}$	$\frac{1}{18}$	$\frac{1}{18}$	$\frac{1}{18}$	$\frac{1}{36}$	$\frac{1}{36}$	$\frac{1}{36}$	$\frac{1}{36}$	$\frac{1}{36}$	$\frac{1}{36}$	$\frac{1}{36}$	$\frac{1}{36}$	$\frac{1}{36}$	$\frac{1}{36}$	$\frac{1}{36}$	$\frac{1}{36}$
c_{kx}	0	+1	−1	0	0	0	0	+1	−1	+1	−1	0	0	+1	−1	+1	−1	0	0
c_{ky}	0	0	0	+1	−1	0	0	+1	−1	0	0	+1	−1	−1	+1	0	0	+1	−1
c_{kz}	0	0	0	0	0	+1	−1	0	0	+1	−1	+1	−1	0	0	−1	+1	−1	+1

Table 3.4: D3Q19 Velocity Sets in explicit form. This table is easier to understand following at the same time Fig. 3.3. Here the velocity vectors are $\hat{\mathbf{c}}_k = (\hat{c}_{kx}, \hat{c}_{ky}, \hat{c}_{kz})$ and the weights w_k verify restrictions imposed in equations (3.14).

3.2.3 Extension to 3D

The lattice Boltzmann method with the BGK operator has been discussed only in 2 dimensions up to here, however, the extension to three dimensions is straightforward. One just has to choose a D3Qj lattice and calculate appropriate equilibrium distributions. There are a number of viable three dimensional velocity sets, such as the D3Q15, D3Q19 and D3Q27. In fact, D2Q9 is the two dimensional projection of D3Q19 onto the xy plane. The computational molecule of the D3Q19 velocity set is displayed in Figs. 3.2 and 3.3.

For hydrodynamic simulations, D. d'Humières, P. Lallemand and U. Frisch, proposed in Lattice Gas Models for 3D hydrodynamics [41], a multispeed lattice-gas cellular automata over a cubic lattice with 19 velocities. The explicit velocity sets for this molecule and its respective weights are given in Table 3.4.

The D3Q19 is a *multi-speed* velocity set, with velocities of length 1 and $\sqrt{2}$. The fact that lower dimensional velocity sets are sometimes the projection of higher dimensional ones, means that in cases of the existence of invariance along one or more axes, the simulations can be easily simplified. For this reason, I will not present benchmark cases for 3D as those I will presented for 2D, instead, I will add a body force to the system and present its pertinent test directly in three dimensions.

3.3 Boundary Conditions

When I introduced the concept of Law of Similarity, I also mentioned how important geometry is on a computational fluid dynamics problem and, even though boundary conditions apply to a small portion of the fluid domain, their influence usually will be reflected in the overall behavior of the flow. In fact, the dynamics of fluid flows is highly dependent on the surrounding environment and on how it interacts with the fluid. The way in which this influence can be described mathematically in our code via the respective boundary conditions is described in this section. Boundary conditions play also a crucial role since they transmit the physical constrictions imposed by the external media into the flow.

Specifying boundary conditions to the Navier-Stokes equations is relatively easy, how-

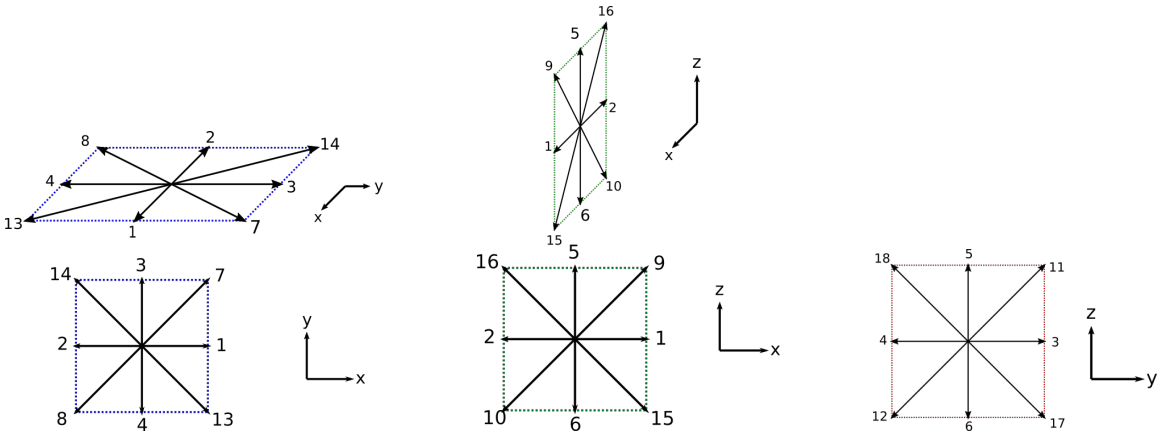

Figure 3.3: Structure of the 3D computational molecule and its velocity vectors illustrated on Table 3.4.

ever not the case for the LB approximation of the problem. Here, the behavior of the discretised distribution function on the lattice nodes needs to be mathematically specified depending on how the fluid interacts with the physical boundary, rather than specifying the macroscopic variables of interest such as the fluid density and velocity, therefore, on this approximation to the problem, there are more degrees of freedom, one for each mesoscopic population f_k. Based on the above, I shall consider the following types of boundary conditions:

1. Periodic
2. No-slip or Bounce back
3. Specification of pressure and velocity using the Zou-He Scheme

For the sake of illustration, I explain conditions for a 3D problem in this chapter and later in Appendix B, the boundary conditions in 2D used in some tests of this work are specified.

In three dimensions, the boundary consists of 6 different plane faces on which the different types of boundary conditions need to be considered. From now on and using definitions in equations (3.16) and (3.17), I will refer to them as follows:

1. Top face: all boundary lattice sites or nodes where $z = z_{max}$ with its associated distribution functions as f_k^{top}.
2. Bottom face: nodes where $z = z_{min}$ with f_k^{bottom}.
3. East face: boundary nodes where $y = y_{max}$ with f_k^{east}.
4. West face: $y = y_{min}$ with f_k^{west}.

5. Frontal face: $x = x_{max}$ with f_k^{front}.
6. Rear face: $x = x_{min}$ with f_k^{back}.

3.3.1 Periodic boundary conditions in 3D

Periodic Boundary conditions are most commonly intended for physical phenomena where surface effects play a negligible role. This type of boundary condition is usually the simplest of the list which is equivalent to changing the topology of the domain to a periodic one. Here the discretised distribution function at one side of the domain is assigned to that at the opposite site of the domain in the streaming process.

East face: The distribution functions pointing towards the inner side of this face are, according to Fig. 3.2):

$$\begin{aligned} f_4^{east} &= f_4^{west} \\ f_8^{east} &= f_8^{west} \\ f_{12}^{east} &= f_{12}^{west} \\ f_{13}^{east} &= f_{13}^{west} \\ f_{18}^{east} &= f_{18}^{west} \end{aligned} \tag{3.50}$$

West face: Again following the D3Q19 molecule illustrated in Fig. 3.2, the appropriate distribution functions to be indicated are:

$$\begin{aligned} f_3^{west} &= f_3^{east} \\ f_7^{west} &= f_7^{east} \\ f_{11}^{west} &= f_{11}^{east} \\ f_{14}^{west} &= f_{14}^{east} \\ f_{17}^{west} &= f_{17}^{east} \end{aligned} \tag{3.51}$$

The logic is the same for the rest of the faces, where the distribution functions to be indicated are:

Frontal face: f_2, f_8, f_{10}, f_{14} and f_{16}.
Rear face: f_1, f_7, f_9, f_{13} and f_{15}.
Bottom face: f_5, f_9, f_{11}, f_{16} and f_{18}.
Top face: $f_6, f_{10}, f_{12}, f_{15}$ and f_{17}.
These boundary conditions are the most used along this work.

3.3.2 Bounce-back Boundary Conditions in 3D

These are used to model solid stationary or moving boundaries. In this case, populations hitting a rigid wall during propagation, are reflected back to where they came from. This

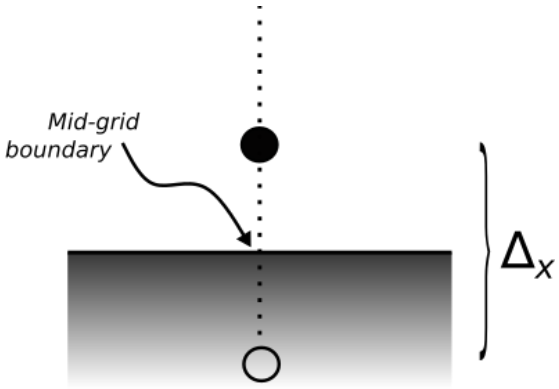

Figure 3.4: Scheme of the non-slip (Bounce-Back) boundary condition for a south wall. The dashed line represents the lattice site, the gray shaded, the solid region and the solid line, the boundary.

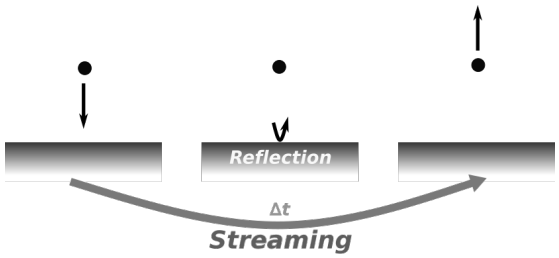

Figure 3.5: The black arrow represents the particle distribution being reflected during the streaming process of a halfway Bounce-Back boundary condition.

scheme implies two facts: first, the wall is impermeable to the fluid, second, as the fluid does not slip on the wall, there is no relative transverse motion between fluid and boundary. These two implications show the reason why the Bounce-Back (BB) method mirrors the Dirichlet Boundary conditions at the macroscopic level [28].

In general, boundary conditions may belong to one of two groups, mid-grid or on-grid. Whereas BB may also be either halfway or fullway. In particular, in this work I use mid-grid halfway Bounce-Back method.

Mid-grid or also called link-wise, means that the boundary lies on the lattice links of the computational domain, as shown in Fig. 3.4, not on the lattice site. Halfway, that particles are considered to travel only half of the link distance, thereby the reflection of the distribution velocity occurs during the streaming step, see Fig. 3.5.

Based on this two figures, 3.4 and 3.5, it is obvious how, for link-wise methods, the inclusion of the boundary condition represents also the inclusion of half a lattice site $\frac{\Delta_x}{2}$ into the physical domain.

Defining

$$f_k^{\star}(\mathbf{x_B}, t) = f_k(\mathbf{x_B}, t) - \frac{1}{\tau}\left(f_k(\mathbf{x_B}, t) - f_k^{eq}(\mathbf{x_B}, t)\right) \tag{3.52}$$

with $\mathbf{x_B}$ the boundary node, for example nodes in the top boundary are $\mathbf{x_B} = (x, y, z_{max})$ and the notation for the distribution function defined in equation (3.52) for these top boundary nodes will be $f_k^{\star top}(t)$, then the specific implementation for each possible segment of the boundary of this non-slip boundary is:

Top face:

$$\begin{aligned}
f_6^{top}(t + \Delta t) &= f_5^{\star top}(t) \\
f_{10}^{top}(t + \Delta t) &= f_9^{\star top}(t) \\
f_{12}^{top}(t + \Delta t) &= f_{11}^{\star top}(t) \\
f_{15}^{top}(t + \Delta t) &= f_{16}^{\star top}(t) \\
f_{17}^{top}(t + \Delta t) &= f_{18}^{\star top}(t)
\end{aligned} \tag{3.53}$$

Bottom face:

$$\begin{aligned}
f_5^{bottom}(t + \Delta t) &= f_6^{\star bottom}(t) \\
f_9^{bottom}(t + \Delta t) &= f_{10}^{\star bottom}(t) \\
f_{11}^{bottom}(t + \Delta t) &= f_{12}^{\star bottom}(t) \\
f_{16}^{bottom}(t + \Delta t) &= f_{15}^{\star bottom}(t) \\
f_{18}^{bottom}(t + \Delta t) &= f_{17}^{\star bottom}(t)
\end{aligned} \tag{3.54}$$

Frontal face:

$$\begin{aligned}
f_2^{front}(t + \Delta t) &= f_1^{\star front}(t) \\
f_8^{front}(t + \Delta t) &= f_7^{\star front}(t) \\
f_{10}^{front}(t + \Delta t) &= f_9^{\star front}(t) \\
f_{14}^{front}(t + \Delta t) &= f_{13}^{\star front}(t) \\
f_{16}^{front}(t + \Delta t) &= f_{15}^{\star front}(t)
\end{aligned} \tag{3.55}$$

Rear face:

$$\begin{aligned} f_1^{back}(t+\Delta t) &= f_2^{\star\,back}(t) \\ f_7^{back}(t+\Delta t) &= f_8^{\star\,back}(t) \\ f_9^{back}(t+\Delta t) &= f_{10}^{\star\,back}(t) \\ f_{13}^{back}(t+\Delta t) &= f_{14}^{\star\,back}(t) \\ f_{15}^{back}(t+\Delta t) &= f_{16}^{\star\,back}(t) \end{aligned} \tag{3.56}$$

East face:

$$\begin{aligned} f_4^{east}(t+\Delta t) &= f_3^{\star\,east}(t) \\ f_8^{east}(t+\Delta t) &= f_7^{\star\,east}(t) \\ f_{12}^{east}(t+\Delta t) &= f_{11}^{\star\,east}(t) \\ f_{13}^{east}(t+\Delta t) &= f_{14}^{\star\,east}(t) \\ f_{18}^{east}(t+\Delta t) &= f_{17}^{\star\,east}(t) \end{aligned} \tag{3.57}$$

West face:

$$\begin{aligned} f_3^{west}(t+\Delta t) &= f_4^{\star\,west}(t) \\ f_7^{west}(t+\Delta t) &= f_8^{\star\,west}(t) \\ f_{11}^{west}(t+\Delta t) &= f_{12}^{\star\,west}(t) \\ f_{14}^{west}(t+\Delta t) &= f_{13}^{\star\,west}(t) \\ f_{17}^{west}(t+\Delta t) &= f_{18}^{\star\,west}(t) \end{aligned} \tag{3.58}$$

These boundary conditions will be mainly used in the study of capillary waves, where their influence over the temporal evolution of the wave will be analyzed.

3.3.3 Specification of Pressure and Velocity Boundary Conditions using the Zou-He Scheme in 3D

These are conditions based on the idea of bounce-back of the non-equilibrium distribution function following the approach by Zou and He [40]. Here I will derive explicitly the corresponding relations for the top face ($z = z_{max}$) and only give the results for the rest of the faces. The same process to derive the conditions applies for the relations in 2 dimensions.

To obtain the necessary conditions, I use

$$\rho(\mathbf{x},t) = \sum_{k=0}^{18} f_k(\mathbf{x},t), \tag{3.59}$$

$$\mathbf{u}(\mathbf{x},t) = \frac{1}{\rho(\mathbf{x},t)} \sum_{k=0}^{18} f_k(\mathbf{x},t)\hat{\mathbf{c}}_\mathbf{k}. \tag{3.60}$$

Top face: As can be seen from the molecule in Fig. 3.2, the distribution functions pointing inwards, that is, the unknowns are:

$$f_6,\ \ f_{10},\ \ f_{12},\ \ f_{15}\ \ and\ \ f_{17}. \tag{3.61}$$

Then, solving for these functions from the velocity in the z-direction in (3.60),

$$f_6 + f_{10} + f_{12} + f_{15} + f_{17} = f_5 + f_9 + f_{11} + f_{16} + f_{18} - \rho v_z \tag{3.62}$$

and from the density (3.59),

$$f_6 + f_{10} + f_{12} + f_{15} + f_{17} = \rho - (f_0 + f_1 + f_2 + f_3 + f_4 + f_5 + f_7 + f_8 + f_9 + f_{11} + f_{13} + f_{18}). \tag{3.63}$$

This way, one obtains a relation for the density in terms of all the known distribution functions:

$$\begin{aligned}\rho =& [2(f_5 + f_9 + f_{11} + f_{16} + f_{18}) \\ &+ f_0 + f_1 + f_2 + f_3 + f_4 + f_7 + f_8 + f_{13} + f_{14}]\frac{1}{1+u_z}\end{aligned} \tag{3.64}$$

However, the unknown distribution functions remain undetermined. To close the system, I assume, as suggested by Zou and He, the Bounceback rule is still correct for the non-equilibrium part of the particle distribution function normal to the surface:

$$f_k^* = f_k - f_k^{(eq)}, \tag{3.65}$$

That is, in the case of the top boundary:

$$f_6^* = f_6 - f_6^{(eq)} = f_5 - f_5^{(eq)} = f_5^*, \tag{3.66}$$

so that

$$f_6 = f_5 + (f_6^{(eq)} - f_5^{(eq)}). \tag{3.67}$$

Considering the relations for $f_6^{(eq)}$ and $f_5^{(eq)}$, leads to the condition that defines f_6:

$$f_6 = f_5 - \frac{\rho}{3}u_z. \tag{3.68}$$

Applying the same rule for the rest of the unknown distribution functions, one obtains the following four expressions:

$$\begin{aligned} f_{10} &= f_9 - \frac{\rho}{6}(u_x + u_z), \\ f_{12} &= f_{11} - \frac{\rho}{6}(u_y + u_z), \\ f_{15} &= f_{16} + \frac{\rho}{6}(u_x - u_z), \\ f_{17} &= f_{18} + \frac{\rho}{6}(u_y - u_z). \end{aligned} \tag{3.69}$$

When this kind of boundary condition is used to simulate a laminar flow driven by a moving lid in the y-direction, these physical constraints translate into

$$\begin{aligned} f_{10} &= f_9, \\ f_{12} &= f_{11} - \frac{\rho}{6}u_{lid}, \\ f_{15} &= f_{16}, \\ f_{17} &= f_{18} + \frac{\rho}{6}u_{lid}. \end{aligned} \tag{3.70}$$

with $u_y = u_{lid}$ the velocity of the lid.

Below, I give the expressions for the east and west boundaries. These conditions will be mainly used for a flow driven by a gradient pressure, hence a corresponding gradient density, always in the incompressible limit, along the y-direction. So, contrary to the relation obtained in equation (3.64), albeit the inlet (west boundary) outlet (east boundary) densities are specified by the problem, a relation to determine the appropriate velocities is needed.

East face:

$$u_y = \tfrac{1}{\rho}[f_0 + f_1 + f_2 + f_5 + f_6 + f_9 + f_{10} + f_{15} + f_{16} + 2(f_3 + f_7 + f_{11} + f_{14} + f_{17})] - 1 \tag{3.71}$$

with $u_y = u_{outlet}$, and the unknown particle distribution functions are:

$$\begin{aligned} f_4 &= f_3 - \frac{\rho}{3}u_y \\ f_8 &= f_7 - \frac{\rho}{6}(u_x + u_y) \\ f_{12} &= f_{11} - \frac{\rho}{6}(u_y + u_z) \\ f_{13} &= f_{14} + \frac{\rho}{6}(u_x - u_y) \\ f_{18} &= f_{17} + \frac{\rho}{6}(u_z - u_y) \end{aligned} \tag{3.72}$$

West face: Considering here $u_y = u_{inlet}$ as

$$u_y = 1 - \frac{1}{\rho}[f_0 + f_1 + f_2 + f_5 + f_6 + f_9 + f_{10} + f_{15} + f_{16} + 2(f_4 + f_8 + f_{12} + f_{13} + f_{18})] \tag{3.73}$$

and

$$\begin{aligned} f_3 &= f_4 + \frac{\rho}{3}u_y \\ f_7 &= f_8 + \frac{\rho}{6}(u_x + u_y) \\ f_{11} &= f_{12} + \frac{\rho}{6}(u_y + u_z) \\ f_{14} &= f_{13} - \frac{\rho}{6}(u_x - u_y) \\ f_{17} &= f_{18} - \frac{\rho}{6}(u_z - u_y) \end{aligned} \tag{3.74}$$

The rest of the boundaries are not used on this work, but the way to obtain them is analog to what I have done for the top boundary here.

3.4 Forcing scheme

In this work, a proper discussion of the implementation of a body force in the LB algorithm is essential, since a force F_α is a momentum source term on the Navier-Stokes equations,

$$\begin{aligned} \partial_t\rho + \partial_\gamma(\rho u_\gamma) &= 0, \\ \partial_t(\rho u_\alpha) + \partial_\beta(\rho u_\alpha u_\beta) &= -\partial_\alpha p + \partial_\beta\left(\eta[\partial_\beta u_\alpha + \partial_\alpha u_\beta]\right) + F_\alpha. \end{aligned} \tag{3.75}$$

It is also important because in order to prepare the 3D BGK LBM as a Shan-Chen pseu-

dopotential method used in the multiphase problemas below, it is necessary to understand and implement correctly body forces in our simulations. In this section I will show how, with the inclusion of forces and assuming still the BGK collision operator, the original algorithm does not suffer mayor modifications.

There are various schemes to implement force in a lattice Boltzmann model, in this work I only focus on the one proposed by Z. Guo, C. Zheng, and B. Shi in 2002 [42].

Considering first the continuous Boltzmann equation with a forcing term,

$$\frac{\partial f}{\partial t} + \xi_\alpha \frac{\partial f}{\partial x_\alpha} + \frac{F_\alpha}{\rho}\frac{\partial f}{\partial \xi_\alpha} = \Omega(f) \tag{3.76}$$

the goal is to discretise it in velocity space, physical space and time. Using, once again, Hermite polynomials, the force contribution to the system takes the form:

$$\frac{\mathbf{F}}{\rho} \cdot \nabla_\xi f \approx -\frac{\mathbf{F}}{\rho} \cdot w \sum_{n=1}^{N} \frac{(-1)^n}{n!} n\mathbf{a}^{(n-1)} \cdot \mathbf{H}^{(n)},$$

now, by replacing the continuous $\boldsymbol{\xi}$ by the discrete velocity set $\hat{\mathbf{c}}_k$ and renormalising by the lattice weights w_k, the discrete form of the forcing term is

$$F_k(\mathbf{x}, t) = -\frac{\mathrm{w}_k}{w(\boldsymbol{\xi})}\frac{\mathbf{F}}{\rho} \cdot \nabla_\xi f|_{\boldsymbol{\xi} \to \sqrt{3}\hat{\mathbf{c}}_k}, \tag{3.77}$$

so the discrete velocity Boltzmann equation with a forcing term F_k can be written as

$$\partial f_k + c_{k\alpha}\partial_\alpha f_k = \Omega_k + F_k, \quad k = 0, ...q-1, \tag{3.78}$$

with q the number of elements in the velocity set, as before $q = 9$ in 2D and $q = 19$ in 3D. This forcing term represents the body force of the system, which, truncated up to second order in velocity, is:

$$F_k = w_k \left(\frac{c_{k\alpha}}{c_s^2} + \frac{(c_{k\alpha}c_{k\beta} - c_s^2\delta_{\alpha\beta})u_\beta}{c_s^4} \right) F_\alpha, \tag{3.79}$$

using Einstein summation convention over Greek indices. This expression recovers the body force at its first order velocity moment:

$$\sum_{k=0}^{18} F_k c_{k\alpha} = F_\alpha$$

which is a source of momentum, just as expected for the Navier-Stokes equation, but not a mass source as confirmed on its zeroth order moment:

$$\sum_{k=0}^{18} F_k = 0.$$

On the other hand, a second order accurate discretisation of the LBGK including the forcing term is [28]:

$$\underbrace{f_k(\mathbf{x} + \hat{\mathbf{c}}_k \Delta t, t + \Delta t)}_{streaming} = f_k(\mathbf{x}, t) + \underbrace{\frac{\Delta t}{\tau}\left(f_k^{eq}(\mathbf{x}, t) - f_k(\mathbf{x}, t)\right)}_{collision} + \left(1 - \frac{\Delta t}{2\tau}\right) F_k \Delta t. \tag{3.80}$$

By defining the source term as

$$S_k = \left(1 - \frac{\Delta t}{2\tau}\right) F_k, \tag{3.81}$$

the post collision population suffers the following modification:

$$f_k^\star = f_k + (\Omega_k + S_k)\Delta t. \tag{3.82}$$

Finally, the macroscopic moments are modified

$$\begin{aligned} \rho &= \sum_k f_k + \frac{\Delta t}{2} \sum_k F_k, \\ \rho \mathbf{u} &= \sum_k f_k \mathbf{c}_k + \frac{\Delta t}{2} \sum_k F_k \mathbf{c}_k = \sum_k f_k \mathbf{c}_k + \frac{\Delta t}{2} \mathbf{F}. \end{aligned} \tag{3.83}$$

This forcing scheme is used in the rest of this work, because when introducing the two-phase method, which is one of the goals of this work, this forcing scheme will lead to viscosity-independent and thus τ-independent, surface tension [28], still other implementations are also possible [43].

3.5 Benchmark cases

As examples of what has been learned up to here on the three previous sections, I illustrate the Poiseuille and Couette Flows in 2 dimensions.

In these simulations, as typically done in literature, the dimensionless time step and lattice spacing are set equal to unity ($\Delta x^\star = \Delta t^\star = 1$) and numerical contributions to viscosity are accounted for and considered to be part of the physics of the method.

3.5.1 Couette problem

Considering first the steady laminar[¶] flow known as Couette Flow, where an incompressible fluid is sandwiched between two infinite parallel plates, located at $y = 0$, $y = L$, system simulated by using periodic boundary conditions along the x-axis in the domain $x \in [0, L] \times y \in [0, L]$. The bottom plate is held fixed such that $\mathbf{u}(u_x(y = 0), 0) = (0, 0)$, while the top plate moves with velocity $\mathbf{u}(u_x(y = L), 0) = (V_0, 0)$. This way, the Navier-Stokes equation of the system reduces to

$$\underbrace{\rho \frac{D\mathbf{u}}{Dt}}_{\text{steady and incompressible}} = -\nabla p + \eta \nabla^2 \mathbf{u} + \mathbf{F},$$

so that the equation to solve is

$$\nabla^2 \mathbf{u} = 0.$$

Taking the symmetries of the problem, this equation further reduces to

$$\frac{d^2 u_x(y)}{dy^2} = 0$$

and considering the boundary conditions, $u_x(0) = 0$ and $u_x(L) = V_0$, the velocity profile solution of the fluid is

$$u_x(y) = \frac{V_0}{L} y. \tag{3.84}$$

The system in the simulation is initially at rest reaching the steady state of equation (3.84) after 200 hours (in physical units) of evolution. A schematic example of the velocity profile formed by this flow appears in Fig. 3.6.

The goal of this section is to show the resulting velocity field, provided specific initial and boundary conditions, therefore I will use this space as an example of adimensionalisation: given the physical parameters, I will obtain the corresponding conversion factors. The flow is simulated for the physical parameters:

[¶]A laminar flow occurs when a fluid flows in parallel layers, with no disruption between the layers, i.e. it is not turbulent.

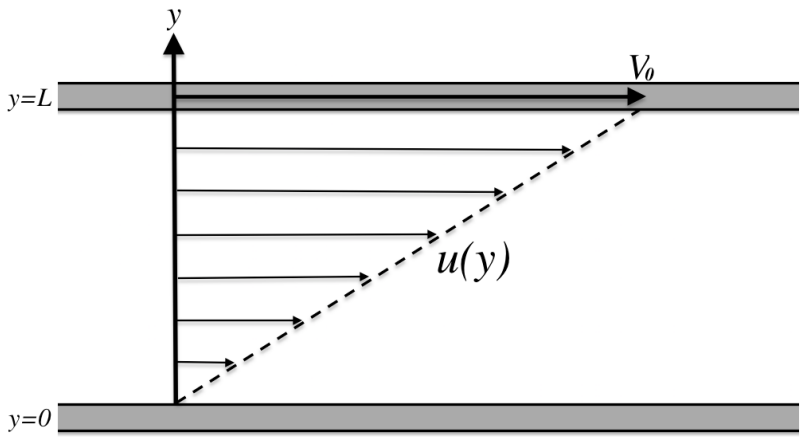

Figure 3.6: Schematic velocity profile of Couette Flow.

$$\begin{aligned} Re &= 125 \\ \nu &= 10^{-6} m^2/s \\ L &= 1m \\ \rho &= 10^3 kg/m^3 \\ V_0 &= 1.25 \times 10^{-4} m/s. \end{aligned} \tag{3.85}$$

Following subsection 3.2.1 and considering $N_x = 100$ and $\tau^\star = 0.9$, the following parameters are obtained:

$$\Delta x = \frac{1\ m}{100} = 1 \times 10^{-2} m, \tag{3.86}$$

$$\Delta t = 13.333 s, \tag{3.87}$$

$$\nu^\star = 0.133 \tag{3.88}$$

as stated in equation (3.36). On the other hand, using (3.32), the non-dimensional velocity of the lid is

$$V_0^\star = 0.166, \tag{3.89}$$

which is needed to use specification of velocity boundary conditions, shown in equations

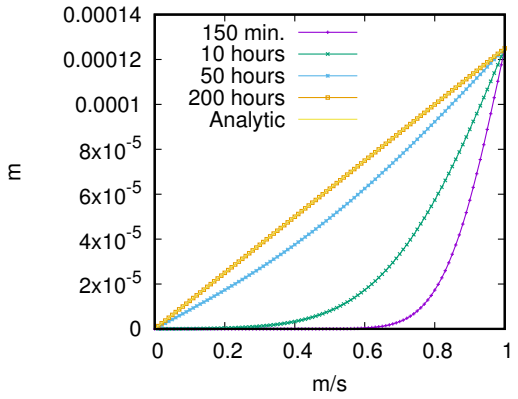

Figure 3.7: Snapshots of $u_x(y)$ at $x = L/2$ for Couette Flow. Starting the simulation with the fluid flow at rest, the velocity profile approaches that of equation (3.84) after 200 hours of evolution in physical time.

(B.9).

The evolution of the velocity profile of this flow, simulated using the lattice Boltzmann method described so far and with the code developed with this work, using the aforementioned characteristics, is illustrated in Fig. 3.7 for different times until the steady state is reached.

For this simulation, periodic boundary conditions were used on the east and west boundaries, equations (B.2) and (B.1) in $x = L$ and $x = 0$ respectively, bounce back at the bottom, equations (B.4) at $y = 0$ and moving lid at the top boundary, equations (B.9) at $y = L$.

In order to illustrate the convergence of the method, the same flow is simulated but with other 3 finer meshes, i.e, $N_x = 200$, $N_x = 400$ and $N_x = 800$. This, as previously mentioned, setting the non-dimensional ratio $\nu^\star \frac{\Delta t^\star}{\Delta x^{\star 2}}$ to a constant value.

Fig. 3.8a shows how the difference between simulations for different resolutions is actually extremely small, plot that represents the velocity profile of each mesh at the steady state ($250 hours$) zoomed in.

At this respect, it is important to mention that the simulation for each resolution of the mesh, approaches a stationary regime at different times imposed numerically by

$$\epsilon_{u_i}(t) := \sqrt{\frac{\sum_{\mathbf{x}} \left(u_{in}(\mathbf{x}, t) - u_{io}(\mathbf{x}, t)\right)^2}{\sum_{\mathbf{x}} u_{io}(\mathbf{x}, t)^2}} \approx 10^{-7} \tag{3.90}$$

with $i = x, y$ (and z in case of 3 dimensions).

Fig. 3.9 shows the value of equation (3.46), as a function of time for 4 different resolutions. All the four simulations were carried out up to $t = 250$ *hours* but the same figure indicates the point at which each simulation reached the steady state, condition (3.90). Given the resulting velocity profile for each simulation at $t = 250$ *hours*, I carried out a

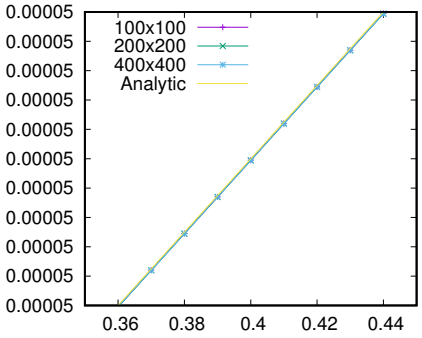

(a) Steady flow for different meshes at $t = 250hours$ zoomed in to a smaller region of the y domain.

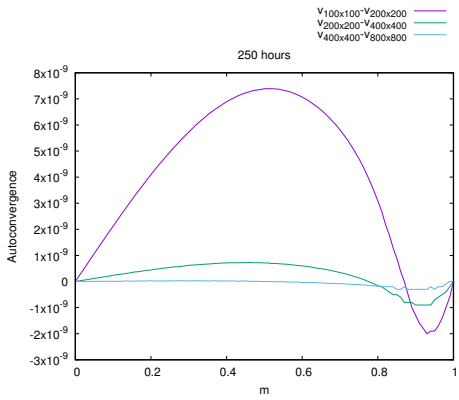

(b) Autoconvergence for Couette Flow at time $t = 250hours$.

Figure 3.8: Comparison of Couette Flow for different refinements of the spatial domain.

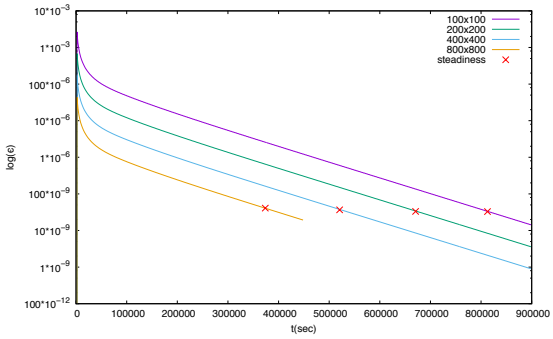

Figure 3.9: Using a logarithmic scale, errors defined on equation (3.46) for the 4 different meshes used and the time at which each simulations reaches the steady state, defined by the threshold in equation (3.90).

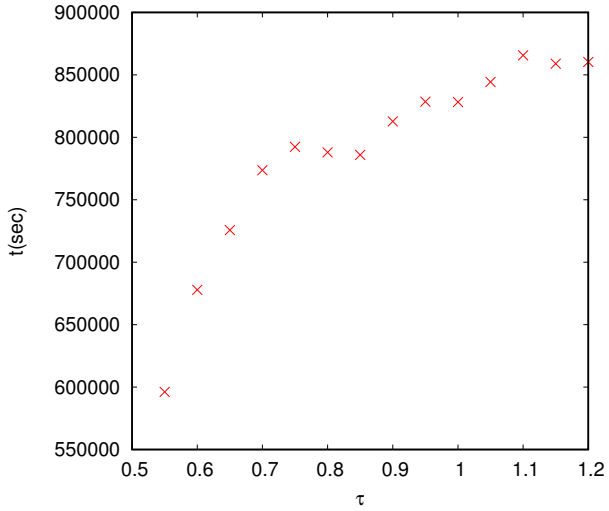

Figure 3.10: Time-steps (vertical axis) at which the steady state (equation (3.90)) for Couette Flow is reached for the same physical system but simulated with different relaxation times.

study of convergence. Fig. 3.8b lets us appreciate how the finer the mesh, the smaller the difference between the resulting velocity profile for each different simulation, as expected.

Another important parameter of the LB Method is the relaxation time, Fig. 3.10 illustrates the dependence on τ of the time at which the steady state is reached. Here, different values of the relaxation parameter were used, maintaining Re constant and $N_x = 100$, so the physical system that the numerical set up represents is the same in all cases.

3.5.2 Poiseuille

For a second example, let us consider the Poiseuille Flow, a steady, laminar, incompressible fluid flow, confined between to infinite parallel plates separated a distance L along the y-axis. The fluid is moving in the x-direction, in this case, due to a constant pressure gradient in the x-direction, as illustrated on Fig. 3.11. This system has a closed stationary solution that can be constructed from the stationary Navier-Stokes equation,

$$\underbrace{\rho \frac{D\mathbf{u}}{Dt}}^{0} = -\nabla p + \eta \nabla^2 \mathbf{u} + \mathbf{F}^{0}.$$

steady and incompressible

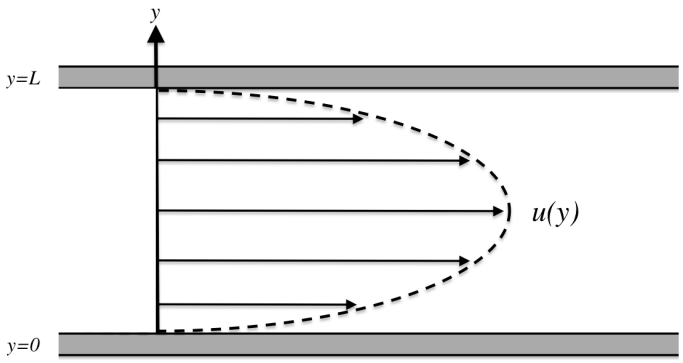

Figure 3.11: Schematic velocity profile of Poiseuille Flow.

Assuming the flow only along the x-direction, the system to solve is

$$\begin{pmatrix} \frac{\partial p}{\partial x} \\ 0 \end{pmatrix} = \eta \begin{pmatrix} \left(\frac{\partial^2}{\partial x^2} + \frac{\partial^2}{\partial y^2} \right) u_x(y) \, . \\ 0 \end{pmatrix}$$

and considering no-slip boundary condition between the fluid and the parallel plates,

$$u_x(y = 0) = 0, \quad u_x(y = L) = 0$$

the resulting velocity profile is

$$u_x(y) = \frac{1}{2\eta} \frac{dp}{dx} y(y - L). \tag{3.91}$$

The simulation was carried out starting with the fluid at rest and using specification of pressure boundary conditions, equations (B.7) and (B.8) for east and west boundaries and bounce back, equations (B.3) and (B.4) for the top and bottom walls, and using the following physical parameters:

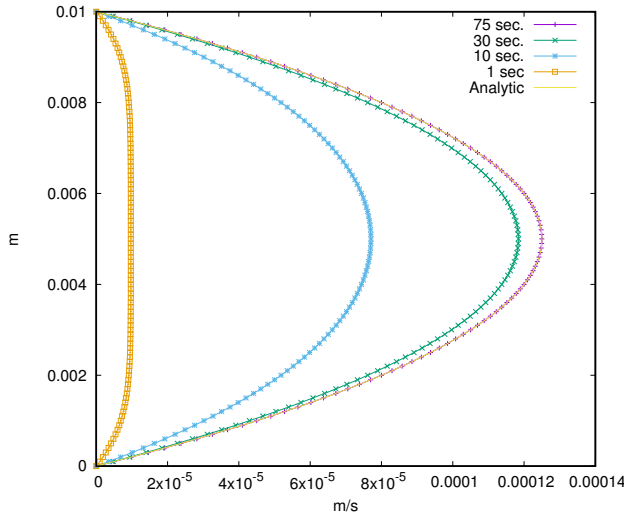

Figure 3.12: Poiseuille Flow. Velocity profile $u_x(y)$ along the y-axis (vertical axis of the plot) at various times calculated on a 100×100 mesh using $\tau = 0.9$.

$$\begin{aligned} Re &= 1.25 \\ \nu &= 10^{-6} m^2/s \\ L &= 0.01m \\ \rho &= 10^3 kg/m^3 \\ \nabla p = 0.1 \quad & \underbrace{kg\frac{m}{s^2}} \quad \frac{1}{m^2}\frac{1}{m} \\ & \text{Units of force} \end{aligned} \tag{3.92}$$

Care must be taken in the code in respect of the value and units of the pressure gradient, since this simulation is in two dimensions, defining a pressure over a boundary side with units of length instead a face with units of area is not that straightforward. One must add a scaling factor representing the extra missing dimension.

The resulting velocity profile is shown on Fig. 3.12 at different times until the steady state is reached at $t = 100sec$. I carried out this simulation with $N_x = N_y = 100$ and $\tau = 0.9$.

For the analysis of the autoconvergence, I ran three other simulations now with $N_x = 200$, $N_x = 400$ and $N_x = 800$ making sure again that the dimensionless ratio $\nu^\star \frac{\Delta t^\star}{\Delta x^{\star 2}}$ was always constant and, with it, the corresponding Reynolds number.

The plot for the second order autoconvergence can be appreciated on Fig. 3.13 where the colored lines represent the factors in (3.49) for $\phi = u_x$

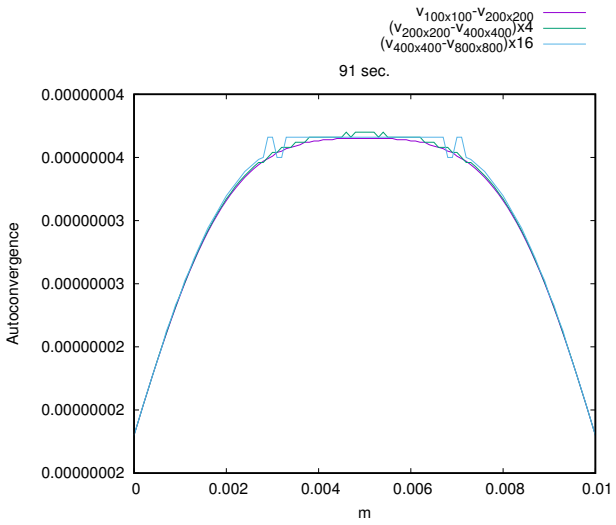

Figure 3.13: Autoconvergence analysis for the numerical simulations of the Poiseuille Flow.

$$u_{x100\times100} - u_{x200\times200},$$
$$(u_{x200\times200} - u_{x400\times400})4,$$
$$(u_{x400\times400} - u_{x800\times800})16.$$

Here, factors 4 and 16 are the corresponding κ^{α} from equation (3.49) with $\alpha = 2$ the autoconvergence order and $\kappa = 2$.

Once again, in the same manner as in Couette Flow, the effects of the relaxation parameter and of the lattice resolution on the time at which the steady state is reached, are shown in Figs. 3.14a and 3.14b.

3.5.3 Lid Driven Cavity

Another problem used as a benchmark test for CFD codes, is the Lid driven cavity. A square cavity filled with fluid and whose lid is set to motion. Here I present a $0.1m$ cavity with a lid moving with velocity $1.55 \times 10^{-2} m/s$ along the x direction, with a Reynolds number of $Re = 1550$. The resulting velocity field is shown in Fig. 3.15 and quite well compares with benchmark solutions, for instance with results of section 5.5 from [44].

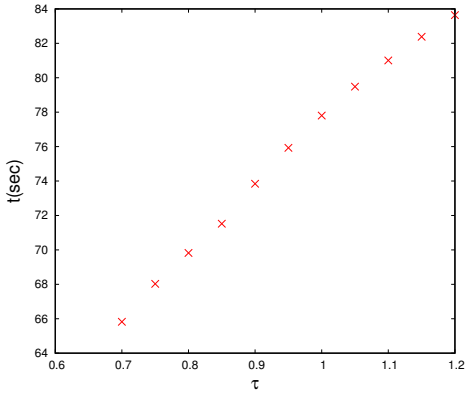

(a) Dependence of the time at which the steady flow is reached, on the relaxation time parameter. The units along the verical axis are time-steps (Δt).

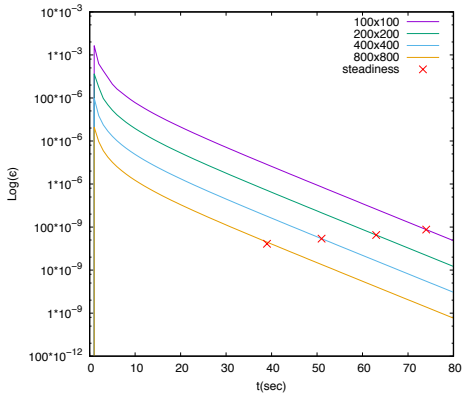

(b) Using logarithmic scale, errors defined on equation (3.46) for the 4 different resolutions used and the time at which each simulation reaches steadiness marked with a ×.

Figure 3.14: Dependence of time for approaching the stationary regime on the values of τ and N_x. Notice that when τ, the relaxation time is bigger, it takes more time to the simulation to reach the stationary regime.

3.5.4 Benchmark cases for the forcing scheme

Using the Guo's scheme introduced before, with second order integration for the forcing term, I successfully simulated in 3 dimensions and using the code developed in this work, the benchmark flow consisting of a constant force

$$\mathbf{F}(\mathbf{x}, t) = \mathbf{F_0}, \tag{3.93}$$

whose velocity profile results in

$$\mathbf{u}(t) = \frac{\mathbf{F_0}}{\rho} t. \tag{3.94}$$

Using periodic boundary conditions in all the boundary faces, the simulation starts with a fluid flow at rest as an initial condition and a randomly directed force defined as $\mathbf{F_0} = (0.0035, 0.007, 0.0061)$. The resulting velocities corresponding to equation (3.94) are shown in Fig. 3.16. The red dots of the plot indicate the analytic values of equation (3.94) for each spatial component of the velocity at the final time of the simulation, which corresponds to $t = 80$ using non-dimensionalised units. These quantities coincide with the numerical result from the simulation, verifying then the correct implementation of the forcing term in the code.

I also validated the code by simulating the unsteady Taylor-Green vortex flow, which is a solution of the incompressible Navier-Stokes equations. In this system, as in the majority of the literature that solves this problem in 2D, that is $\mathbf{F} = (F_x, F_y, 0)$, the force field applied

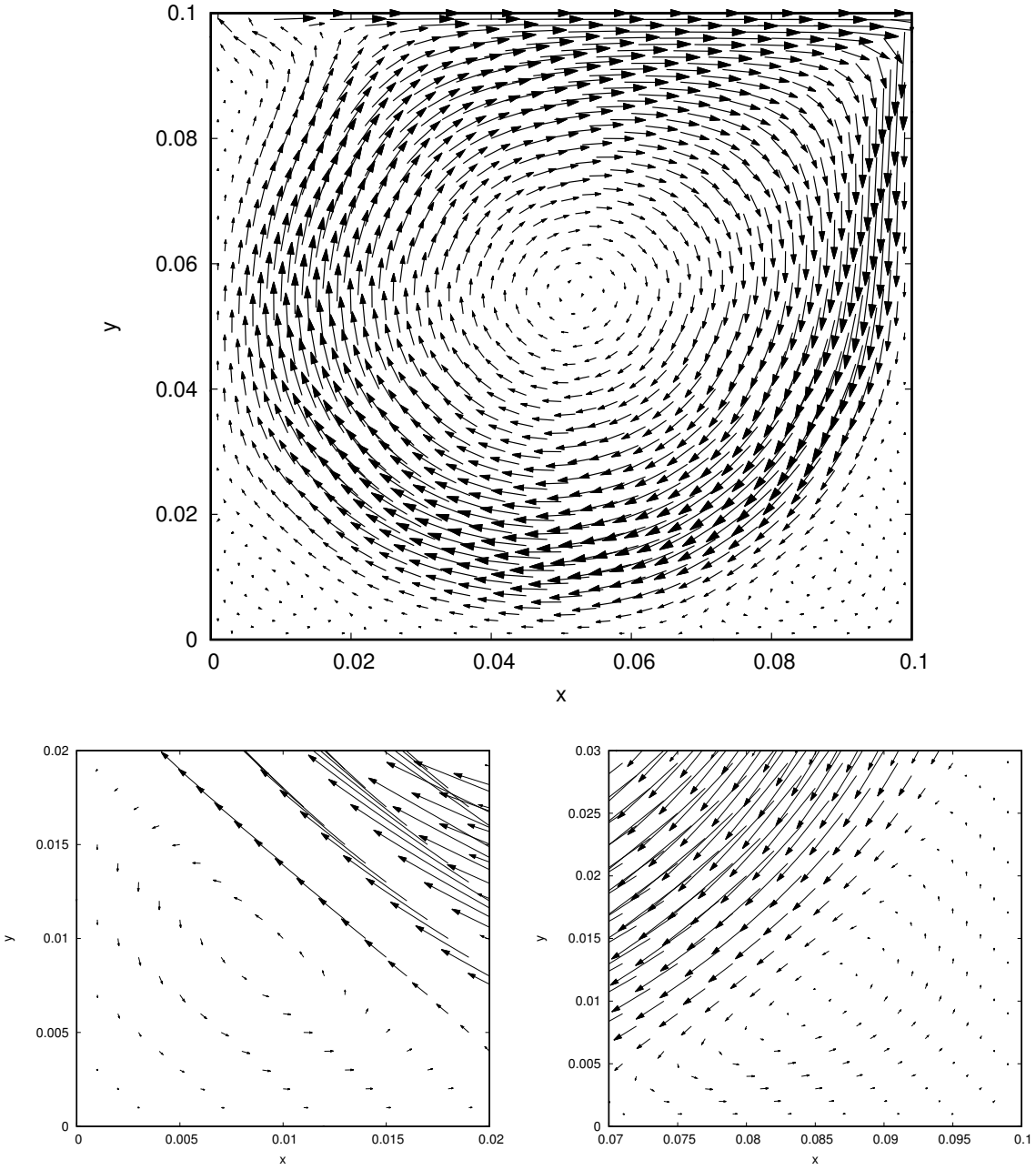

Figure 3.15: Velocity vector field for a lid driven cavity with $Re = 1550$. These plots should be compared with results of section 5.5 from [44]. In the bottom I show the field zoomed near the lower corners of the domain in order to verify that vortexes are also formed there as expected.

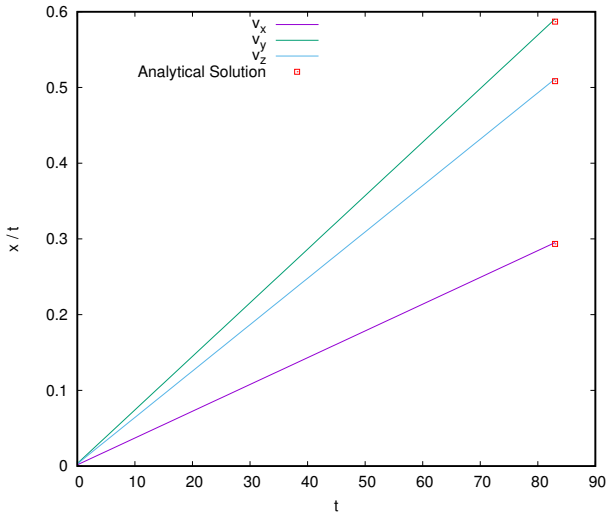

Figure 3.16: Magnitude of the flow velocities generated by a randomly directed constant force. The red dots indicate the analytic value in lattice units of the velocity components in equation (3.93).

is a function of space and time:

$$\mathbf{F} = -\rho\frac{F_0^2}{2}\left(k_x \sin(2k_x x))\hat{\mathbf{e}}_\mathbf{x} + \frac{k_x^2}{k_y}\sin(2k_y y)\hat{\mathbf{e}}_\mathbf{y}\right)e^{-2\nu(k_x^2+k_y^2)t}, \tag{3.95}$$

with $k_{x,y} = \frac{2\pi}{N_{x,y}}$. The analytic solution for the velocity components, given this force field is:

$$\begin{aligned} u_x &= -u_0 \cos(k_x x)\sin(k_y y)e^{-2\nu(k_x^2+k_y^2)t}, \\ u_y &= -u_0\frac{k_x}{k_y}\sin(k_x x)\cos(k_y y)e^{-2\nu(k_x^2+k_y^2)t}. \end{aligned} \tag{3.96}$$

The computational domain in this simulation is $[1, 50] \times [1, 50] \times [1, 50]$ with $u_0 = 0.1$ and $\tau = 1.0$, the velocity and the relaxation parameter. Once again, all boundaries are periodic and the initial condition for the simulation is given by equation (3.96) with $t = 0$.

Fig. 3.17 shows the velocity field of the Taylor-Green vortex flow. It is verified that it maintains the same structure while decaying exponentially as expected from equation (3.96).

Once a breakdown of the lattice Boltzmann method for a single phase fluid has been presented in this chapter, next chapter discusses the theory of the Shan-Chen model, an extension of the LBM capable of simulating two phase fluids.

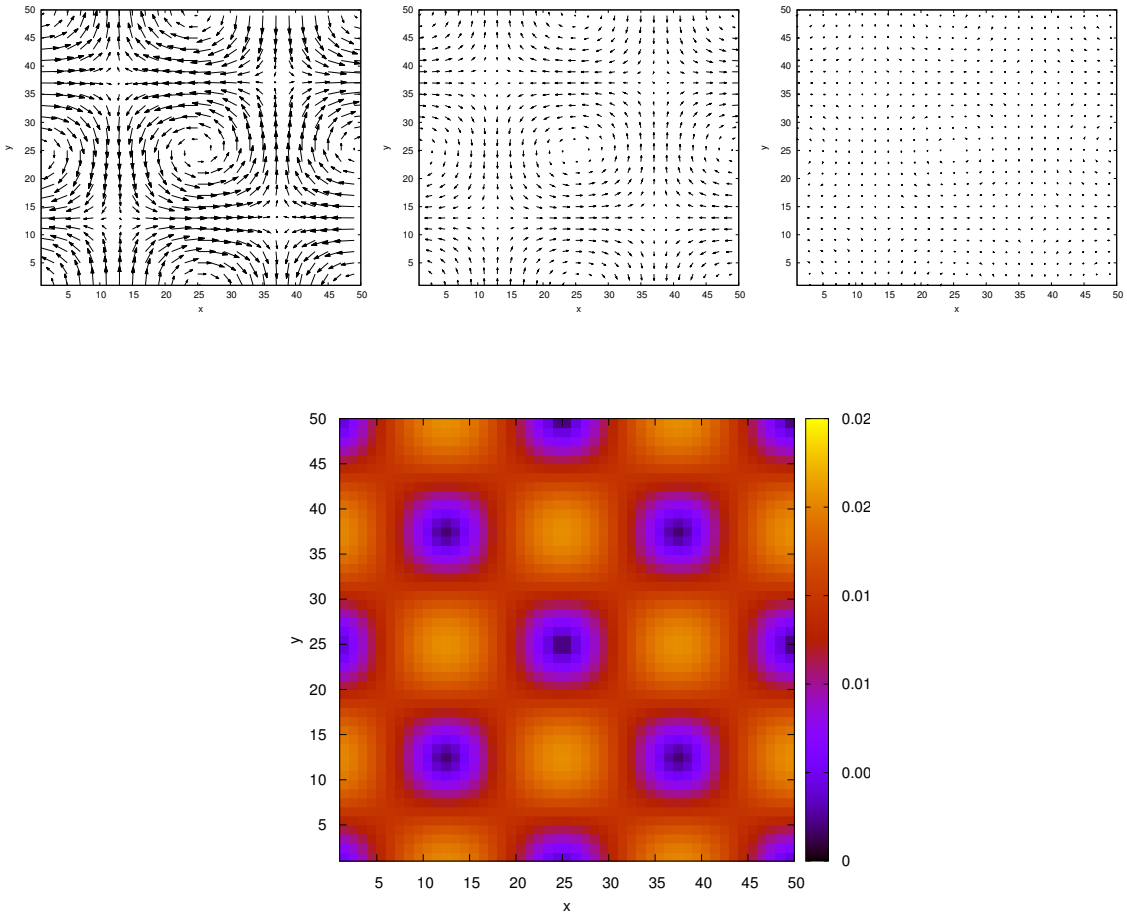

Figure 3.17: Velocity field of the Taylor-Green vortex flow, with $k_x = k_y = \frac{2\pi}{N_{x,y}}$ in $[1, 50] \times [1, 50] \times [1, 50]$. First three plots verify how the velocity field decays exponentially with time without losing its structure as it should be from equation (3.96).

Chapter 4

Shan-Chen Pseudopotential method

A multiphase flow occurs when two or more fluids that differ by their physical properties and that do not easily mix, share an interface. They can be single component fluid flows like liquid-water and water-vapor, that can inter-convert (evaporate or condense), or multicomponet fluid flows such as water and oil were diffusion may happen.

Some important everyday two-phase systems that can be encountered in nature is the dynamics of clouds, in the industries, recovery of bioproducts [45], purification of biomolecules [46], the recovery of petroleum, etc.

Lately, and specially for multiphase flows, LBM has become a novel and powerful tool. There are various LB methods for multiphase/multicomponent systems:

1. Color gradient, 1991.
2. **Shan-Chen**, 1994.
3. Free Energy, 1994.
4. He-Chen-Zhang, 1999.

to mention a few, among which, in this work I use the Shan-Chen approach. As I will mention with more detail later, for Shan-Chen method surface tension is an emergent effect. Effect that is crucial in the study of capillary waves, main goal of this work. Consequently, one of the questions I look to answer is whether this characteristic of the method turns out to be an advantage to the study of these waves.

Therefore, before going to the specifics of the method, it is convenient to introduce an essential property of any two phase fluid flow and a property that will be vital along the rest of this work. The interface between the two phases and the parameter in charge of regulating this interaction between the phases, is the surface tension. ENERGY PER UNIT AREA REQUIRED TO FORM THE INTERFACE BETWEEN THE TWO FLUID PHASES* [26]. Phenomenon

*Definition only valid for simple fluids. In general, the energy per unit area for stretching the interface is given by $\Omega = \sigma + d\sigma/d\epsilon$ with ϵ the strain, but for simple liquids $d\sigma/d\epsilon = 0$ [28].

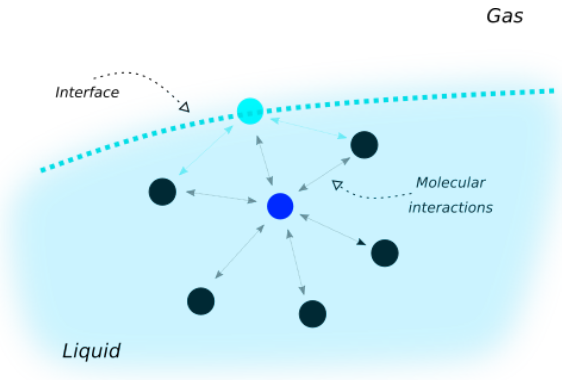

Figure 4.1: Schematic representation of surface tension, showing the excess of energy of a surface particle in comparison to the energy of an internal one.

that is a function of temperature and, at microscopic level, this tension at the interface is due to molecular interactions, see Fig. 4.1.

Surface Tension

The key to the physics of multiphase flows is this notion of surface tension, σ: reversible work per unit area needed to increase the area A of surface Σ by an amount ΔA. Consider a spherical droplet of one fluid suspended in another fluid, e.g. liquid suspended in a gas, then (see Fig. 4.2):

$$\begin{aligned} \Delta W =& \sigma \Delta A \\ =& \Delta P \Delta V \qquad \text{(work done by a gas)} \end{aligned}$$

then $\Delta P(4\pi R^2 \Delta R) = \sigma(8\pi R \Delta R)$ and cancelling out the extra terms, the Laplace relation is obtained:

$$\Delta P = \frac{2\sigma}{R}, \tag{4.1}$$

which relates the curvature of the surface and the surface tension, σ to the pressure jump, *Laplace pressure* ($P_l - P_g = \Delta P$), across the interface. This equation is only valid in 3D, whereas in 2D for a circular droplet this relation is[†]:

$$\Delta P = \frac{\sigma}{R}.$$

[†]Where cylindrical coordinates should be used instead of spherical ones and consider a symmetry along the z-axis. This 2D version is used when studying for example blood flow through arteries or flows in pipes.

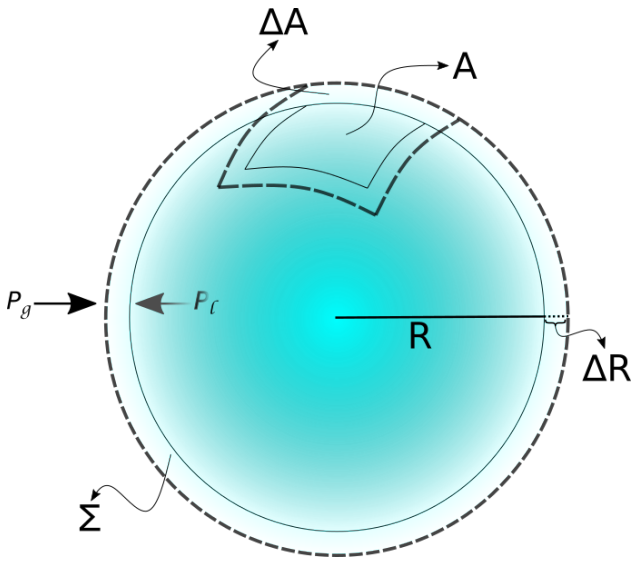

Figure 4.2: Schematic representation of Laplace Relation, where σ is the parameter that relates the curvature of the surface and ΔP.

Liquid-Gas coexistence

Thermodynamics tells us that an ideal gas equation of state (EoS) cannot represent a liquid/vapour coexistence. Hence, one important condition when working with a multi-phase fluid is that, unlike some parameters like viscosity that is a well defined concept for ideal gases, the mere coexistence of two phases on one fluid, commands a non-ideal non-monotonic equation of state capable of describing the phase coexistence. Therefore, given the nature of the system that concerns us, one of the key questions to solve along this chapter and that will be helpful when constructing the Shan-Chen method is: What is the condition for the existence of liquid/vapor equilibrium? Physically, the response to this question represents a constrain to the equation of state.

Let us use van der Waals equation of state for a liquid vapor system to illustrate this argument,

$$P = \frac{KT}{v - b} - \frac{a}{v^2}, \tag{4.2}$$

whose diagram for an isotherm is shown in Fig. 4.3. It is seen that it has a local minimum and a maximum. Any EoS that displays this property, allows the coexistence of two bulk fluids as shown also in Fig. 4.3. These P-V diagrams are useful to find the coexisting densities of the phases (liquid and gas) along with the Maxwell's construction rule. Analytically it can be stated as

$$\int_{v_g}^{v_l} P(v', T)dv' = P_0(v_g - v_l) \tag{4.3}$$

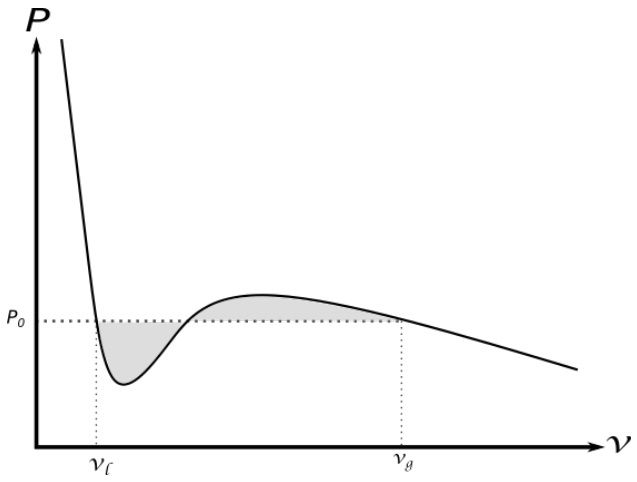

Figure 4.3: Isotherm of the van der Waals equation of state, showing that the phase transition occurs at a pressure P_0, allowing two different bulk fluids.

where P_0 is the constant pressure at which the coexistence happens. Going back to Fig. 4.3, equation (4.3) means that, for a given temperature T, both shaded areas bounded by the curve should be identical [2]. In terms of density, equation (4.3) is [28]:

$$\int_{\rho_g}^{\rho_l} (P_0 - P(\rho', T)) \frac{d\rho'}{\rho'^2} \tag{4.4}$$

where the subscript g stands for the gas and l for the liquid and both densities satisfy $P_0 = P(\rho_g, T) = P(\rho_l, T)$.

Any model for the equation of state that satisfies equation (4.4) is thermodynamically consistent.

Numerical Modeling

In order to model the interactions above described, two approaches can be followed in terms of the interface between the two phases:

- Sharp interface model: Interface is a 2D boundary simulated by a different computational mesh than the used for the rest of the fluid flow, ergo, the need of an explicit tracking of the boundary.

- Diffuse interface approach: approach used by the LB community. Implies a hyperbolic tangent-like transition of the order parameter (density) between one phase and the other as illustrated in Fig. 4.4).

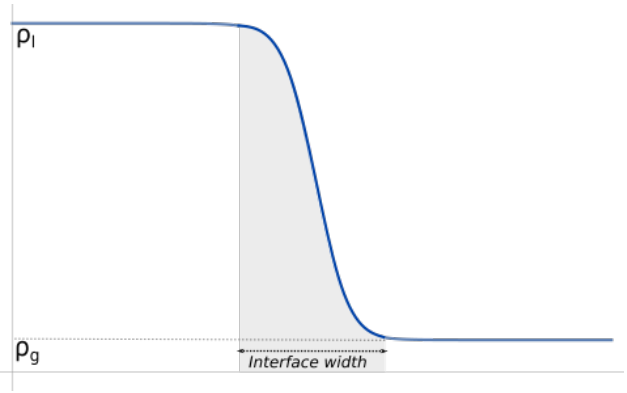

Figure 4.4: Typical density profile in the diffuse interface approach. ρ_g denotes the gas density and ρ_l the liquid density across the spatial domain.

Physically, for substances like water, the interface width is of the order of nanometers but, numerically, it is required to be of several lattice units for the sake of stability of the method. Ideally, as I will show later on, Shan-Chen model works in a regime where the simulation results do not depend on the interface width, that is, within an order of magnitude smaller than the first important length scale of the system.

A key advantage of this diffuse interface models is that it does not need to be tracked explicitly. This and the fact that the density variation is smooth, allows the method to incorporate the description of surface tension into the equations of motion in the pressure tensor. The way this pressure tensor depends on the density categorizes into two approaches:

- Top-down approach: Starting from a macroscopic concept one obtains a force that leads to phase separation. The Free energy method belongs to this kind of approach.
- Bottom-up approach: The postulation of a microscopic interaction, leads to a macroscopic separation of phases by redefining the equilibrium velocity distribution in order to simulate a fluid with a nonideal equation of state. However, this approach leads to inconsistent thermodynamics unless a particular equation of state is chosen.

Shan-Chen model lies in the bottom-up type and is suitable for using a diffuse interface, since in Shan-Chen surface tension is an emergent effect. One important advantage of diffuse interface models is that the interface does not need to be tracked explicitly, making the model convenient for studying problems with nontrivial surface geometries, hence the decision of tackling the analysis of capillary waves with this model.

4.1 Theory of Shan-Chen method

This method was proposed in two articles in 1993 [47] and in 1994 [48] by Xiaowen Shan and Hudong Chen, its fundamental feature is the introduction of an interparticle potential,

which adds an attractive or repulsive tail to the collision term leading to phase separation. The method replaces the ideal gas equation of state by a non-ideal non-monotonic EoS. I will show that these conditions are necessary for the thermodynamic phase transition to occur according to Maxwell's construction rule. This way evaporation, condensation, cavitation and diffusion of a single component fluid can be simulated. In the case of multi-component flows, each component will use its own distribution function.

The basic idea of the model is the incorporation of nonlocal interactions among the particles through an interparticle potential [47] which is, in fact, encoded on a so called SC force. The idea behind such a force is the assumption that intermolecular forces act between pairs of molecules and are additive, also that this interaction is a strong function of the distance between fluid elements:

$$\mathbf{F}^{SC}(\mathbf{x}) = \int (\tilde{\mathbf{x}} - \mathbf{x}) G(\tilde{\mathbf{x}}, \mathbf{x}) \Psi(\mathbf{x}) \Psi(\tilde{\mathbf{x}}) d^3\tilde{\mathbf{x}}$$

with $\tilde{\mathbf{x}} \neq \mathbf{x}$ and $G(\tilde{\mathbf{x}}, \mathbf{x})$ expressing the pairwise interaction between sites $\tilde{\mathbf{x}}$ and $\mathbf{x}$, therefore carrying information about spatial dependence of the force, and $\Psi(\mathbf{x})$ a kind of effective free energy of the system [26].

The inter-particle-like interaction proposed by Shan and Chen is:

$$\mathbf{F}^{\mathbf{SC}}(\mathbf{x}) = -G\Psi(\mathbf{x})\Sigma_k w_k \Psi(\mathbf{x} + \hat{\mathbf{c}}_\mathbf{k}\Delta t)\hat{\mathbf{c}}_\mathbf{k}\Delta t, \tag{4.5}$$

which conserves total momentum, though not locally, given that momentum lost in one phase is gained by the other one[‡]. This form of the force, encoded as the result of pairwise molecular interaction, represents a sum of pseudopotential interaction with only the nearest neighboring fluid cells, taking $G(\tilde{\mathbf{x}}, \mathbf{x})$ as

$$G(\tilde{\mathbf{x}}, \mathbf{x}) = \begin{cases} w_k G & \text{for } \tilde{\mathbf{x}} = \mathbf{x} + \hat{\mathbf{c}}_\mathbf{k}\Delta t \\ 0 & \text{otherwise} \end{cases} \tag{4.6}$$

and the constant G controlling the strength of the interaction. Note that positive G means attraction and negative repulsion.

The big question following the liquid-gas coexistence and the Maxwell's construction rule is, which equation of state corresponds to the Shan-Chen method?

4.1.1 Equation of State of the model

The Equation of State of this method needs additional terms making it non-monotonic so that a phase transition and coexistence of phases is possible. The additional terms are encoded on the SC force.

Taylor-expanding the pseudopotential $\Psi(\mathbf{x} + \hat{\mathbf{c}}_\mathbf{k}\Delta t)$ around $\mathbf{x}$, substitute it on equation

[‡]For a prove of this argument I refer to Shan and Chen 1994 [48].

(4.5) and considering the restrictions imposed to the moments of the weight w_i mentioned in chapter 3, one obtains

$$\begin{aligned}
F_\mu^{SC}(\mathbf{x}) &= -G\Psi(\mathbf{x})\Sigma_k w_k[\Psi(\mathbf{x}) + \partial_\alpha\Psi(\mathbf{x})c_{k\alpha}\Delta t + \frac{1}{2!}\partial_\alpha\partial_\beta\Psi(\mathbf{x})c_{k\alpha}c_{k\beta}\Delta t^2 \\
&+ \frac{1}{3!}\partial_\alpha\partial_\beta\partial_\gamma\Psi(\mathbf{x})c_{k\alpha}c_{k\beta}c_{k\gamma}\Delta t^3 + O(\delta^4)]c_{k\mu}\Delta t \\
&= -G\Psi(\mathbf{x})[\Psi(\mathbf{x})\Sigma_k w_k c_{k\mu}\Delta t + \partial_\alpha\Psi(\mathbf{x})\Sigma_k w_k c_{k\alpha}c_{k\mu}\Delta t^2 + \frac{1}{2!}\partial_\alpha\partial_\beta\Psi(\mathbf{x})\Sigma_k w_k c_{k\alpha}c_{k\beta}c_{k\mu}\Delta t^3 \\
&+ \frac{1}{3!}\partial_\alpha\partial_\beta\partial_\gamma\Psi(\mathbf{x})\Sigma_k w_k c_{k\alpha}c_{k\beta}c_{k\gamma}c_{k\mu}\Delta t^4 + O(\delta^4)] \\
&= -G\Psi(\mathbf{x})\left(c_s^2\Delta t^2\partial_\alpha\Psi(\mathbf{x}) + \frac{1}{6}c_s^4 3\partial_{\alpha\gamma\gamma}\Psi(\mathbf{x})\Delta t^4\right)\delta_{\alpha\mu} \\
&= -\left(Gc_s^2\Delta t^2\Psi(\mathbf{x})\partial_\mu\Psi(\mathbf{x}) + \frac{1}{2}c_s^4\Psi(\mathbf{x})\partial_{\mu\gamma\gamma}\Psi(\mathbf{x})\Delta t^4\right) \\
&= -\left(\frac{1}{2}Gc_s^2\Delta t^2\partial_\mu\Psi^2(\mathbf{x}) + \frac{1}{2}c_s^4\Psi(\mathbf{x})\partial_{\mu\gamma\gamma}\Psi(\mathbf{x})\Delta t^4\right).
\end{aligned} \tag{4.7}$$

For diffuse interface models as this one, the smoothness of the transition of the density across the interface permits the incorporation of the surface tension into the fluid equations of motion in the description of the pressure tensor $\mathbf{P}$. The tensor $P_{\alpha\beta}$ corresponds to force per unit area in the β-direction on a surface pointing along the α-direction. For an isotropic fluid, the pressure tensor is $P_{\alpha\beta} = p_b\delta_{\alpha\beta}$ and so the treatment of the pressure as a scalar. Nonetheless, when an interface is involved, the isotropy is broken. Now the pressure tensor for SC is defined as the excess pressure of the interparticle force with respect to that of the ideal gas:

$$\nabla\cdot\mathbf{P}^{\mathbf{SC}} = \nabla c_s^2\rho - \mathbf{F}^{\mathbf{SC}}, \tag{4.8}$$

this way, if $\Delta t = 1$ in equation (4.7),

$$\begin{aligned}
\partial_\alpha P_{\alpha\mu} =& \partial_\mu\left(c_s^2\rho\right) + \left(\frac{1}{2}Gc_s^2\partial_\mu\Psi^2(\mathbf{x}) + \frac{1}{2}c_s^4\Psi(\mathbf{x})\partial_{\mu\gamma\gamma}\Psi(\mathbf{x})\right) \\
&= \partial_\mu\left(c_s^2\rho + \frac{1}{2}Gc_s^2\Psi^2(\mathbf{x})\right) + \frac{1}{2}c_s^4\Psi(\mathbf{x})\partial_{\mu\gamma\gamma}\Psi(\mathbf{x}) \\
&= \partial_\mu p_b(\rho) + \frac{1}{2}c_s^4\Psi(\mathbf{x})\partial_{\mu\gamma\gamma}\Psi(\mathbf{x}).
\end{aligned} \tag{4.9}$$

Even though the detailed form of the pressure tensor depends on the specific model, inde-

pendently of the model, this pressure tensor must describe an equation of state that allows for phase coexistence and accounts for the surface tension. In diffuse interface models, this surface tension is accounted *via* a force,

$$\mathbf{F} = \kappa\rho\nabla\Delta\rho.$$

Force that leads to

$$\partial_\alpha p_b - F_\alpha = \partial_\beta\left[\left(p_b - \frac{\kappa}{2}(\partial_\gamma\rho)^2 - \kappa\rho\partial_\gamma\partial_\gamma\rho\right)\right)\delta_{\alpha\beta} + \kappa(\partial_\alpha\rho)(\partial_\beta\rho)\Big] := \partial_\beta P_{\alpha\beta}, \tag{4.10}$$

the pressure tensor $P_{\alpha\beta}$ also contains information about the equation of state and the surface tension [28]. Comparing equation (4.9) and (4.10), one finally obtains the equation of state of the multiphase Shan-Chen model:

$$p_b(\rho) = c_s^2\rho + \frac{1}{2}Gc_s^2\Psi^2(\mathbf{x}), \tag{4.11}$$

with

$$\kappa = -G\frac{c_s^4}{2}, \quad \Psi(\mathbf{x}) \propto \rho. \tag{4.12}$$

As a remark, it is obvious that for $G \to 0$ the ideal equation of state is recovered, so G is in charge of controlling the strength of the interaction, generating the conditions necessary for phase transitions, that is why this parameter is referred to as the *temperature like* parameter.

Shan and Chen proposed in their original paper, the following pseudopotential function:

$$\Psi(\mathbf{x}) = \rho_0\left[1 - \exp\left(-\frac{\rho_0}{\rho(\mathbf{x})}\right)\right] \tag{4.13}$$

with ρ_0 usually equal to unity and $\Psi(\mathbf{x})$ bounded between 0 and ρ_0, as seen in Fig. 4.5. This way $\mathbf{F}^{\mathbf{SC}}$ remains finite even for large densities, resulting in stable simulations for density ratios even larger than for the other common form of the pseudopotential,

$$\Psi(\rho) = \rho.$$

Furthermore, by taking Ψ like in equation (4.13), the coexistence curve of the LBM agrees with the thermodynamic theory [48].

Given this form of pseudopotential, equation (4.13), and considering that there is a stationary inflection point in the constant-G line on a $\rho/\rho_0 - p$ diagram,

$$\left(\frac{\partial p(\rho)}{\partial\rho}\right)_G = 0,$$
$$\left(\frac{\partial^2 p(\rho)}{\partial\rho^2}\right)_G = 0,$$

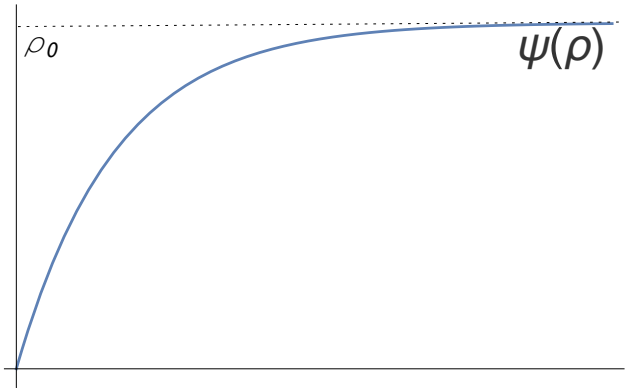

Figure 4.5: Pseudopotential proposed by Shan and Chen, bounded between 0 and ρ_0.

with critical values of

$$\begin{aligned} \frac{\rho_{crit}}{\rho_0} &= \ln 2 \\ G &= \frac{-4}{\rho_0} \end{aligned} \tag{4.14}$$

and with the common choice of $\rho_0 = 1$, phase separation occurs only for $G < -4$ as I will show in the next sections.

As final comments to this section, as every computational method, Shan-Chen model has its own limitations:

- Limited to low density ratios: bigger ones will lead to numerical instability since the forcing scheme will generate bigger velocities than those it can support.
- Surface tension cannot be specified independently of the density ratio.
- Depending on the potential chosen there is a possible lack of thermodynamic consistency.

And some main fields of applications, but not restricted to them:

- Dynamics of bubbles.
- Suspension of solid particles in liquid and/or vapor phases.

4.2 Basic test

All the simulations henceforth presented are carried out using a three dimensional code and presented in lattice units.

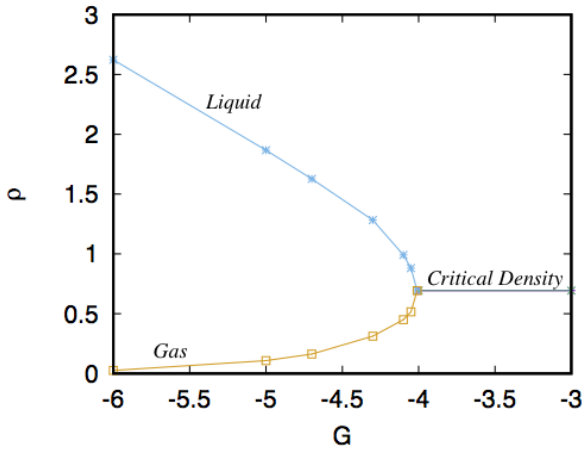

Figure 4.6: Maximum and minimum density values, equivalent to liquid and gas phases respectively as a function of G. The bifurcation of the system represents phase separation from an homogeneous critical density $\rho_{crit} = \ln 2$, into two phases at $G_{crit} = -4$. This result should be compared with Figure 9.9 in [28] and Figure 1 in [47].

4.2.1 Phase transition

The liquid-gas phase transition is shown to occur for a properly chosen interparticle potential, in our case equation (4.13), and a temperature-like parameter below the critical value.

The simulations reported here are constructed on a $50 \times 50 \times 1$ lattice with periodic boundary conditions in all faces of the domain. Initially, the density distribution is homogeneous plus a small random fluctuation ($\rho = \rho_{crit} \pm \delta\rho = \ln 2 \pm 0.001$), with ρ_0 from (4.14) equal to unity. Fig. 4.6 shows the maximum and the minimum densities in the final steady state of this simulations as function of the temperature-like parameter G. The figure shows how, as G goes below the critical value, the system transits from a single phase fluid to a two phase fluid. Whereas Fig. 4.7 displays the time evolution of the density for the case with $G = -6.0$.

Hence, the separation of two phases and with it, the emergent effect of surface tension.

4.2.2 Liquid droplet in a gas phase

The surface tension defined as the mismatch between the normal and transversal components of the pressure tensor, integrated across the interface in its normal direction

$$\sigma = \int_{-\infty}^{\infty} (P_n - P_t) d\hat{n} \tag{4.15}$$

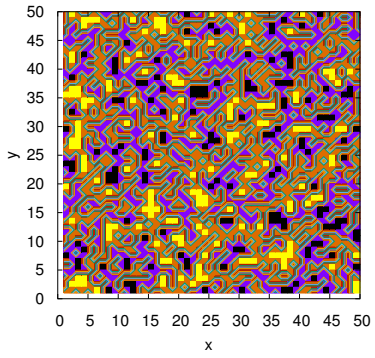

(a) $t = 0$.

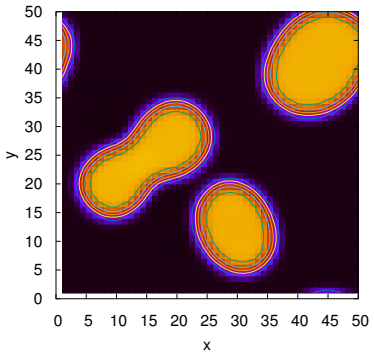

(b) $t = 300$.

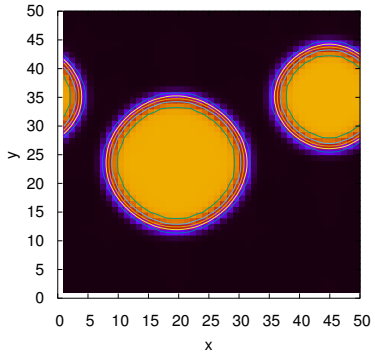

(c) $t = 1500$.

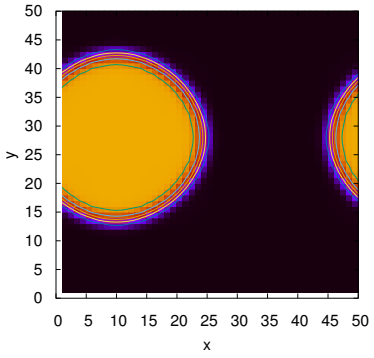

(d) $t = 18000$.

Figure 4.7: Phase transition in a $50 \times 50 \times 1$ lattice. Shown is the time evolution of the density at $t = 0$ with $\rho_{crit} \pm 0.001$, $t = 300$, $t = 1500$ and its final steady state at $t = 18000$. Color black indicates a gas phase and yellow a liquid phase.

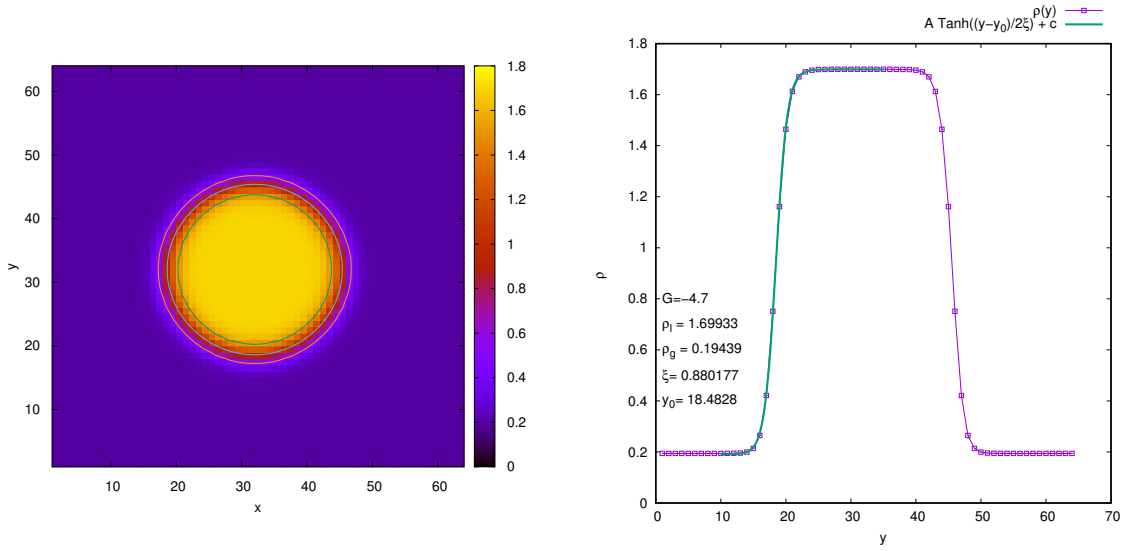

Figure 4.8: Steady state of a liquid droplet in a gas sea with $\rho_l/\rho_g = 8.741732$, $R = 13.9972$, $\Delta p = 2.98 \times 10^{-3}$ and $\sigma = 2.0856 \times 10^{-2}$ and its hyperbolic tangent-like density profile.

is not always straightforward to compute in simulations. However, it is possible to compute surface tension by exploiting the Laplace relation in equation (4.1), using the so called *Laplace test* or bubble test. For a three dimensional bubble at rest of one fluid phase, say liquid, immersed in a sea of the other fluid phase, say gas, Laplace law states:

$$P_l - P_g = \frac{2\sigma}{R},$$

where σ is the surface tension and R the radius of the droplet as illustrated in Fig. 4.2.

For the test I use a $64 \times 64 \times 64$ lattice, initialized a bubble of density $\rho_l = 2.1$ and $R = 15$ in a sea with density $\rho_g = 0.15$ with a sharp interface and $G = -4.7$. When the system reaches equilibrium, a spherical bubble with a diffuse hyperbolic tangent-like interface forms, shown in Fig. 4.8,

$$\rho(x) = \frac{\rho_l - \rho_g}{2} \tanh\left(\frac{x - x_0}{2\xi}\right) + \frac{\rho_l + \rho_g}{2}. \tag{4.16}$$

At its steady state, $\rho_l/\rho_g = 8.741732$, $R = 13.9972$, $\delta p = 2.98 \times 10^{-3}$ and $\sigma = 2.0856 \times 10^{-2}$. The density profile of this droplet is shown in Fig. 4.8 with the best fit parameters of the interface profile of equation (4.16).

A number of tests with different bubble radii were ran for a fixed G to show that δp *vs.* $1/R$ is linear, with 2σ being the slope of the curve, as shown in Fig. 4.9. While maintaining the spherical shape of the droplet, these simulations also prove the isotropy of

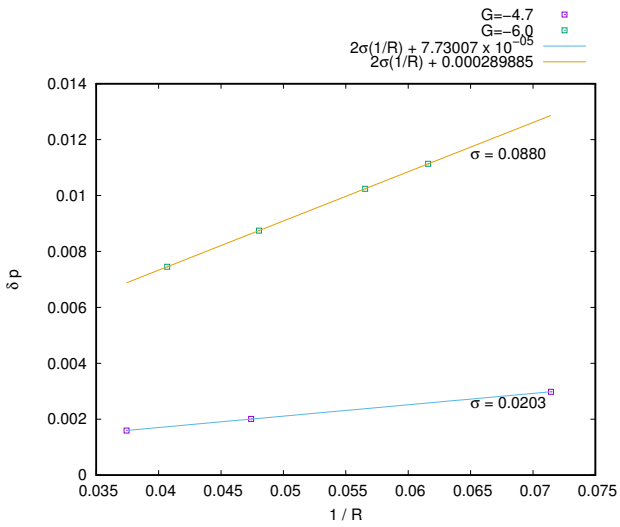

Figure 4.9: Results of the Young-Laplace test for a liquid droplet in a gas phase. The relation is linear, with the slope of the curve being twice the surface tension, 2σ, i.e. the linear fit is $2\sigma\frac{1}{R} + \Delta p_0 = 2(0.0203)\frac{1}{R} + 7.73007 \times 10^{-5}$ for $G = -4.7$, with the small correction of 7.73007×10^{-5} due to numerical errors.

the surface tension.

In these simulations, a zero fluid velocity is expected everywhere. However, numerical simulations often present microcurrents or parasitic currents near the droplet interface due to the truncated nature of the numerical method as the next section presents, i.e. truncation errors arising from the SC Force.

4.2.3 Spurious currents

The presence of spurious currents is an unphysical and undesirable effect, hence if its magnitude is large, the results are inaccurate and can lead to numerical instability. They arise from the numerical approximation of the surface tension force in equation (4.7), specially when this approximation is not perfectly isotropic.

Continuing Taylor expansion to higher orders in equation (4.7), Shan-Chen force in D3Q19 is a combination of dominating isotropic contributions and an isotropic error term (see Appendix C for details)

$$\mathbf{F}^{aniso} \propto G\Psi(\mathbf{x})(\hat{\mathbf{e}}_x\partial_x^5 + \hat{\mathbf{e}}_y\partial_y^5 + \hat{\mathbf{e}}_z\partial_z^5)\Psi(\mathbf{x}), \tag{4.17}$$

that gives rise to spurious currents increasing proportionally with G. This dependence of the magnitude of the spurious currents on the temperature like parameter, is shown in Fig. 4.10 where I represent the velocity field resulting out of this phenomenon, here as $|G|$ increases, the emerging spurious currents increase as well.

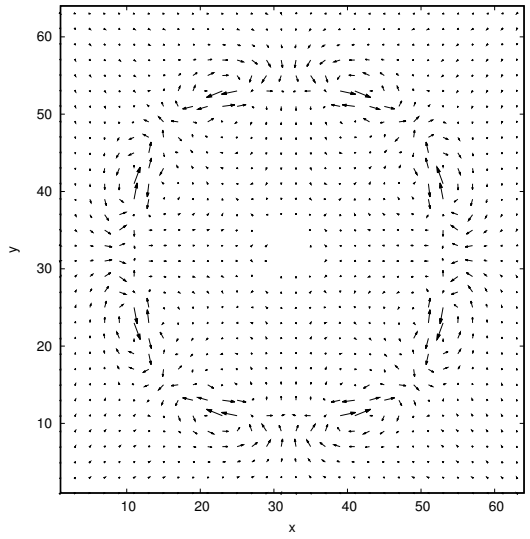

(a) $G = -4.7$, with $\rho_l/\rho_g = 8.91887$, $R = 21.0916$ lu and $\sigma = 0.02119$. The values of the vector field are magnified by a factor of 1000.

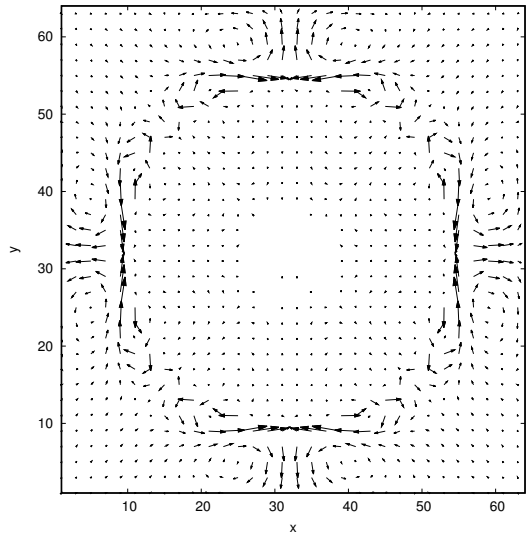

(b) $G = -6.0$, with $\rho_l/\rho_g = 97.1411$, $R = 20.8160$ and $\sigma = 0.09102$. The values of the vector field are magnified by a factor of 50.

Figure 4.10: Velocity field representing spurious currents of the liquid droplet in a gas phase at equilibrium.

4.2.4 Galilean invariance test: Liquid droplet with a constant velocity

Now I simulate a liquid droplet immerse in a gas phase with a constant velocity $v_y = 0.025\Delta y/\Delta t$. As expected, the fact that the droplet maintains its spherical shape through the evolution of the system, once again proves the isotropy of the model, at least at a good order of approximation.

Up to this point, I have discussed all basic theory and benchmark tests necessary to understand and implement a code capable of simulating a two phase fluid in 3 dimensions. Next in this work is the analysis of capillary waves, a characteristic phenomenon of any two phase fluid.

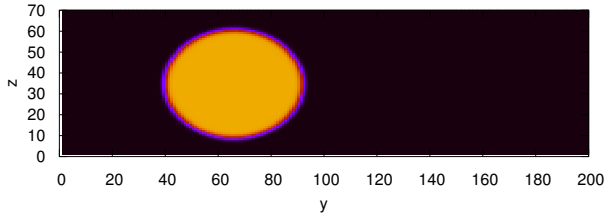

(a) $t = 0$.

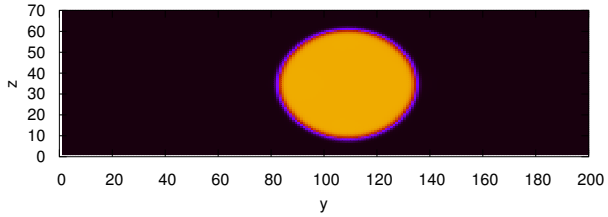

(b) $t = 1,740$.

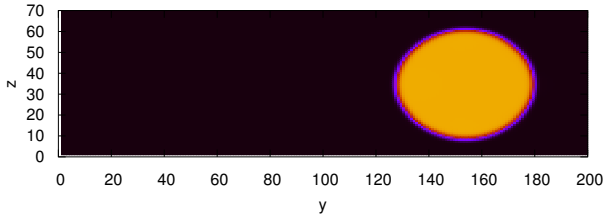

(c) $t = 3,540$.

Figure 4.11: Liquid drop immerse in a gas phase with constant velocity proving, by maintaining its spherical shape, the galilean invariance of the model .

Chapter 5

Simulation of small amplitude capillary waves in confined geometries

5.1 Physical problem

Waves at fluid interfaces in two phase flows are ubiquitous across a wide range of scales. From tidal waves with a wavelength of $\lambda \approx 10^7 m$ and tsunamis with $\lambda > 10^5 m$, to interfacial waves with long wavelengths such as gravity waves where the force of gravity tries to restore equilibrium and those with small wavelengths called capillary waves, whose dominant restoring mechanisms are surface tension and viscosity of the fluid. Fig. 5.1 shows a schematic description of these waves. Its characteristic wavelength is [49]

$$\lambda_c = \sqrt{\frac{\sigma}{\rho g}}.$$

For $\lambda \ll \lambda_c$ one has the case of capillary waves, on the contrary, for $\lambda \gg \lambda_c$, the case of gravity waves and when $\lambda \approx \lambda_c$, gravity-capillary waves. In nature, the wavelength of a capillary wave on water is typically less than a few centimeters, in addition, their amplitude is much smaller than their wavelength $A \ll \lambda$. For these short wavelengths, $\lambda \ll \lambda_c$, gravity forces can be ignored from the analysis [27].

Capillary waves take part in many physical phenomena, natural processes and engineering applications [49]. They play an important role in Rayleigh-Plateau instability [50], the atomization of liquid jets [51], they are observed at the front of short gravity waves [52], etc. They are also a central interest in cell biology [53] [54] [55], influencing properties of lipid membranes, micelles and vesicles, and naturally in microfluidics, specially for applications such as surface wave acoustics [56], microstreaming [57] and ultrasound cavitation [58].

In this chapter and as the main goal of this work, I focus the rest of the analysis on the temporal behaviour of the amplitude of stationary capillary waves and the effect of confined

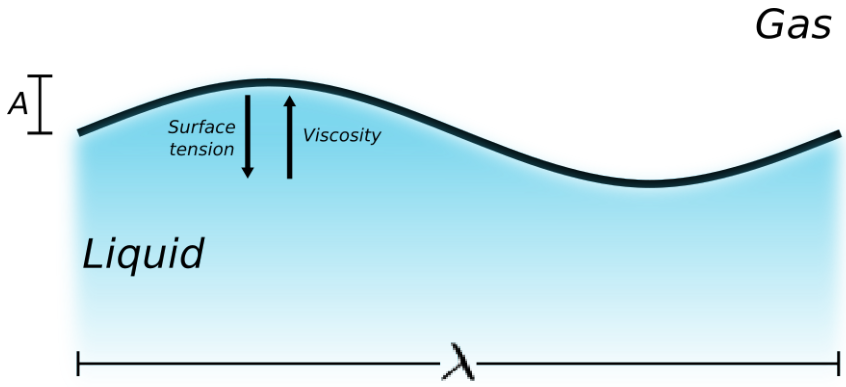

Figure 5.1: Schematic representation of interfacial capillary waves with $A \ll \lambda$. For these waves, the dominant restoring mechanisms are surface tension and viscosity of the fluid.

geometries and different values of surface tension have in it.

5.2 Numerical setup

For this purpose, I exploit some of the advantages of the lattice Boltzmann method and the Shan-Chen implementation, namely, a single numerical parameter τ representing the viscosity η of the fluid, via equation (2.40) as well as the temperature like parameter G, which is directly related to the surface tension of the system σ, as seen in the Young-Laplace test and Fig. 4.9. These two parameters, τ and G represent, in the code and in the method, the two main restoring forces of the dynamics of a stationary capillary wave. Another possible asset of this method for the study of capillary waves that I will analyze in the work, is the fact of the Shan-Chen approach being a bottom-up diffuse interface model, meaning that surface tension is an emergent effect, and that the interface does not need to be tracked explicitly, this makes it suitable for the study of systems with intricate interfacial geometries. Finally, for the simulation of confining geometries, I will also use two different kinds of boundary conditions: Bounce-back boundaries in the top and bottom sides of the domain, representing the effect of walls, and periodic boundary conditions in the rest of the spatial domain, particularly, I will reduce the 3 dimensional domain to a 2 dimensional one by using a slab symmetry along the x-axis such that the computational lattice, hence the volume to analyze, will be defined as $[1, 1] \times [1, \lambda] \times [1, L]$, as illustrated in Fig. 5.2.

For the initial setup of the system, following experimental methods [59], the wave is generated as follows: a fluid interface originally in thermodynamic equilibrium is excited by pressure fluctuations generated locally at the interface, equation (4.11) translates these pressure fluctuations into density fluctuations which will generate a stationary wave of initial amplitude A_0 and constant wavelength of λ. In most simulations presented in this work, this density fluctuation will be considered at $t = 0$ with $A_0 = 3$ *lu* and $\lambda = 160$ *lu*, as

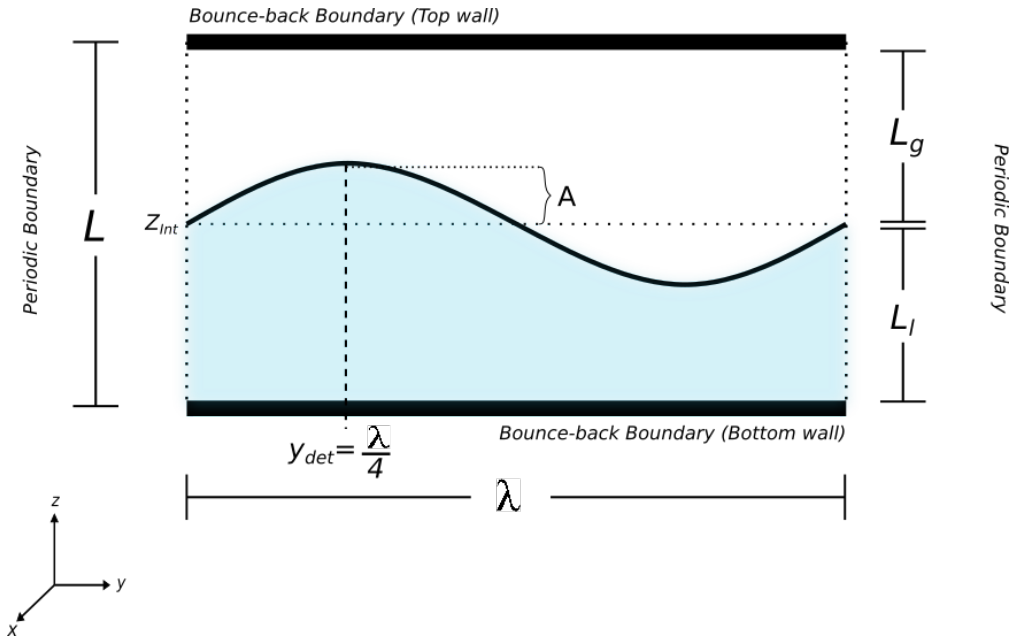

Figure 5.2: Initial configuration of a stationary capillary wave in confined geometries with a spatial domain of $[1, 1] \times [1, \lambda] \times [1, L]$ and amplitude A.

illustrated in Fig. 5.2. Numerically, the thermodynamic equilibrium means that the system has reached ρ_l and ρ_g dictated by equation (4.11) and a diffuse density profile that can be adjusted by the profile

$$\rho(z) = \frac{\rho_l - \rho_g}{2} \tanh\left(\frac{z - z_0}{2\xi}\right) + \frac{\rho_l + \rho_g}{2}, \tag{5.1}$$

with z_0 the location of the interface which, from now on and, as notation in Fig. 5.2 suggests, will be referred to as z_{int}. Once thermodynamic equilibrium is reached in the simulation, the density fluctuation is defined as a sine function

$$z_w(y) = z_0 + A_0 \sin\left(\frac{2\pi\, y}{\lambda}\right), \tag{5.2}$$

that will generate the density profile corresponding to a capillary wave like the one illustrated in Fig. 5.2:

$$\rho(y, z) = \frac{\rho_l - \rho_g}{2} \tanh\left(\frac{z - z_w(y)}{2\xi}\right) + \frac{\rho_l + \rho_g}{2}. \tag{5.3}$$

Note that, for equation (5.2), the maximum amplitude of the wave occurs when $y = \lambda/4$ since $z_w(y = \lambda/4) = z_0 + A_0$, hence to analyze the temporal evolution of the amplitude $A(t)$ given this initial setup, a detector that measures the position of the interface with time, is located at $y_{det} = \lambda/4$. For this interface tracking analysis, based on the density profile

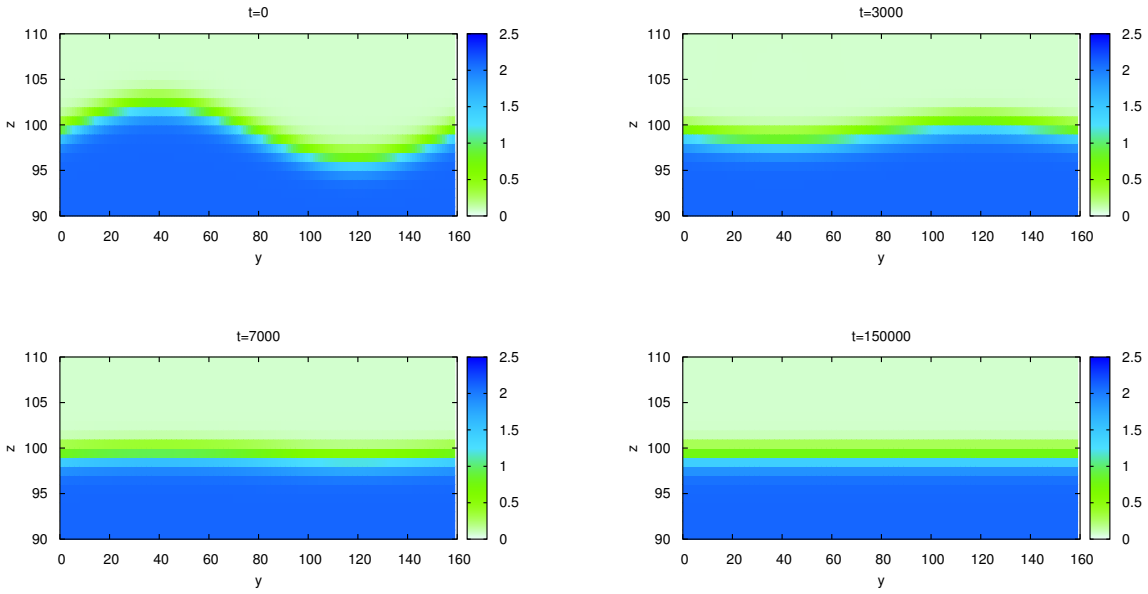

Figure 5.3: Density profile of a stationary capillary wave with initial density profile defined by equation (5.3), with $G = -5.3$, $\tau = 1.0$, $L = 200\ lu$, $z_{int} = 100\ lu$, $A_0 = 3\ lu$ and $\lambda = 160\ lu$. Only the region of interest of the z-axis is shown in the figure. Color green represents the density of the gas $\rho_g = 0.07823$ and blue that of the liquid $\rho_l = 2.107$. The different figures represent snapshots of the evolution of the system in time. The wave damps out gradually until the interface reaches a flat profile as the one defined in equation (5.1).

defined in equation (5.3), the location of the interface z_{det} will be defined as the position along the z-direction in y_{det} where $z_{det} = \frac{\rho_l+\rho_g}{2}$, where a second order interpolation was used to establish its value.

When considering the effects of the geometry into the evolution of confined waves, the parameters to vary, from Fig. 5.2, are: z_{int} and L which will translate into a variation of L_g and L_l. I will also consider the effects of varying the value of surface tension σ determined by different values of the temperature like parameter, $G = -5.1, -5.3, -5.5$. To reduce the cases of study, all simulations will have a fixed value of $\tau = 1.0$, hence I will only analyze effects of different temperature like parameters and different geometries into the temporal evolution of the system for a single viscosity parameter.

First, I will develop the particular case of $G = -5.3$, and $L = 200\ lu$, I will analyze the dynamics of the system given $z_{int} = 100\ lu$. These values of G and τ result into values for the densities at equilibrium of $\rho_l = 2.107$ and $\rho_g = 0.07823$. The initial configuration for a system with these characteristics is illustrated in Fig. 5.3 at $t = 0$ together with its evolution in time until $t = 150000$.

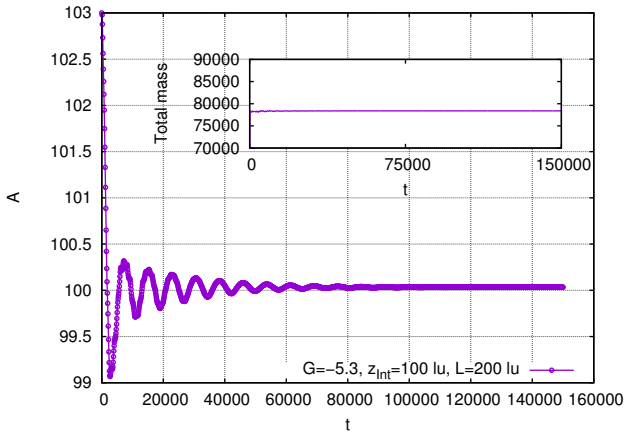

Figure 5.4: Dynamics of the amplitude of the wave for a spatial domain of $[1, 160] \times [1, 200]$, with $G = -5.3$, periodic boundary conditions along the horizontal domain and bounce-back in top and bottom boundaries.

Fig. 5.4 shows values of the interface position. It represents the temporal evolution of the position of the amplitude. This figure also shows an important condition that the method needs to fulfill at all times, that is, conservation of total mass of the system. This condition will no longer be mentioned in next results, nonetheless, it is fulfilled by all simulations.

Once a general overview to the initial setup of simulations for this section is presented and before going for an analysis of the influence different geometries have in the dynamics of a stationary capillary wave, it is important to mention how the conditions of initial thermodynamic equilibrium were constructed in numerical simulations for this work. Using previous results for ρ_l and ρ_g obtained from the analysis made for phase transitions in chapter 4, and given different values of the temperature like parameter, the spatial domain described in the previous example $[1, 160]\times[1, 200]$, was initialized with a diffuse interface density profile as the one described in equation (5.1). Note that this equation already represents a flat interface. Next, I analyzed the changes of location of the interface in time, which is already supposed to be in equilibrium, nonetheless, as Fig. 5.5 indicates, the interface suffers some small amplitude and high frequency oscillations even though I have not added any density fluctuations. These particular oscillations, whose frequency was measured with a Fourier transform of the amplitude signal presented in same Fig. 5.5, will be ignored in the rest of the results presented in this work, since they result to be a phenomenon of the initial setup of the system and not the capillary wave *per se*. These peculiar oscillations will have higher frequency and amplitude for smaller values of G which represent a larger surface tension, but are still insignificant to the dynamics that is of interest to this work. Another peculiarity that this initial setup will present, is a small shift of the original posi-

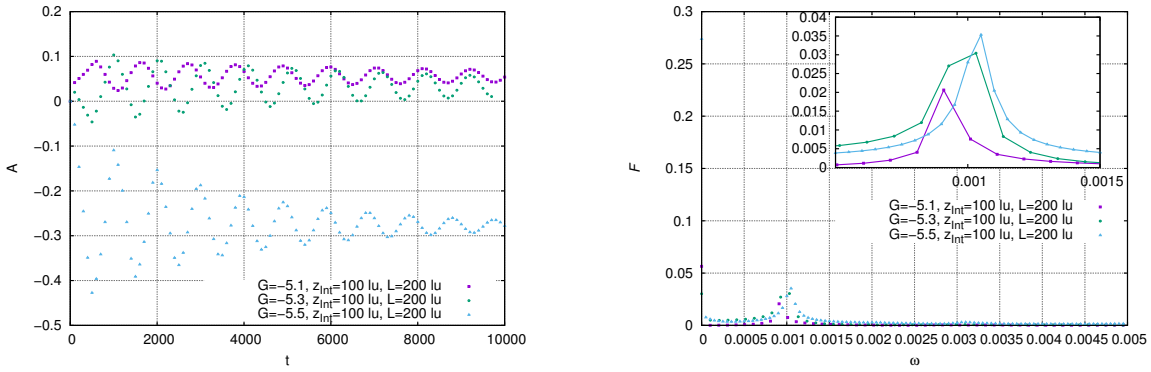

(a) Interface position.

(b) Fourier transform

Figure 5.5: Interface position for a system at initial equilibrium with no wave, illustrating the temporal evolution of the system for different values of G and with initial density profile defined by equation (5.1), with $\tau = 1.0$, $L = 200\ lu$ and $z_{int} = 100\ lu$ as well as the Fourier transform of the signal.

G	ρ_l	ρ_g
-5.1	1.964	0.1035
-5.3	2.107	0.07823
-5.5	2.242	0.05625

Table 5.1: Different study cases for the temperature like parameter G and its densities at phase equilibrium ρ_l and ρ_g.

tion of the interface z_{int}. This shift is, at most, less than half of a lattice unit and is due to a small condensation or evaporation of the fluid. Effect that will also be ignored in results since mass is still conserved and will not affect the evolution of the wave considering it manifests itself even when the system is initialized without a wave.

5.3 Results and analysis

In this final section, I will analyze some representative cases of the study of capillary waves in confined geometries. The selected cases are described in Table 5.1 for the values of the temperature like parameter G and its respective densities ρ_l and ρ_g, and in Table 5.2 for the different geometries defined by the variation of either L, z_{int} or both.

I will first analyze, for $G = -5.3$, the three cases for fixed L defined in Table 5.2. Results for the evolution of the amplitude are shown in Fig. 5.6 for $L = 200\ lu$, considering for each case z_{int} as the origin of the z-axis. From the plot, a recognizable difference in the oscillatory

Different Geometries	Case 1		Case 2		Case 3	
	L	z_{int}	L	z_{int}	L	z_{int}
Fixed L	200 lu	100 lu	200 lu	150 lu	200 lu	50 lu
Height			300 lu	100 lu	400 lu	100 lu
Depth				200 lu		300 lu

Table 5.2: Different study cases defined by different geometries of the spatial domain. Parameters L and z_{int} represent the total depth of the domain ($L_l + L_g$) and the location of the interface respectively, both in lattice units (lu).

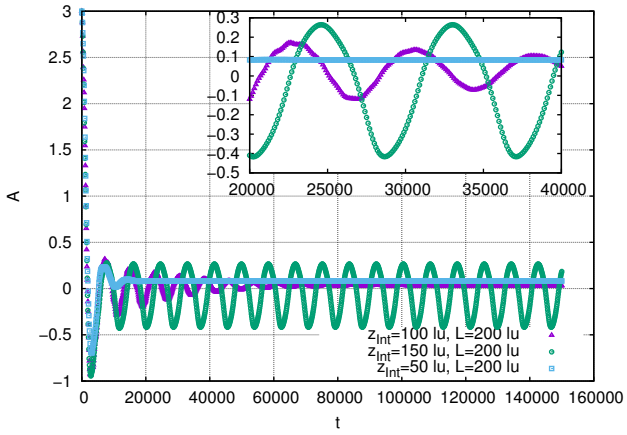

Figure 5.6: Dynamics of the amplitude of the wave for a spatial domain of $[1, 160] \times [1, 200]$, with $G = -5.3$, $A_0 = 3.0$ lu, periodic boundary conditions along the horizontal domain and bounce-back in top and bottom boundaries and different positions of the interface: $z_{int} = 100$ lu, 150 lu and 50 lu.

behaviour of the system is noticeable. It seems like if the closer the top boundary is from the position of the wave (case 2), the more oscillations the system presents as if this region defined an underdamped regime for the system. Whereas the farther the wave is from the top wall of the system (case 3), the fewer oscillations it presents, as an overdamped regime would.

Fig. 5.7 shows results for 3 different cases of height defined in Table 5.2. These different simulations are used to analyze the influence of $L_g = L - z_{int}$ in the oscillatory behavior of the wave and confirm the effect the top boundary has over the evolution of it. Considering that the blue squares, which plot the most overdamped curve of the three, correspond to the geometrical configuration with the furthest-away top boundary, it is possible to conclude that, at least for $G = -5.3$, the distance of the top boundary, which represents the ceiling of

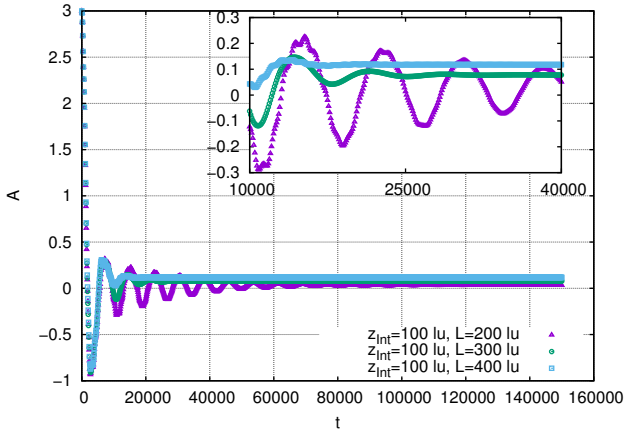

Figure 5.7: Dynamics of the amplitude of the wave for different spatial domains defined in cases 1, 2 and 3 for Height geometries in Table 5.2. With $[1, 160] \times [1, L]$ defining the spatial domain and with $G = -5.3$, $A_0 = 3.0$ *lu*, periodic boundary conditions along the horizontal domain and bounce-back in top and bottom boundaries and same position $z = 100$ *lu* for the interface. This plot shows the influence of $L_g = L - z_{int}$ (From Fig. 5.2) over the oscillatory behaviour of the wave.

the system, over the position of the capillary wave, damps the oscillatory behaviour of the interface.

On the same note, Fig. 5.8 shows how, depending on the distance between the top boundary and the interface position, the frequency of the damping of the wave suffers a soft linear increase in its value. Hence, not only does L_g modifies the overall behaviour of the system but also its initial response to the surface tension and fluid viscosity as two of the main forces that govern the system.

To verify whether the same result was also valid for the depth L_l of the system, three cases labeled as Depth in Table 5.2 were analyzed.

Fig. 5.9 shows there is a threshold for L_l for which the closer the wave is to the bottom of the system, the more damped its evolution is. Hence the distance of this boundary to the relative position of the interface L_l has the opposite effect over the evolution of the interface than that of L_g. As expected, based on this result, same thing happens for the frequency of oscillations, instead of linearly increasing, they decrease, see linear fit in Fig. 5.8.

The later results were for $G = -5.3$, but surprisingly the dynamics is not similar for other values of G. Same three cases for Height and Depth geometries were simulated and results show that L_g and L_l when $G = -5.1$ and $G = -5.5$, do not interfere over the overdamped (all geometries for G=-5.1) or underdamped (all geometries for G=-5.5) regime of the system. Whereas they do have an effect on the representative frequencies

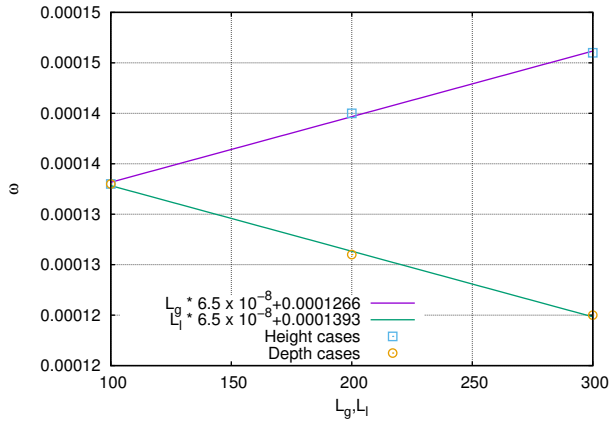

Figure 5.8: Values of the frequencies of the damping for the 6 different cases defined in Table 5.2 under the names of Height and Depth. These values illustrate the effect the different geometries have on the frequency of the system.

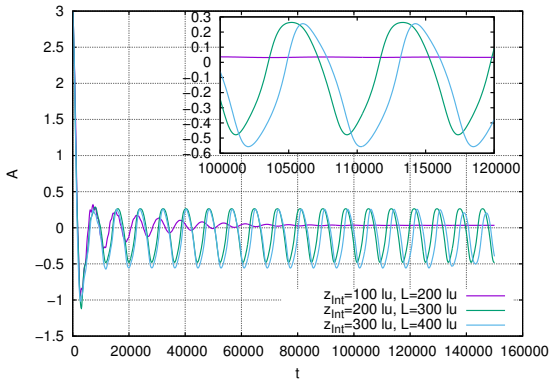

Figure 5.9: Dynamics of the amplitude of the wave for different spatial domains defined in cases 1, 2 and 3 for Depth geometries of Table 5.2. With $[1:160]\times[1:L]$, with $G=-5.3$, $A_0=3.0$ *lu*, periodic boundary conditions along the horizontal domain and bounce-back in top and bottom boundaries and different positions of the interface z_{int}.

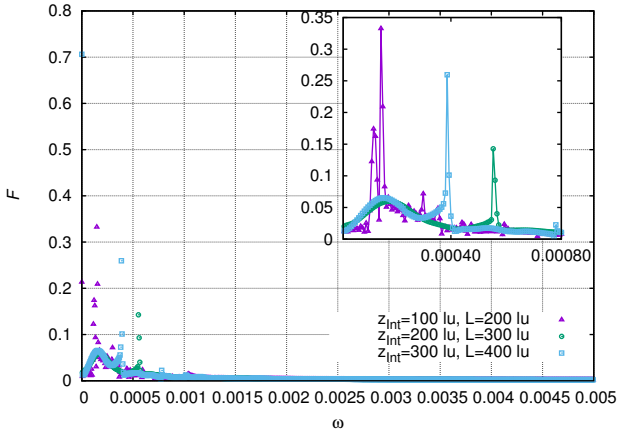

Figure 5.10: Fourier transform of the amplitudes of wave simulated using Depth geometries of Table 5.2. With $[1, 160] \times [1, L]$, $G = -5.5$, $A_0 = 3.0$ lu, periodic boundary conditions along the horizontal domain and bounce-back in top and bottom boundaries and different positions of the interface z_{int}.

of the motion. Fig. 5.10 presents the Fourier transform of the amplitudes $A(t)$ for cases corresponding to different depths of the system when $G = -5.5$. Each case shows two different frequencies for each value of L_g when the depth of the system is modified. First value, which approximately coincides regardless of the geometry, corresponds to the initial damping of the system, same as the one observed when $G = -5.3$. The other frequencies observed in this plot, the ones that do not coincide for any G, correspond to the remaining oscillation of the system that takes place due to the high value of surface tension that $G = -5.5$ represents. On this note, it is also verified that even when the value of the G parameter determines two damping regimes, it does not determine the values of the frequency of the damping which is rather influenced by the different values of z_{int} and L.

Finally, Tables 5.3 and 5.4 summarize all main results presented in this chapter. In Table 5.3 I show frequencies for all cases when $G = -5.3$. If case 1, whose parameters of L and z_{int} are the same for all 3 geometries: Fixed L, Height or Depth, is considered as the standard case, since it has the property of $L_g = L_l = 100$ lu, notice that its frequency is $\omega = 0.000133 = \omega_0$, value by which the rest of the frequencies are normalised in both tables. Parting from this value, Table 5.3 shows the influence of L_g over the frequency: all boxes in the darker grey have a higher frequency than ω_0, but also larger values of L_g than 100 lu, hence, as concluded before, the further the top boundary is from the interface, the bigger its damping effect over the wave. On the contrary, all boxes in the lighter grey have smaller values of the frequency than ω_0 and at the same time, larger values of L_l than 100 lu. Therefore, L_l decreases the value of the frequency when it increases by damping the behaviour of the system the closer it is.

$G = -5.3$			
	Case 1	Case 2	Case 3
Fixed L	1.00	0.902255	1.097744
Height		1.052631	1.097744
Depth		0.947368	0.902255

Table 5.3: Frequencies of the damping for all cases when $G = -5.3$. Note that all values are normalised by $\omega_0 = 0.000133$, which is the value of the frequency for the case shown in Fig. 5.4, with $G = -5.3$, $L = 200\ lu$ and $z_{int} = 100\ lu$. Darker grey shows the influence of L_g over the frequency: the further the top boundary is from the interface, the bigger its damping effect over the wave. Lighter grey shows the effect of L_l. This parameter decreases the value of the frequency when it increases by damping the behaviour of the system the closer it is.

	$L = 200\ lu, z_{int} = 100\ lu$	$L = 400\ lu, z_{int} = 100\ lu$	$L = 400\ lu, z_{int} = 300\ lu$
$G = -5.1$	1.00	0.947368	1.052631
$G = -5.3$	1.00	1.097744	0.902255
$G = -5.5$	1.097744	1.097744	1.150375

Table 5.4: Influence of G over the dynamics of the system. The numerical values represent the frequencies of the damping normalised by $\omega_0 = 0.000133$.

Table 5.4 presents the influence of G over the dynamics of the system. Nonetheless its influence is not as straightforward as that of the geometry. From the tables it looks like this parameter only defines a threshold over which the system is either overdamped ($G = -5.1$) or underdamped ($G = -5.5$) without a soft transition between the two regimes. As future analysis, the study of more cases of G may reveal a more clear influence of this parameter over the system, since, at the end of the day, it defines the surface tension of the fluid.

Up to now, this chapter has been mostly descriptive. The next and final section will present a discussion from the physical point of view of the previous results.

5.4 Discussion and future work

An interfacial wave such as a capillary wave, is affected by restoring forces during the evolution toward the equilibrium, forces that will generate recirculation of the fluid above and bellow the interface as shown in Fig. 5.11.

The resulting flow patterns eventually reach the nearby walls and bounce back towards the interface with which it interferes. The closer the walls, the more the recirculation will be perturbed and the stronger the waves will be affected by the geometry of the domain. The velocity of recirculation will depend upon the viscosity and density of the fluid. For the case of interfacial capillary waves, even when the fluid in both sides of the wave is the same, density is not and, with it, neither is the dynamic viscosity. Therefore the surrounding walls of the system will have different effects depending on the fluid with which they are in contact. This explains why top wall which is surrounded by gas has a different impact over the evolution of the wave than that of the bottom wall in contact with liquid. This argument is shown in Fig. 5.12, that shows the vorticity of the system $\nabla \times \mathbf{v}$, for different times when $G = -5.3$, $L = 200$ and $z_{int} = 100$. In this figure it is clear how after $t \sim 400$ the effect of the top boundary is reflected towards the interface such that at t the effects have already reached the interface intervening in the dynamics of the wave. This is the reason why the frequency of the damping ω, depends on the system.

The previous discussion of the results, encourages to pose more questions that will be tackled in further analysis, including a quantitative description of the effects of boundaries on the flow patterns interfering with the interface.

In the meanwhile, in next an final chapter, I will review the work presented in this dissertation with some conclusions and an outlook of the research.

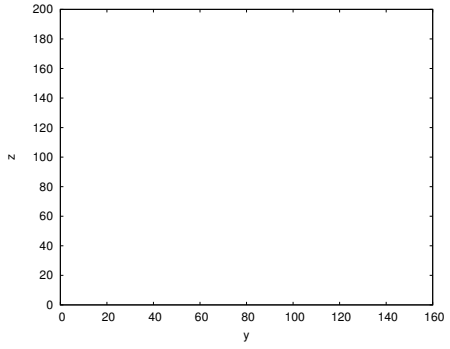

(a) $t = 0$

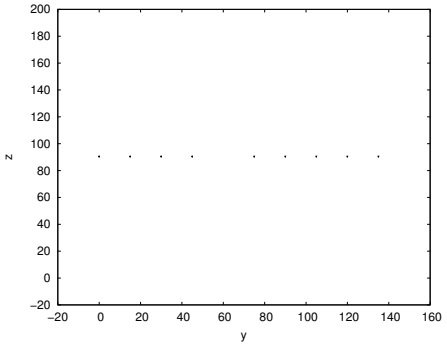

(b) $t = 100$

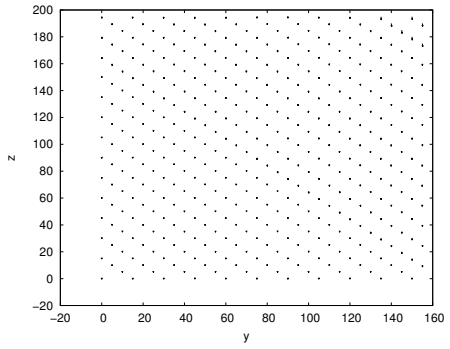

(c) $t = 200$

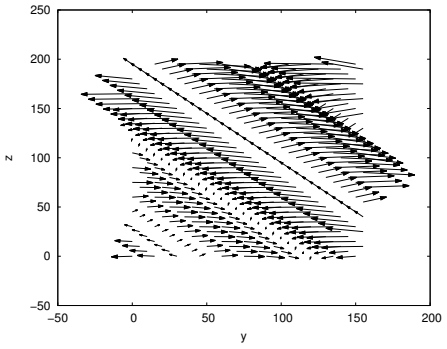

(d) $t = 300$

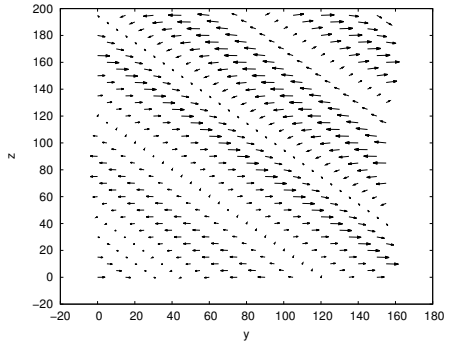

(e) $t = 400$

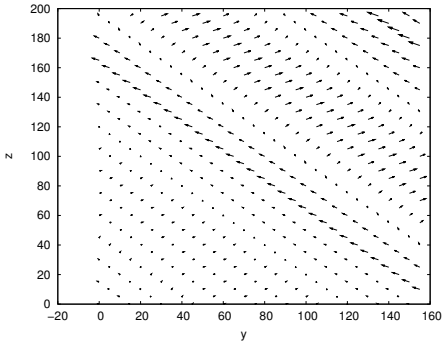

(f) $t = 4000$

Figure 5.11: Vector field of the system scaled by a factor of 5×10^5 for different times with $G = -5.3$, $\tau = 1.0$, $L = 200$ *lu*, $z_{int} = 100$ *lu*, $A_0 = 3$ *lu* and $\lambda = 160$ *lu*. The different plots show the evolution of the redistribution of the flow patterns.

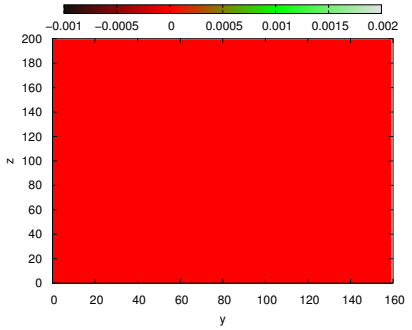

(a) $t = 0$

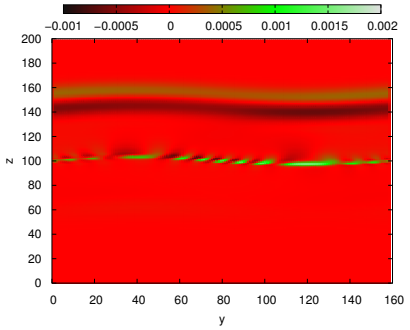

(b) $t = 100$

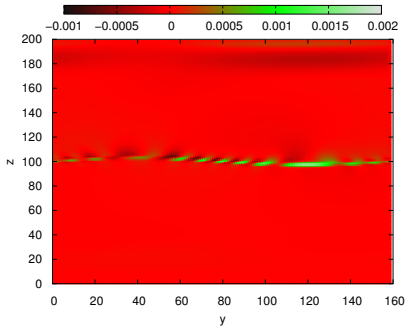

(c) $t = 200$

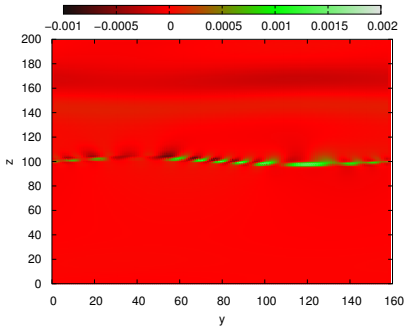

(d) $t = 300$

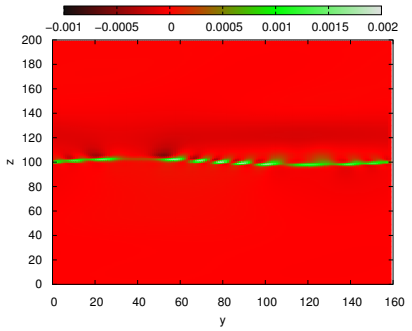

(e) $t = 400$

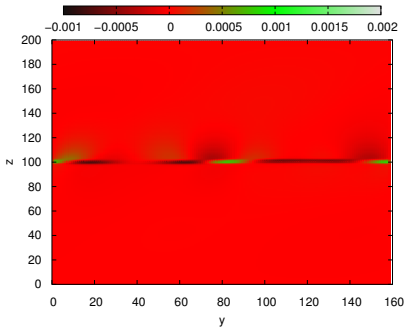

(f) $t = 4000$

Figure 5.12: Vorticity $\nabla \times \mathbf{v}$ of the system for different times with $G = -5.3$, $\tau = 1.0$, $L = 200\ lu$, $z_{int} = 100\ lu$, $A_0 = 3\ lu$ and $\lambda = 160\ lu$. The different plots show the evolution of the resulting flow patterns which eventually reach the top wall at $t \sim 200$ and bounce back towards the interface with which it interferes at $t \sim 400$.

Chapter 6

Conclusions

In this work I presented a totally functional code in FORTRAN 90 implemented from scratch and without the use of any library or packages. The code is a lattice Boltzmann method implementation extended with a Shan-Chen approach making it capable of simulating in 3 dimensions, a two phase fluid throughout a considerable range of density ratios. Along the work, I presented all basic benchmark tests that ensure the correct implementation of this numerical method and discussed important topics to the implementation of it such as the non-dimesionalization of the code, boundary conditions and the introduction of a forcing scheme crucial to the Shan-Chen model.

I also included an explicit mathematical derivation of the main equation used within this model, the lattice Boltzmann equation, and how it is linked to the macroscopic analysis of a fluid by introducing the Chapman Enskog analysis, in charge of recovering the hydrodynamics of the system parting from the kinetic approach that the Lattice Boltmann Method uses.

In the last chapter, I included the main results of this work, where I analyzed the temporal evolution of the amplitude of a stationary capillary wave in confined geometries. Prior to this dissertation, up to the best of my knowledge, there are no studies that analyze the dynamics of standing capillary waves under this conditions, not even with other numerical methods or experimentally. Studies that could have useful application mainly to understand properties of multiphase fluids since, for example, the analysis of capillary waves can reveal information such as surface tension or viscosity of fluids when not known.

All the analysis here presented, leads me to conclude that, even with the limitations that the Shan-Chen approach presents, regarding, for example, a relatively short range of density ratios in comparison to other methods, its advantages are more relevant to the study of this particular system: the surface tension being an emergent effect, as well as the coexistence of two phases added to the fact that there is no need of the inclusion of another

numerical or analytic tools in charge of tracking the interface between the two phases, these advantages allow more freedom to the evolution of intricate interfacial geometries, which is crucial in the analysis of capillary waves, as interfacial perturbations of the pressure that they are.

Regarding the influence the geometry has over the evolution of the system, the analysis is still young and much work is needed ahead. Nonetheless, the results that I present are a clear indicator that different geometries influence in different ways the dynamics of standing capillary waves. Hence not only the study of the influence of the bottom wall is important in the analysis of these systems, concluding that previous results about waves in shallow waters do not apply to the analysis of this work.

The previous conclusion and results from last chapter, also leads me to stand out the lack of experimental results and theoretical analysis towards the study of capillary waves in confined geometries. Experimental results in this topic could have been a solid basis of comparison of our numerical results, in the mean time, all that there is as validation of these results are the benchmark cases that were used also to test the validity of the code here presented.

Finally, as an important remark, there is possibility for further analysis regarding this topic: a bigger range of values for surface tension, the inclusion of viscosity as a free parameter or the analysis of a broader range of geometries, for example, waves that no longer have a symmetry along the third dimension or that are confined in another direction such as a rectangular pipe.

Appendix A

Method of Characteristics

In this appendix, the full mathematical procedure used to discretise in space and time the Boltzmann equation will be described . Taking equation (3.20) as the starting point

$$\frac{\partial f_k(\mathbf{x},t)}{\partial t} + \hat{\mathbf{c}}_k \cdot \nabla f_k(\mathbf{x},t) = -\frac{f_k(\mathbf{x},t) - f_k^{eq}(\mathbf{x},t)}{\tau}, \tag{A.1}$$

which is a first order hyperbolic partial differential equation and using the method of characteristics, the existence of a parameter χ that parametrises a trajectory along which this PDE becomes an ordinary differential equation (ODE) will be assumed.

The new system to solve in terms of this parameter χ, is

$$\frac{\mathrm{d}f_k}{\mathrm{d}\chi} = \frac{\partial f_k}{\partial t}\frac{\mathrm{d}t}{\mathrm{d}\chi} + \frac{\partial f_k}{\partial x_\alpha}\frac{\mathrm{d}x_\alpha}{\mathrm{d}\chi} = -\frac{f_k - f_k^{eq}}{\tau} \tag{A.2}$$

along the trajectories

$$t(\chi) = \chi + t_0, \qquad \mathbf{x}(\chi) = \hat{\mathbf{c}}_k\chi + \mathbf{x}_0$$

such that

$$\frac{\mathrm{d}t}{\mathrm{d}\chi} = 1, \qquad \frac{\mathrm{d}x_\alpha}{\mathrm{d}\chi} = \hat{c}_{k\alpha}$$

with initial conditions $t(0) = t_0$ and $\mathbf{x}(0) = \mathbf{x}_0$, recovering then equation (A.2). Rewriting equation (A.2) now in the form of an ODE,

$$\frac{\mathrm{d}f_k(\chi)}{\mathrm{d}\chi} + \frac{1}{\tau}f_k(\chi) = \frac{1}{\tau}f_k^{eq}(\chi)$$

and multiplying both sides by $e^{\frac{\chi}{\tau}}$,

$$\underbrace{e^{\frac{\chi}{\tau}}\frac{\mathrm{d}f_k(\chi)}{\mathrm{d}\chi}+\frac{e^{\frac{\chi}{\tau}}}{\tau}f_k(\chi)}_{\frac{\mathrm{d}}{\mathrm{d}t}(e^{\frac{\chi}{\tau}}f_k(\chi))}=\frac{e^{\frac{\chi}{\tau}}}{\tau}f_k^{eq}(\chi)$$

a total differential is obtained,

$$\frac{\mathrm{d}}{\mathrm{d}t}(e^{\frac{\chi}{\tau}}f_k(\chi))=\frac{e^{\frac{\chi}{\tau}}}{\tau}f_k^{eq}(\chi) \tag{A.3}$$

which can be integrated over one time step of size Δt. For the left-hand side:

$$\begin{aligned}\int_{\chi_0}^{\chi_0+\Delta t}\mathrm{d}(e^{\frac{\chi'}{\tau}}f_k(\chi'))&=e^{\frac{\chi'}{\tau}}f_k(\chi')|_{\chi_0}^{\chi_0+\Delta t}\\&=e^{\frac{\chi_0+\Delta t}{\tau}}f_k(\mathbf{x}_0+\hat{\mathbf{c}}_k(\chi_0+\Delta t),t_0+\chi_0+\Delta t)-e^{\frac{\chi_0}{\tau}}f_k(\mathbf{x}_0+\hat{\mathbf{c}}_k\chi_0,t_0+\chi_0).\end{aligned}$$

Choosing integration constants arbitrarily as $\chi_0=0$ and $\mathbf{x}=\mathbf{x}_0$, $t=t_0$, the result is

$$\int_{\chi_0}^{\chi_0+\Delta t}\mathrm{d}(e^{\frac{\chi'}{\tau}}f_k(\chi'))=e^{\frac{\Delta t}{\tau}}f_k(\mathbf{x}+\hat{\mathbf{c}}_k\Delta t,t+\Delta t)-f_k(\mathbf{x},t),$$

whereas for the right hand side:

$$\int_{\chi_0}^{\chi_0+\Delta t}\frac{1}{\tau}f_k^{eq}(\chi')\mathrm{d}\chi'=\frac{1}{\tau}\int_t^{t+\Delta t}f_k^{eq}(\mathbf{x}-\hat{\mathbf{c}}_k(t'-t),t')e^{\frac{t'-t}{\tau}}\mathrm{d}t'.$$

Matching right and left hand sides

$$e^{\frac{\Delta t}{\tau}}f_k(\mathbf{x}+\hat{\mathbf{c}}_k\Delta t,t+\Delta t)-f_k(\mathbf{x},t)=\frac{1}{\tau}\int_t^{t+\Delta t}f_k^{eq}(\mathbf{x}-\hat{\mathbf{c}}_k(t'-t),t')e^{\frac{t'-t}{\tau}}\mathrm{d}t',$$

finally results in the integral-form solution of the Lattice BGK equation:

$$f_k(\mathbf{x}+\hat{\mathbf{c}}_k\Delta t,t+\Delta t)=\frac{e^{-\frac{\Delta t}{\tau}}}{\tau}\int_t^{t+\Delta t}f_k^{eq}(\mathbf{x}-\hat{\mathbf{c}}_k(t'-t),t')e^{\frac{t'-t}{\tau}}\mathrm{d}t'+e^{-\frac{\Delta t}{\tau}}f_k(\mathbf{x},t). \tag{A.4}$$

In order to discretise this integral solution, Δt is assumed small and f_k^{eq} locally smooth, hence, after using the forward Euler approximation

$$\int_t^{t+\Delta t}f_k^{eq}(\mathbf{x}-\hat{\mathbf{c}}_k(t'-t),t')e^{\frac{t'-t}{\tau}}\mathrm{d}t'=f_k^{eq}(\mathbf{x},t)\Delta t, \tag{A.5}$$

results into an equation that, when using a Taylor expansion of the exponential, reads

$$\begin{aligned} f_k(\mathbf{x} + \hat{\mathbf{c}}_k \Delta t, t + \Delta t) = & \underbrace{e^{-\frac{\Delta t}{\tau}}}_{1-\frac{\Delta t}{\tau}+O(\Delta t^2)} \frac{1}{\tau} f_k^{eq}(\mathbf{x}, t)\Delta t + \underbrace{e^{-\frac{\Delta t}{\tau}}}_{1-\frac{\Delta t}{\tau}+O(\Delta t^2)} f_k(\mathbf{x}, t) \\ &= \left(1 - \frac{\Delta t}{\tau} + O(\Delta t^2)\right) \frac{1}{\tau} f_k^{eq}(\mathbf{x}, t)\Delta t + \left(1 - \frac{\Delta t}{\tau} + O(\Delta t^2)\right) f_k(\mathbf{x}, t) \\ &= \left(\frac{\Delta t}{\tau} - \frac{\Delta t^2}{\tau^2} + O(\Delta t^3)\right) f_k^{eq}(\mathbf{x}, t) + \left(1 - \frac{\Delta t}{\tau} + O(\Delta t^2)\right) f_k(\mathbf{x}, t), \end{aligned}$$

notice that $\hat{\mathbf{c}}_k \Delta t = \Delta \mathbf{x}$ with $\Delta \mathbf{x}$ along the k-direction. Keeping only terms up to first order in Δt, last equation reduces to

$$f_k(\mathbf{x} + \hat{\mathbf{c}}_k \Delta t, t + \Delta t) = f_k(\mathbf{x}, t) - \frac{\Delta t}{\tau} f_k(\mathbf{x}, t) + \frac{\Delta t}{\tau} f_k^{eq}(\mathbf{x}, t) + O(\Delta t^2).$$

After comparing this equation with equation (3.1), the **Lattice Bhatnagar Gross Krook equation** discretised in velocity space, physical space and time is obtained:

$$\underbrace{f_k(\mathbf{x} + \hat{\mathbf{c}}_k \Delta t, t + \Delta t)}_{\text{streaming}} = f_k(\mathbf{x}, t) + \underbrace{\frac{\Delta t}{\tau} \left(f_k^{eq}(\mathbf{x}, t) - f_k(\mathbf{x}, t)\right)}_{\text{collision}}, \tag{A.6}$$

a special case of the Lattice Boltzmann equation that uses the BGK collision operator.

Appendix B

Boundary Conditions in 2 Dimensions

This appendix includes all boundary conditions in 2D used in this work. In this case, the spatial domain has 4 boundaries and not 6 as in 3D:

1. North face: all boundary nodes where $y = y_{max}$ with its associated distribution functions as f_k^{north}.

2. South face: nodes where $y = y_{min}$ with f_k^{south}.

3. East face: boundary nodes where $x = x_{max}$ with f_k^{east}.

4. West face: $x = x_{min}$ with f_k^{west}.

B.1 Periodic Boundary Conditions in 2D.

Like in 3 dimensions, periodic boundary conditions are the easiest case. May be suitable for periodic or to simulate infinite domains.

Periodic East and West Boundary Conditions.

The schematic diagram of this boundary lattice sites is given in Fig. B.1. At the west boundary, the inlet particle distributions for a 2D problem f_1, f_5 and f_8 are unknown after the streaming operation, their values are obtained from the respective outlet particle distribution function from the east, that is:

$$\begin{aligned} f_1^{west} &= f_1^{east} \\ f_5^{west} &= f_5^{east} \\ f_8^{west} &= f_8^{east} \end{aligned} \tag{B.1}$$

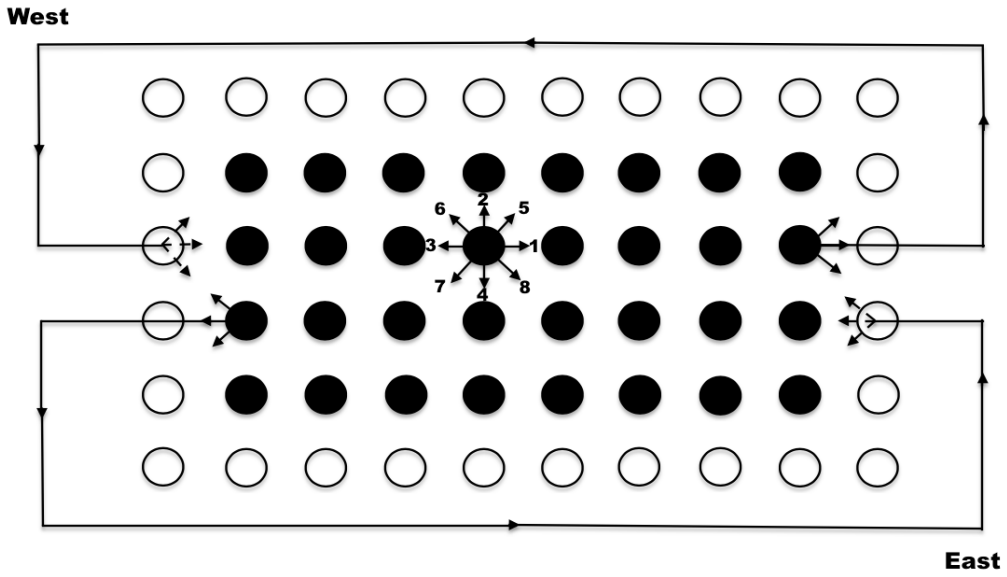

Figure B.1: Illustration of east and west periodic boundary conditions in 2 dimensions for the LBM D2Q9.

On the other side, at the east boundary, f_3, f_6 and f_7 are unknown and obtained from the respective outlet particle distribution from the west side:

$$\begin{aligned} f_3^{east} &= f_3^{west} \\ f_6^{east} &= f_6^{west} \\ f_7^{east} &= f_7^{west} \end{aligned} \tag{B.2}$$

For the northern and southern boundaries, the relations are obtained in an analog manner.

B.2 Bounce-Back Boundary Conditions in 2D

Once again, the construction is similar as for the 3D case, notation is also similar with $\mathbf{x_B}$ the boundary node and simplifying notation with $f_k(t + \Delta t) = f_k(\mathbf{x_B}, t + \Delta t)$.

North:

$$\begin{aligned} f_7^{north}(t + \Delta t) &= f_5^{\star north}(t) \\ f_4^{north}(t + \Delta t) &= f_2^{\star north}(t) \\ f_8^{north}(t + \Delta t) &= f_6^{\star north}(t) \end{aligned} \tag{B.3}$$

South:

$$\begin{aligned} f_5^{south}(t+\Delta t) &= f_7^{\star\,south}(t) \\ f_2^{south}(t+\Delta t) &= f_4^{\star\,south}(t) \\ f_6^{south}(t+\Delta t) &= f_8^{\star\,south}(t) \end{aligned} \tag{B.4}$$

East:

$$\begin{aligned} f_6^{east}(t+\Delta t) &= f_8^{\star\,east}(t) \\ f_3^{east}(t+\Delta t) &= f_1^{\star\,east}(t) \\ f_7^{east}(t+\Delta t) &= f_5^{\star\,east}(t) \end{aligned} \tag{B.5}$$

West:

$$\begin{aligned} f_5^{west}(t+\Delta t) &= f_7^{\star\,west}(t) \\ f_1^{west}(t+\Delta t) &= f_3^{\star\,west}(t) \\ f_8^{west}(t+\Delta t) &= f_6^{\star\,west}(t) \end{aligned} \tag{B.6}$$

This type of boundary is used in this work for the lid driven cavity.

B.3 Specification of Pressure and Velocity Boundary Conditions using the Zou-He Scheme

As mentioned, in the lattice Boltzmann method, the pressure is related to the density by the isothermal equation of state,

$$p = c_s^2 \rho,$$

implying that, a specification of pressure difference means a specification of density difference.

East: Consider a 2 dimensional domain, with

$$p_{out} = c_s^2 \rho_{out}$$

where ρ_{out} and p_{out} are the values of density and pressure at the east boundary and p_{out} is a given value of pressure at that boundary. Explicitly, the conditions for f_3, f_6, f_7 and the x-component of u are

$$
\begin{aligned}
u_x &= \frac{1}{\rho_{out}}(f_0 + f_2 + f_4 + 2(f_1 + f_5 + f_8)) - 1 \\
f_3 &= f_1 - \frac{2}{3}\rho_{out}u_x \\
f_6 &= f_8 - \frac{1}{2}(f_2 - f_4) - \frac{1}{6}\rho_{out}u_x + \frac{1}{2}\rho_{out}u_y \\
f_7 &= f_5 + \frac{1}{2}(f_2 - f_4) - \frac{1}{6}\rho_{out}u_x - \frac{1}{2}\rho_{out}u_y
\end{aligned}
\tag{B.7}
$$

and if a velocity $u_{x_{out}} = u_x$ is required to hold at the boundary instead of the pressure, then

$$
\rho_{out} = \frac{1}{1 + u_x}(f_0 + f_2 + f_4 + 2(f_1 + f_5 + f_8)).
$$

West: At boundary segment, the specified values for density and pressure are related by

$$
p_{in} = c_s^2 \rho_{in},
$$

implying that

$$
\begin{aligned}
u_x &= 1 - \frac{1}{\rho_{in}}(f_0 + f_2 + f_4 + 2(f_6 + f_3 + f_7)) \\
f_1 &= f_3 + \frac{2}{3}\rho_{in}u_x \\
f_5 &= f_7 - \frac{1}{2}(f_2 - f_4) + \frac{1}{6}\rho_{in}u_x + \frac{1}{2}\rho_{in}u_y \\
f_8 &= f_6 + \frac{1}{2}(f_2 - f_4) + \frac{1}{6}\rho_{in}u_x - \frac{1}{2}\rho_{in}u_y
\end{aligned}
\tag{B.8}
$$

or if the velocity is specified and not the pressure:

$$
\rho_{in} = \frac{1}{1 - u_x}(f_0 + f_2 + f_4 + 2(f_6 + f_3 + f_7)).
$$

North: For a prescribed y-component of the velocity at the top boundary:

$$\begin{aligned}
\rho &= \frac{1}{1+u_y}(f_0+f_1+f_3+2(f_2+f_5+f_6)) \\
f_4 &= f_2 - \frac{2}{3}\rho u_y \\
f_7 &= f_5 + \frac{1}{2}(f_1-f_3) - \frac{1}{2}\rho u_x - \frac{1}{6}\rho u_y \\
f_8 &= f_6 - \frac{1}{2}(f_1-f_3) + \frac{1}{2}\rho u_x - \frac{1}{6}\rho u_y.
\end{aligned} \tag{B.9}$$

If the prescribed value was ρ instead of u_y, solve the first condition for u_y.

South: Again, for a prescribed value of u_y now in the south boundary:

$$\begin{aligned}
\rho &= \frac{1}{1-u_y}(f_0+f_1+f_3+(f_4+f_7+f_8)) \\
f_2 &= f_4 + \frac{2}{3}\rho u_y \\
f_5 &= f_7 - \frac{1}{2}(f_1-f_3) + \frac{1}{2}\rho u_x + \frac{1}{6}\rho u_y \\
f_6 &= f_8 + \frac{1}{2}(f_1-f_3) - \frac{1}{2}\rho u_x + \frac{1}{6}\rho u_y.
\end{aligned} \tag{B.10}$$

The case of a prescribed y-component of the velocity at the top boundary is used in the work for the case of the Couette Flow, whereas the case of specification of pressure at east and west boundaries is used for Poiseuille Flow.

Appendix C

Spurious Currents

In this appendix will be shown how to derive the nonisotropic contributions of the Shan-Chen force due to discretzations of the method [60]. This, by Taylor-expanding to higher orders the pseudopotential $\Psi(\mathbf{x} + \hat{\mathbf{c}}_\mathbf{k}\Delta t)$ around $\mathbf{x}$.

As stated, the forcing term is written in the form

$$\mathbf{F}^{\mathbf{SC}}(\mathbf{x}) = -G\Psi(\mathbf{x})\Sigma_k w_k \Psi(\mathbf{x} + \hat{\mathbf{c}}_\mathbf{k}\Delta t)\hat{\mathbf{c}}_\mathbf{k}\Delta t,$$

so, applying the Taylor expansion to $\Psi(\mathbf{x} + \hat{\mathbf{c}}_\mathbf{k}\Delta t)$ and substituting in $\mathbf{F}^{\mathbf{SC}}$:

$$\begin{aligned} F_\alpha^{SC}(\mathbf{x}) = -G\Psi(\mathbf{x})[&\Psi(\mathbf{x})E^{(1)} + \partial_\beta\Psi(\mathbf{x})E^{(2)}\Delta t^2 + \frac{1}{2!}\partial_\beta\partial_\gamma\Psi(\mathbf{x})E^{(3)}\Delta t^3 \\ &+ \frac{1}{3!}\partial_\beta\partial_\gamma\partial_\mu\Psi(\mathbf{x})E^{(4)}\Delta t^4 + \frac{1}{4!}\partial_\beta\partial_\gamma\partial_\mu\partial_\nu\Psi(\mathbf{x})E^{(5)}\Delta t^5 \\ &+ \frac{1}{5!}\partial_\beta\partial_\gamma\partial_\mu\partial_\nu\partial_\xi\Psi(\mathbf{x})E^{(6)}\Delta t^6 + O(\delta^6)]. \end{aligned} \tag{C.1}$$

Introducing the notation

$$E^{(m)} = E^{(m)}_{\alpha_1\alpha_2\ldots\alpha_m} = \sum_k w_k c_{k\alpha_1} c_{k\alpha_2}\ldots c_{k\alpha_m} \tag{C.2}$$

with $E^{(2n+1)} = 0$ and $E^{(2n)} = c_s^2\Delta^{(2n)}$ where

$$\Delta^{(2n)} = \Delta^{(2n)}_{\alpha_1\alpha_2\ldots\alpha_{2n}} = \sum_{j=2}^{2n} \delta_{\alpha_1\alpha_j}\Delta^{(2n-2)}_{\alpha_2\ldots\alpha_{2n}},$$

and in particular, $\Delta^2_{\alpha\beta} = \delta_{\alpha\beta}$ and $\Delta^4_{\alpha\beta\gamma\mu} = \delta_{\alpha\beta}\delta_{\gamma\mu} + \delta_{\alpha\gamma}\delta_{\beta\mu} + \delta_{\alpha\mu}\delta_{\beta\gamma}$.

Now we will show that the truncated isotropy of the lattice up to the fifth order, induces anisotropic contributions to the Shan-Chen Force, which trigger spurious currents. First,

this truncated isotropy means that all the tensors up to the fifth order are isotropic while the higher order ones are not. Going back to equation (C.1), it then becomes

$$\begin{aligned} F_{\alpha}^{SC}(\mathbf{x}) = -G\Psi(\mathbf{x})[c_s^2\Delta_{\alpha\beta}^2\Delta t^2\partial_\beta\Psi(\mathbf{x}) + \frac{1}{3!}c_s^4\Delta_{\alpha\beta\gamma\mu}^4\Delta t^4\partial_\beta\partial_\gamma\partial_\mu\Psi(\mathbf{x}) \\ + \frac{1}{5!}c_s^6\Delta_{\alpha\beta\gamma\mu\nu\xi}^6\Delta t^6\partial_\beta\partial_\gamma\partial_\mu\partial_\nu\partial_\xi\Psi(\mathbf{x}) + O(\delta^6)]. \end{aligned} \tag{C.3}$$

Finally, after some algebra and assuming spherical symmetry of the pseudopotential, $\Psi = \Psi(r)$ so that $\nabla = \hat{r}\partial_r$ and $\nabla^2 = \partial^2 r + \frac{2\partial_r}{r}$, we obtain (ignoring some constants and coefficients):

$$\mathbf{F}^{SC}(\mathbf{x}) \approx -G\Psi(\mathbf{x})\{\underbrace{\nabla[\Psi(\mathbf{x}) + \nabla^2\Psi(\mathbf{x}) + \nabla^2\nabla^2\Psi(\mathbf{x})]}_{\text{isotropic part}} + \underbrace{(\hat{\mathbf{e}}_\mathbf{x}\partial_x^5 + \hat{\mathbf{e}}_\mathbf{y}\partial_y^5 + \hat{\mathbf{e}}_\mathbf{z}\partial_z^5)\Psi(\mathbf{x}) + O(\delta^6)}_{\text{anisotropic part}}\}. \tag{C.4}$$

This anisotropic component of the force due to the anisotropy of $E^{(6)}$ is responsible for spurious currents.

Bibliography

[1] Z. Zhuang, et al., *Extended Finite Element Method.*, Elsevier, Beijing, 2014.

[2] H. Huang, et al., *Multiphase Lattice Boltzmann Method: theory and application.*, Wiley Blackwell, United Kingdom, 2015.

[3] A. W. Date, *Introduction to Computational Fluid Dynamics.*, Cambridge University Press, Cambridge, 2005.

[4] T. M. Squires, S. R. Quake, Microfluidics: Fluid physics at the nanoliter scale, Rev. Mod. Phys. 77, 977(2005)

[5] P. Tabeling, *Introduction a la Microfluidic*, Belin, Paris, 2003

[6] F. Blanchette, T. P. Bigioni, Dynamics of drop coalescence at fluid interfaces, J. Fluid MEch. 620 333-352 (2009)

[7] F. Blanchette, T. P. Bigioni, Partial coalescence of drops at liquid interfaces, Nature Letters 1 April 2006.

[8] F. H. Zhang, E. Q. Li, S. T. Thoreddsen, Satellite Formation during Coalescence of Unequal size Drops, Phys, Rev, Letters 102, ‘104502 (2009)

[9] L. Shen, F. Denner, N. Morgan, B. van Wachem, D. Dini, Marangoni effect on small-amplitude capillary waves in viscous fluids, Phys, Rev, E 96, 053110 (2017)

[10] P. K. Farsoiya, Y. S. Mayya, R. Dasgupta, Axisymetric viscous interfacial osccilation - theory and simulations, J. Fluid Mech. 826 797-818 (2017)

[11] M. Sbragaglia, R. Benzi, L. Biferale, S. Succi, K. Sugiyama, F. Toschi, Generalized lattice Boltzmann method with multirange pseudopotential, Phys, Rev, E 75, 026702 (2007).

[12] A weighted multiple-relaxation-time lattice Boltzmann method for multiphase flows and its application to partial coalescence cacades, Journal of Computational Physics 341 (2017) 22-43

[13] S. E. M. Tilehboni, K. Sedighi, M. Farhadi, E. Fattahi, Lattice Bolzmann Simulation of Deformation and Breakup of a Droplet under Gravity Force Using Interparticle Potential Model, IJE Transactions 26 7 (2013) 781-794

[14] A. Fakhari, M. H. Rahimian, Simulation of falling droplet by the lattice Boltzamann method, Commun Nonlinear Sci Number Simulat 14 (2009) 3046-3055

[15] S. Zi-yuan, Y. Yong-hua, Y. Fan, Q. Yue-hong, H. Gou-hui, A Lattice Boltzmann Method for Simulation of a Three-dimensional drop impact on a Liquid Film, Journal of Hydrodynamics 2008,20(3) 267-272

[16] E. H. Lucassen-Reynders, J. Luccasen, Properties of Capillary Waves, Elsevier Publishing, Netherlands.

[17] S. Schmieschek, L. Shamardin, S. Frijters, T. Krüger, U. D. Schiller, J. Hartig, LB3D: A parallel implementation of the Lattice-Boltzmann method for simulation of interacting amphiphilic fluids, Com. Phys. Comm. 217 (2017) 149-161

[18] J. Desplat, I. Pagonabarraga, P. Blandon, Comput. Phys. Comm. 134 (2001) 273

[19] M. D. Mazzeo, P. V. Coveney, HemeLB: A high performance parallel lattice-Boltzmann code for large scale fluid flow in complex geometries, Comput. Phys. Comm. 178 (2008) 894-914

[20] OpenLB - Open Source Lattice Boltzmann Code (https://www.openlb.net).

[21] Palabos - CFD Complex Physiscs (http://www.palabos.org).

[22] Exa Simulation Sofware Solutions — Exa Corporation (https://exa.com).

[23] XFlow (https://www.fluidflowltd.com).

[24] Z. Chen, C. Shu, D. Tan, X. D. Niu, Q. Z. Li, Simplified multiphase lattice Boltzmann method for simulating multiphase flows with large density ratios and complex interfaces. Phys, Rev, E 98, 063314 (2018)

[25] A. Madsen, T. Seydel, M. Sprung, C. Gutt, M. Tolan, G. Gru, Capillary Waves at the Transition from Propagating to Overdamped Behavior, Physical Review Letters 92, 9 (2014)

[26] S. Succi, *The Lattice Boltzmann Equation for Fluid Dynamics and Beyond*, Oxford University Press, New Yory, 2009.

[27] L. D. Landau, E. M. Lifshiz, *Fluid Mechanics*, Pergamon Press, Second Edition, Great Britain, 1987.

[28] T. Krüger, et al., *The Lattice Boltzmann Method, principles and practice.*, Springer, Switzerland, 2017.

[29] D. A. Wolf-Gladrow, *Lattice-Gas Cellular Automata and Lattice Boltzmann Models: An introduction*, Springer, Germany, 2000.

[30] P. Bhatnagar, E. P. Gross, M. K. Krook, A model for collision processes in gases. I. Small amplitude processes in charged and neutral one-content systems. Phys. Rev., 94 (3):511-525, 1954.

[31] S. Chapman, T. G. Cowling, *The Mathematical Theory of Non-uniform Gases*, 2nd edition, Cambridge University Press, Cambridge, 1952

[32] L. Jun, Appendix: Chapman-Enskog Expansion in the Lattice Boltzmann Method, arXiv:1512.02599.

[33] Y. H. Qian and S. A. Orszag, Lattice BGK Models for the Navier-Stokes Equation: Nonlinear Deviation in Compressible Regimes, Europhys. Lett. 21(3), 255 (1993)

[34] James D. Sterling, Shiyi Chen. Stability Analysis of Lattice Boltzmann Methods. Journal of Computational Physics 123, 196-206 (1996)

[35] G. R. McNara, G. Zanetti, Use of the Boltzmann Equation to simulate Lattice-Gas Automata, Phys. Rev. Lett 61, 2332 (1988)

[36] X. D. Niu, et al., Investigation of Stability and Hydrodynamics of Different Lattice Boltzmann Models, Journal of Statistical Physics. Vol 117.

[37] Xiaoyi He and Li-Shi Luo, The Theory of lattice Boltzmann method: From the Boltzmann equation to the lattice Boltzmann equation, Physical Review E, Volume 56, Number 6, December 1997

[38] S. Chen, Z, Wang, X. Shan, and G. D. Doolen, Lattice Boltzmann Computational Fluid dynamics in three dimensions, J. Stat. Phys. 68:379 (1992)

[39] Keijo K. Mattila, Paulo C. Phillippi, Luiz A. Hegele. High-Order Regularization in Lattice Boltzmann Equations. Physics of Fluids 29, 046103 (2017)

[40] Q. Zou, X. He. On Pressure and Velocity boundary conditions for the lattice Boltzmann BGK model, Physiscs of Fluids 9, 1591 (1997)

[41] D. d'Humières, P. Lallemand, and U. Frisch, Lattice gas models for 3D hydrodynamics,Europhys. Lett. 2(4):291–297 (1986).

[42] Z. Guo, C. Zheng, B. Shi, Discrete lattice effects on the forcing term in the lattice Boltzmann method, Phys. Rev. E 65, 046308 (2002)

[43] H. Huang, M. Krafczyk, X. Lu, Forcing term in single-phase and Shan-Chen-type multiphase lattice Boltzmann models. Phys. Rev., E 84, 046710 (2011)

[44] A. A. Mohamad, *Lattice Boltzmann Method. Fundamentals and Engineering Applications with Computer Codes*, Springer, London, 2011.

[45] MA. Torres-Acosta, K. Mayolo-Deloisa, J. González-Valdez, M. Rito-Palomares, Aqueous Two-Phase Systems at Large Scale: Challenges and Opportunities, Biotechnol J. 2019 Jan.

[46] Y. Yee Koon, C. Wei Ooi, E-P. Ng, J. Chi-Wei Lan, T. Chuan Ling, P. Loke Show, Current applications of different type of aqueous two-phase systems, Bioresources and Bioprocessing Journal, 2005

[47] X. Shan, H. Chen, Lattice Boltlzmann model for simulating flows with multiple phases and components, Physical Review E 47(3) 1815-1819.

[48] X. Shan, H. Chen, Simulation of nonideal gases and liquid-gas phase transitions by the lattice Boltzmann Equation, Physical Review E 49(4), 2941-2948.

[49] F. Denner, Frequency dispersion of small-amplitude capillary waves in viscous fluids. Phys. Rev. E 94, 023110 (2016)

[50] J. Eggers, E. Villermaux, Physics of liquid jets. Rep. Prog. Phys. 71, 036601 (2008).

[51] S. Tsai, P. Luu, P. Childs, A. Teshome, C. Tsai, The role of capillary waves in two-fluid atomization, Phys. Fluids 9, 2909 (1997).

[52] M. Longuet-Higgins, The effect of non-linearities on statistical distributions in the theory of sea waves, J. Fluid Mech. 16, 138 (1963).

[53] G. Crawford, J. Earnshaw, Viscoelastic relaxation of bilayer lipid membranes. Frequency-dependent tension and membrane viscosity, Biophys. J. 52, 87 (1987)

[54] V. V. Lebedev and A. R. Muratov, Zh. Eksp. Teor. Fiz. 95, 1751 (1989) [Sov. Phys. JETP 68, 1011 (1989)].

[55] G. Gompper, D. M. Kroll, Shape of inflated vesicles, Phys. Rev. A 46, 7466 (1992).

[56] L. Yeo, J. Friend, Surface Acoustic Wave Microfluidics, Annu. Rev. Fluid Mech. 46, 379 (2014).

[57] C. Chindam, N. Nama, M. Lapsley, F. Costanzo, T. Huang, Theory and experiment on resonant frequencies of liquid-air interfaces trapped in microfluidic devices, J. Appl. Phys. 114, 194503 (2013).

[58] Tandiono, S.-W. Ohl, D. S.-W. Ow, E. Klaseboer, V. V. T. Wong, A. Camattari, C.-D. Ohl, Creation of cavitation activity in a microfluidic device through acoustically driven capillary waves, Lab Chip 10, 1848 (2010).

[59] A. Shmyrov, A. Mizev, A. Shmyrova, I. Mizeva, Capillary wave method: An alternative approach to wave excitation and to wave profile reconstruction. Phys. Fluids 31, 012101 (2019)

[60] M. Sbragaglia, R.Benzi, L. Biferale, S. Succi, K. Sugiyama, F. Toschi, Generalized lattice Boltzmann method with multirage pseudopotential, Physical Review E 75, 026702 (2007).